Modeling, Analysis and Control of Magnetically Levitated Rotating Machines

by

Ting-Jen Yeh

B.S., Power Mechanical Engineering (1988)

National Tsing-Hua University

S.M., Mechanical Engineering (1992)

Massachusetts Institute of Technology

Submitted to the Department of Mechanical Engineering

in Partial Fulfillment of the Requirements for the degree of

Doctor of Science in Mechanical Engineering

at the

Massachusetts Institute of Technology

February, 1996

Signature of Author _____

Department of Mechanical Engineering
February 1, 1996

Certified by _____

Dr. Kamal Youcef-Toumi
Associate Professor
Thesis Supervisor

Accepted by _____

Dr. Ain A. Sonin
Chairman, Department Committee on Graduate Students

Modeling, Analysis and Control of Magnetically Levitated Rotating Machines

by

Ting-Jen Yeh

Submitted to the Department of Mechanical Engineering
on Jan 4, 1996 in partial fulfillment of the
requirements for the degree of Doctor of Science in
Mechanical Engineering

ABSTRACT

Total elimination of friction and the active control nature make magnetic bearings more attractive than conventional bearings in applications such as turbomachinery and machine-tool spindles. In these applications, machines go through significant dynamic changes due to gyroscopic effects and disturbances resulting from rotor unbalances or machining forces. These dynamic characteristics, together with the fact that magnetic bearings are inherently nonlinear and unstable due to the nonlinearities of electromagnetic fields, have created challenging problems in modeling, analysis and control. To address and solve these problems, this thesis contains three main themes, namely, investigating achievable performance, obtaining a simple but accurate model and developing an adaptive controller that is robust to nonlinearities and changing system dynamics.

First, a Loop-Transfer-Recovery (LTR) based approach is presented to identify the achievable system performance. A simple finite dimensional model for a magnetically levitated machine is constructed and limitations from hardware components are examined. Using LTR's asymptotic properties and the small gain theorem, the relations among the system bandwidth, the disturbance-rejection capabilities and the flexibility effects are revealed. Second, a model refining procedure is proposed. With the help of the lumped-parameter assumptions and Thevenin's theorem, the refined model not only explains non-ideal effects such as flux leakage, fringing fluxes and the eddy current loss, but also makes a good connection between the physics and the feasible experimental data. Third, in order to directly incorporate the nonlinearities and changing dynamics as part of the control system design, a new adaptive control scheme is developed. The scheme uses local function estimation to cancel the nonlinear and uncertain dynamics present in the system and introduce some desired dynamics. With a properly designed sampling rule, the neighborhood of approximation can be moved from time to time in order to capture the changing dynamics. Stability proofs and practical implementation issues are given. The resultant controller is applicable to SISO systems as well as certain classes of MIMO systems.

The concepts and procedures introduced have been validated either numerically or experimentally on a five-axis magnetically levitated turbo pump. Particularly, the adaptive controller was digitally implemented on a high speed Digital Signal Processor. The sampling frequency employed was $15KHz$. Disturbance rejection tests were conducted for spinning and non-spinning conditions. Results indicate that, at low frequencies, the adaptive control system has much better stiffness properties over a highly complicated analog linear compensator. The controller also maintains the same disturbance rejection properties over a range of rotor speeds.

Thesis Supervisor: Dr. Kamal Youcef-Toumi

Title: Associate Professor of Mechanical Engineering

Acknowledgement

First, I would like to thank my thesis supervisor, Professor Kamal Youcef-Toumi for his advice and assistance throughout my thesis work. He has consistently lead me in the direction of work which has both practical and theoretical relevance. His ideas, suggestions and comments have helped me a great deal.

I also want to thank Professors Anuradha Annaswamy, David Trumper and George Verghese for serving on my thesis committee. They have devoted considerable time and attention to my thesis work and offered helpful suggestions and comments.

I am thankful to National Science Foundation for supporting me through research assistantships. I thank Ebara Research Co. for providing us with the active magnetic bearing system for our research work.

In addition, I want to thank Jake Wetzel, who has been helpful in familiarizing me with the hardware and in conducting experiments with me. I will always remember all the weekends we spent together in fixing the machine, carrying out the system identification tests. This thesis would not have been possible without his support.

I thank all the students I have worked with in the flexible automation laboratory. The former and the current students, Tarzen, Jose, Shih-Ying, Mitchell, Francis, C.-J., Henry, Suresh, Shang-Teh, Tetsuo, Doug, have made my graduate student life so enjoyable. Particularly without Tarzen, it would have been so lonely for me to stay alone in 35-135 at nights and during the weekends.

I would like to thank my parents. It is their continuous encouragement and support allowing me to focus my full concentration on my study at MIT.

Finally, the love of my wife, Serena, has always been of special importance to me. I am thankful to her for putting up with the unreasonable number of hours that I was forced to spend in the laboratory and this thesis is dedicated to her.

Contents

List of Figures

Chapter 1
Introduction

1.1 Motivation

The use of active magnetic bearings to levitate rotating machines has attracted considerable attention in the last forty years. One of the reasons is that magnetic bearings make no physical contact with the spinning rotors, thus eliminating the friction which usually exists in conventional bearings. The absence of friction not only contributes to longer bearing life but also to the elimination of the need for lubrication. Because lubrication often poses problems in vacuum and other hostile environments, magnetic bearings have a wider applicability in comparison with conventional bearings. For example, properly designed magnetic bearings can be operated in a wide range of temperatures ranging from $-250^{o}C$ to $450^{o}C$. Finally, magnetic bearings' active control nature provides on-line adjustment of system stiffness and damping [57], which often leads to a reduction in vibrations.

The idea of suspending a rotating body by means of magnetic forces was introduced as early as 1842 by Earnshaw. He proved that a stable three-axis magnetic suspension system can not be achieved using only passive permanent magnets. According to Earnshaw's theorem, to ensure stability, at least one axis must be actively controlled [16]. After World War II, the development of magnetic levated systems was greatly encouraged by the advances of electrical technologies. In 1957, La Recherche Aeronautique carried the first complete description for totally active magnetic suspension. Then a French patent on a fully active magnetic suspension system was

issued and assigned to Hispano-Sulza Company [20]. Subsequently, several research teams were involved in developing actively controlled magnetic suspension systems for various applications such as neutron chopper, high-speed centrifuges, vacuum pumps, and momentum wheels for spacecrafts. For instance, a radially passive gyros and flywheels with eddy current dampers was designed by the Cambridge Thermionic Corp. for the National Aeronautics and Space Administration's Doddard Space Flight Center. Due to the enormous progress achieved in electronics, the number of industrial applications of active magnetic bearings technology has considerably increased in the last 15 years. The applications include high-speed centrifuges, vacuum pumps, machine tool spindles, medical devices, rototics. contactless acturtors and vibration. These and other applications are described in [43, 15]. A brief historical review of magnetic bearings can be found in [36].

This thesis particularly focuses on modeling. analysis and control of magnetically levitated rotating machines such as turbomachinery and machine tools spindles. Regardless of their advantages, magnetic bearings are inherently nonlinear and unstable due to the nonlinearities of electromagnetic fields. Moreover, in the rotating machine applications, systems go through significant dynamic changes due to gyroscopic effects and disturbances are present because of unbalances in the rotors or the machining force. These characteristics certainly introduce complexities to the system dynamics and control. As a result, to increase the system performance, several issues associated with system dynamics and control need to be addressed

The first key issue in dynamics and control of the magnetically levitated rotating machines is identifying the overall achievable performance given the specific characteristics of individual hardware components. Acquiring knowledge about the achievable performance would provide a system engineer a better understanding of the capability of the system so that a proper controller can be designed according to the system

dynamics. At the same time, a design engineer can also apply the knowledge about the achievable performance to determine the appropriate hardware parameters. Nevertheless, the task is not easy, particularly when one deals with the magnetic bearings whose lack of absolute stability makes the integration of control system design necessary. Moreover, the fact that "components" from various energy domains interact and impose constraints on each other and have their individual behaviors combined in a nonobvious way adds more difficulty to the task.

Second, in the process of acquiring the knowledge on the achievable performance, one also needs to acquire a simple model to characterize the critical features and to account for the energy transduction among different domains in the magnetic bearing system. Such a model also has to be accurate enough so that it can be further used in extensive simulations to facilitate the control system design. However, because magnetic bearings are inherently nonlinear and unstable, assumptions which most conventional identification techniques are based on are violated in this case. Obtaining a good magnetic bearing model thus presents challenging work for system engineers.

Finally, even though a satisfactory model can be obtained, the control of multi-axis magnetic bearing systems is another issue. Not only the nonlinear nature of the actuators, but also the force coupling among various axis makes the control system design a challanging task. Furthermore, in order to achieve desired performance accross the entire operating range, the controller has to be robust against gyroscopic effects, model uncertainties resulting from changes of the rotor speed and the unpredictable disturbances due to unbalances of the rotor. Consequently, the usual fixed-gain linear controller may not be adequate and controllers which can deal with both nonlinearity and uncertainty is therefore strongly favored for magnetically levitated rotating machines.

Motivated by the issues discussed above, this thesis work is devoted to investigat-

ing the achievable performance, developing a model refining procedure to facilitate the controller design, and proposing an control scheme which deals with nonlinearity and uncertainty The research background of this three topics is first given below.

1.2 Background

Although identifying the achievable performance is crucial for the design and control of magnetically levitated machines, not much effort has been contributed. Bornstein and Rao [8, 34] looked into the connection between the maximum load capacity and bearing stiffness in the dynamic range. A similar problem was also addressed by Maslen [27] where a certain iterative scheme was used to obtain the required load capacity of the magnetic bearing by searching for the worst case sinusoidal disturbance, but the procedure is tedious and not guaranteed to produce a convergent solution. Furthermore, in [13] Dhar and Barrett attempted to calculate the individual bearing stiffness and damping coefficient to achieve the desired modal response. Basically, all these approaches lack a systematic procedure to integrate all the important issues including system dynamics, control algorithm and hardware characteristics. Morever, discussions are mainly focused on Single-Input-Single-Output systems. Multi-Input-Multi-Output cases are seldom addressed.

In the research literature, modeling of the magnetic bearing system is typically achieved using the magnetic circuit theory [41, 49]. In this case, non-ideal effects such as the eddy current loss, the flux leakage, and the fringing flux, which are difficult to quantify, are assumed to be negligible. By the use of related electromagnetic principles, the resulting magnetic force turns out to be proportional to the square of input current and inversely proportional to the air gap distance squared and the proportional constant is a function of the pole face area, number of the turns of the coil and the air permeability. Nevertheless, due to the restrictive assumptions

made, there always exist significant discrepancies between the real system and this theoretical model. In [17], Fabien proposed a nonlinear model to account for the non-ideal effects, in which the flux leakage is modeled as the reluctance in parrel with the magnetomotive force and the core reluctance is in series with air relucatace. In this model, an effective area is also used to represent the fringing flux effect. In such a model, the detailed system behavior is not carefully examined. Thus the magnetic fluxes assumed is not physically justified.

Because of the abundent research in the linear control theory, linear models of the magnetic bearings are also frequently employed. These models are based on linearization of the dynamic equations about the equilibrium point[56]. Linear control system design using these linear models has been discussed extensively. For example. Matusmara and Yoshimoto [28] used an integral type servo controller to control a horizontal rotor-magnetic bearing system. Lee and Kim [25] performed model testing and suboptimal vibration control offlexible rotor bearing system by using a magnetic bearing. Hubbard and McDonald [23] used linear-quadratic approach to design a full-state feedback controller for a pendulous supported flywheel. Additional references on linear control system design can be found in [43, 19, 1].

Linear controllers are based on linearized models. They may not be appropriate for magnetic bearings because the systems are characterized by high speed, high precision, and rapidly changing dynamics. These properties may lead to a significant increase in the nonlinear effects. Moreover, either because precise descriptions of the nonlinear effects are hardly available are the rotor speed changes rapidly, model uncertainties often exist and can not be neglected. Consequently, any practical control design for high performance magentically levitated rotating machines must address both the nonlinearities and the uncertainties issues.

Two approaches have been proposed to control systems with nonlinearities and

uncertainties. One is the adaptive approach, and the other is the robust approach. Fig.1.1 shows a general structure for these two types of control systems. For the adaptive type controllers, based on the prior information about the plant, reference inputs and disturbances, a set of proper basis funtions is assumed to span the system function space, and then an estimation scheme is used to identify the individual weighting factors (or coordinates of the basis functions) in real-time. By forming a linear combination of the basis functions, a compensating signal is generated to cancel the system function. Depending on the nonlinearities encountered and the system performance sought, basis functions can consist of, for example, gaussian radial basis functions[38], neurons[33], convolution kernels[22]. Furthermore, if the system behaves in a way that the inherent physics can be applied to obtain the basis functions, not only the control structure is drastically simplified but also higher performance is achieved. Such a concept has enjoyed a great sucess in the control of robot manipulators, spacecrafts and underwater vehicles[39].

For the robust control of nonlinear, uncertain systems, sliding control methodology has been investigated frequently[47]. This methodology constructs the compensating signal bases on the bounds on the nonlinearities and/or uncertainties rather than approximating and estimating the nonlinearities directly. The control system is characterized by a discontinuous function with high frequency chattering, which forces the system to follow the reference signal quickly. This infinite frequency chattering. however, is undesirable in practice, since it involves high control activity and may futher excite high-frequency unmodeled dynamics. The use of boundary layer was adopted in [40] to smooth out the control discontinuity and eliminate the chattering problem.

Some control methods discussed above have been reported for magnetic bearing applications. For example, design of sliding mode controllers have been applied for

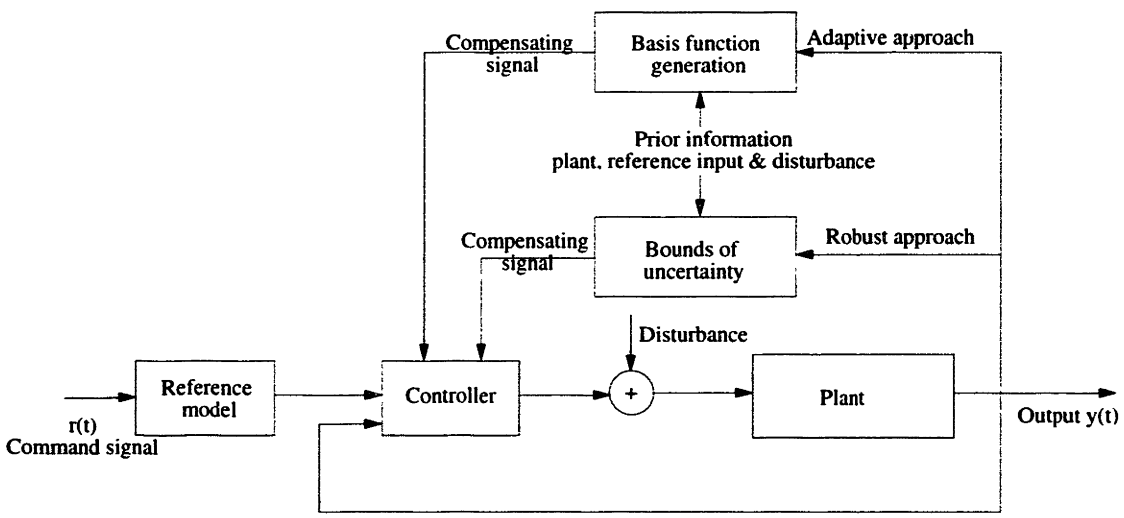

Figure 1.1: General control structure for nonlinear, uncertain systems

magnetic suspensions [31] and rotor-magnetic bearing systems [37]. However, None of the references report any experimental results. In practical applications, one often faces situations that the prior knowledge about the basis functions, the bounds of the uncertainties, and the nonlinear system characteristics are not available. On the other hand, the number of the basis functions may be too large so that on-line computation is practically impossible with today's technologies. In such cases, these controllers may fail and one needs to find some other procedures to design the controller. Motivated by this practical issues, Youcef-Toumi has proposed Time Delay Control (TDC) [53, 54, 55].

Unlike the control strategies described before, TDC does not depend on estimation of specific parameters or repetitive actions, and does not require switching action. Rather, it directly estimates uncertain yet nonlinear system functions, which is accomplished using time delay. The gathered information is used to cancel the unknown dynamics and the unexpected disturbances simultaneously. Then the controller imposes desired dynamics into the plant. Previously, TDC has been applied to servo systems, robot manipulators and magnetic bearing system and has shown impressive performance in face of unpredictable disturbances and uncertain, nonlinear system dynamics [53, 54, 56]. One main purpose of this thesis is to employ the local function estimation idea used in TDC to develop an alternative controller for a magnetically levitated rotating machine.

1.3 Scope and Contents of the Thesis

This thesis contains three main themes, namely, investigating achievable performance, obtaining a simple but accurate model and developing a robust controller using local function estimation for magnetically levitated rotating machines. An Loop-Transfer-Recovery (LTR) based procedure is first proposed to initiate the integration of design and control and solve the achievable performance problem for magnetically levitated rotating machines. Limitations from hardware components constraint the system behavior in various manners. Combining LTR's asymptotic properties and these performance constraints, it is possible to investigate the relation between the system bandwidth and the achievable performance more closely.

For the modeling part, a finite dimensional model for a magnetically levitated machine is presented. The rigid rotor dynamics as well as the actuator dynamics are described. In order to further refine the model, more detailed system behavior such as flux leakages, fringing fluxes and the eddy current loss are also considered and

Thevenin's theorem is used to obtain a simple equivalent model.

As far as the controller design is concerned, an adaptive control scheme based on the local function estimation concept is applied to cancel the nonlinear and uncertain dynamics present in magnetically levitated machines. Instead of approximating the nonlinear, uncertain system function globally as it is suggested in the adaptive control literature, the control scheme developed uses a local function estimation concept. Because the approximation and the estimation of the system function are localized, a less number of basis functions is needed. This, together with the property that the neighborhood of approximation is constantly updated, could give the control system fast adaptation capability and robust performance.

The thesis is organized as follows: First, modeling of magnetically levitated machines is given in Chapter 2. Two current control schemes and the associated performane constraints are also examined in detail. In Chapter 3, an LTR based approach is used to investigate the relation between the system bandwidth and the disturbance-rejection capabilities. Chapter 4 contains experimental results on system idenfication, as well as a modeling refining procedure to connect the physics and the experimental data. To effectively deal with the nonlinarities and uncertainities existing in magnetically levitated rotating machines, an adaptive controller is proposed in Chapter 5. Chapter 6 presents the practical implementation issues and simulations of the adaptative controller. The adaptive control of the magnetically levitated turbo pump together with the experimental evaluation is presented in Chapter 7. Finally, concluding remarks are given in Chapter 8.

Chapter 2

Analysis of Magnetically Levitated Rotating Machines

2.1 Introduction

The system of interests is a magnetically levitated turbo pump used in the semiconductor industry for creating vacuum environments. The sectional view of this machine is shown in Figure 2.1. In this machine, the rotor is spun by an induction motor. There are two circular-shaped radial bearings to keep the rotor centered and one thrust bearing to support the weight of the rotor. In addition, the positions of the rotor are measured by inductive sensors. These sensors have similar configurations as the magnetic bearings.

The purpose of this chapter is to analyze the dynamics of such magnetically levitated rotating machines. A model which consists of the the rotor dynamics and actuator dynamics is given first. Then different current control schemes and associated performance limitations are discussed. The knowledge acquired here will be used extensively in later chapters to investigate the achievable performance, to perform model refinement and to design the control system.

2.2 System Dynamics

Simplified schematic diagrams for the rotor-bearing assembly are shown in Figure 2.2. As shown in Figure 2.2.a, each of the two radial bearings actuates forces in the two radial directions (X_1 and Y_1 or X_2 and Y_2) with an eight pole electromagnet. The

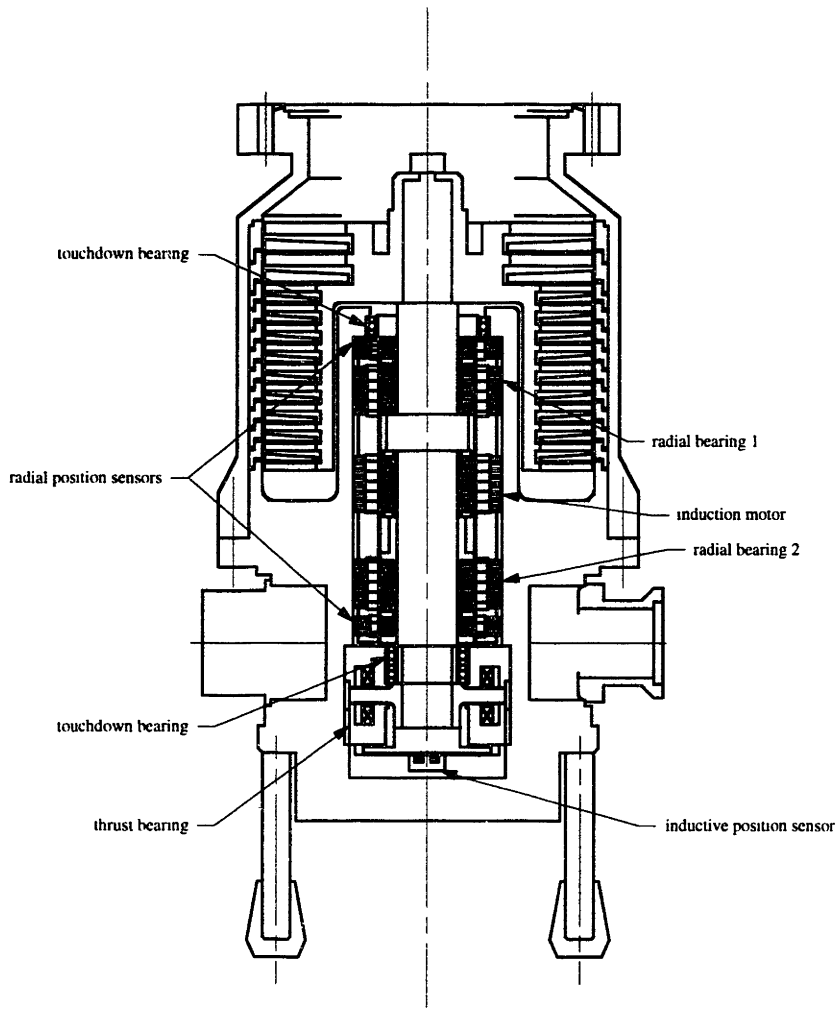

Figure 2.1: Schematics of a magnetically levitated turbo pump

radial bearings together control two rotational and two translational degrees of freedom. In Figure 2.2.b, the displacement in the axial direction is controlled by a thrust bearing with two annular electromagnets. In order to obtain the overall dynamic equations, we first examine the dynamics of the rigid rotor and the electromagnetic actuator separately.

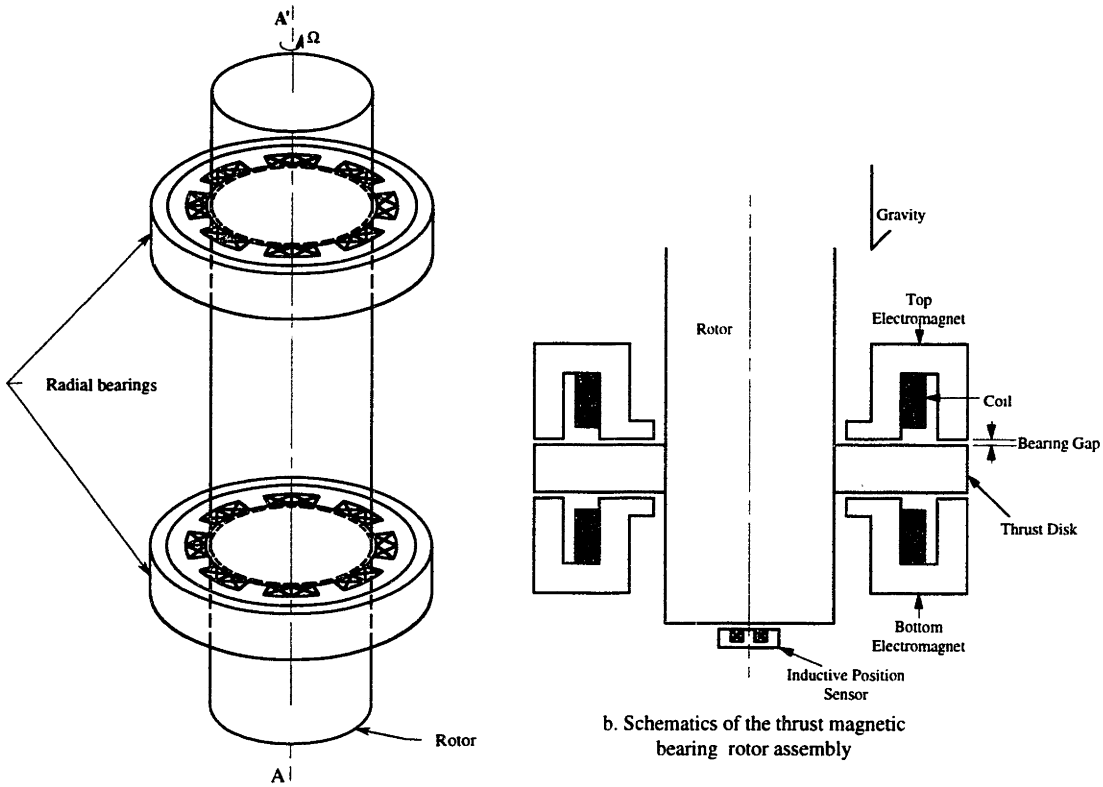

Figure 2.2: Schematics of a magnetically levitated rotating machine

2.2.1 Rigid Rotor Dynamics

A free body diagram of the rigid rotor is shown in Figure 2.3. The forces F_{x1}, F_{y1}, F_{x2}, F_{y2} are provided by the two radial bearings, which are at distances a_1 and a_2 from the rotor center of mass respectively. The thrust bearing generates a force F_z to support the weight of the rotor. A exogenous disturbance force F_d, which consists of F_{dx} and

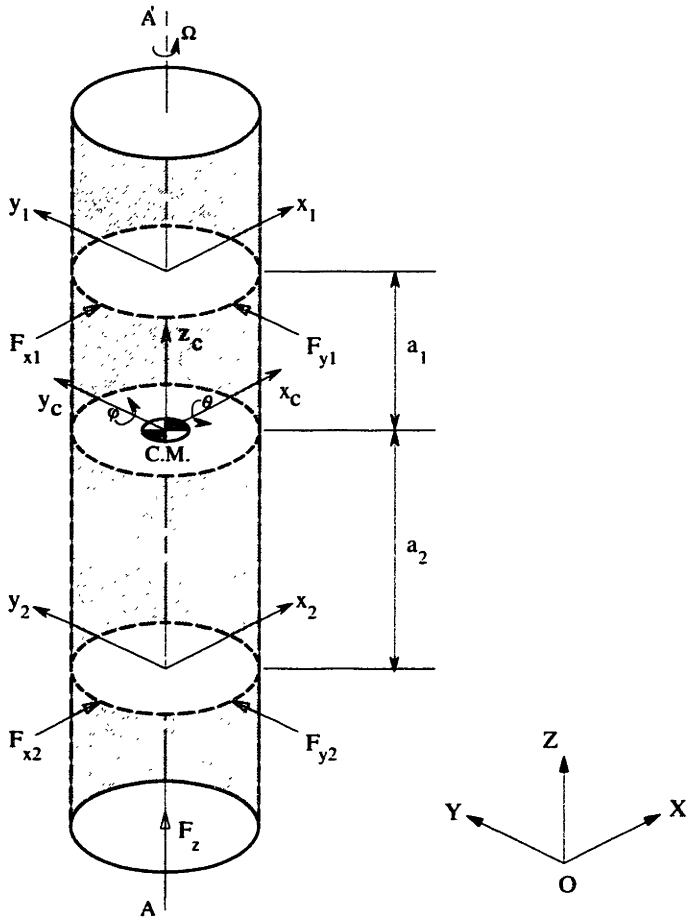

Figure 2.3: The freebody diagram of a magnetically levitated rotating machine

F_{dy}, is applied at a distance ℓ from the center of mass. $O - XYZ$ is the inertial frame fixed in the space. x_c, y_c, and z_c are the displacements of the center of mass along the X, Y and Z directions. x_1, y_1, x_2, and y_2 are displacements of the rotor near radial bearing locations. All of these displacements are given with respect to the inertial frame. It is also assumed in this analysis that the radial measurements and bearing forces are in the same radial plane of the rotor: the effects of non-collocation

are ignored. θ and φ are (yaw and pitch) angles of rotation about the X and the Y axis, respectively. These angles are assumed to be small. Furthermore, in practice, the center of mass of the rotor may not coincide with the geometric center, and the axis of rotation may not be perfectly aligned with the rotor's major principle axis. Therefore, both the static unbalance and the dynamic balance are usually present in rotating shafts. In Figure 2.4, the static unbalance ε is the distance between the rotor's geometric center O and its center of mass O_b, and the dynamic unbalance τ is the angle between the major principle axis $O_b\vec{Z}_b$ and the axis of rotation. Also in this figure, δ_1 and δ_2 are the phase angles associated with the unbalances.

The resulting dynamic equations, in terms of x_c, y_c, z_c, φ and θ, are given by [9],

$$\begin{aligned}
m\ddot{x}_c &= F_{x_1} + F_{x_2} + F_{dx} + m\varepsilon\Omega^2\cos(\Omega t + \delta_1) \\
m\ddot{y}_c &= F_{y_1} + F_{y_2} + F_{dy} + m\varepsilon\Omega^2\sin(\Omega t + \delta_1) \\
m\ddot{z}_c &= F_z - mg \\
I_r\ddot{\theta} + I_a\Omega\dot{\varphi} &= -a_1F_{y_1} + a_2F_{y_2} + \ell F_{dy} + (I_r - I_a)\tau\Omega^2\cos(\Omega t + \delta_2) \\
I_r\ddot{\varphi} - I_a\Omega\dot{\theta} &= a_1F_{x_1} - a_2F_{x_2} - \ell F_{dx} + (I_r - I_a)\tau\Omega^2\sin(\Omega t + \delta_2),
\end{aligned} \tag{2.1}$$

where m is the mass of the rotor, I_a and I_r are the axial and transverse mass moment of inertias. Notice that the gyroscopic coupling effect appears as $I_a\Omega\dot{\theta}$, $I_a\Omega\dot{\varphi}$ terms in these equations because of the rotation speed Ω. Assuming the static unbalance ε is small compared to a_1 and a_2, the following relations can be obtained from geometry.

$$\begin{aligned}
x_1 &= x_c + a_1\varphi \\
x_2 &= x_c - a_2\varphi \\
y_1 &= y_c - a_1\theta \\
y_2 &= y_c + a_2\theta \\
z &= z_c
\end{aligned} \tag{2.2}$$

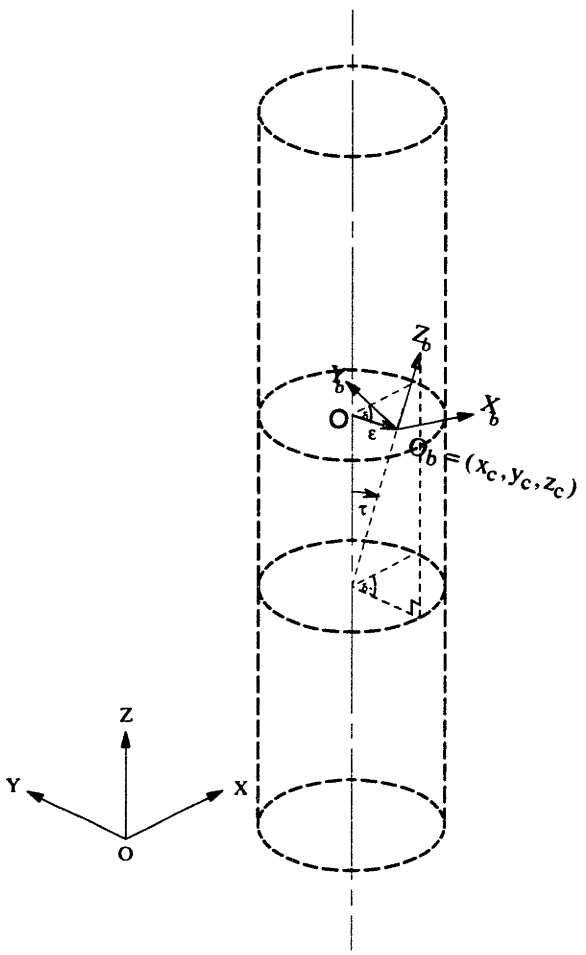

Figure 2.4: The unbalances of the rotor

The dynamic equations of (2.1) can now be written in terms of x_1, x_2, y_1, y_2, and z as:

$$\begin{aligned}
\ddot{x}_1 + \frac{a_1\Omega}{a_1+a_2}\frac{I_a}{I_r}(\dot{y}_1 - \dot{y}_2) &= \frac{\alpha}{m}F_{x1} + \frac{\beta}{m}F_{x2} + \frac{\zeta_1}{m}F_{dx} + \\
&\quad \Omega^2\left[\varepsilon\cos(\Omega t + \delta_1) + \frac{I_r - I_a}{I_r}a_1\tau\sin(\Omega t + \delta_2)\right] \\
\ddot{x}_2 - \frac{a_2\Omega}{a_1+a_2}\frac{I_a}{I_r}(\dot{y}_1 - \dot{y}_2) &= \frac{\beta}{m}F_{x1} + \frac{\gamma}{m}F_{x2} + \frac{\zeta_2}{m}F_{dx} +
\end{aligned}$$

$$
\begin{aligned}
& & & \Omega^2\left[\varepsilon\cos(\Omega t+\delta_1)-\frac{I_r-I_a}{I_r}a_2\tau\sin(\Omega t+\delta_2)\right] \\
\ddot{y}_1-\frac{a_1\Omega}{a_1+a_2}\frac{I_a}{I_r}(\dot{x}_1-\dot{x}_2) &= & \frac{\alpha}{m}F_{y1}+\frac{\beta}{m}F_{y2}+\frac{\zeta_1}{m}F_{dy}+ \\
& & \Omega^2\left[\varepsilon\sin(\Omega t+\delta_1)-\frac{I_r-I_a}{I_r}a_1\tau\cos(\Omega t+\delta_2)\right] \\
\ddot{y}_2+\frac{a_2\Omega}{a_1+a_2}\frac{I_a}{I_r}(\dot{x}_1-\dot{x}_2) &= & \frac{\beta}{m}F_{y1}+\frac{\gamma}{m}F_{y2}+\frac{\zeta_2}{m}F_{dy}+ \\
& & \Omega^2\left[\varepsilon\sin(\Omega t+\delta_1)+\frac{I_r-I_a}{I_r}a_2\tau\cos(\Omega t+\delta_2)\right] \\
\ddot{z} &= & \frac{F_z}{m}-g, \qquad (2.3)
\end{aligned}
$$

where $\alpha=\frac{I_r+ma_1^2}{I_r}$, $\beta=\frac{I_r-ma_1a_2}{I_r}$, $\gamma=\frac{I_r+ma_2^2}{I_r}$, $\zeta_1=\frac{I_r-ma_1\ell}{I_r}$, and $\zeta_2=\frac{I_r+ma_2\ell}{I_r}$..

2.2.2 Actuator Dynamics

Because the magnetic bearings under consideration generate the actuation forces using the same energy-transduction principles, it suffices to study the radial bearings to understand the acturator dynamics. As shown in Figure 2.2, each eight pole radial bearing induces coupled magnetic forces along the X and Y axes. Coil currents along the X-axis induce forces along the Y-axis and vice versa. The modeling of the coupling among axes due to actuator dynamics is discussed in detail in [52]. If this effect is ignored, the magnetic force produced by the electromagnet along each radial axis can be modeled independently of the displacement and current along the other axes. Figure 2.5 shows the schematic diagram and the bond graph model of the x_1 bearing. In the model, the two electromagnets are assumed to be the same. Other modeling assumptions include: 1) the flux leakage and fringing fluxes of the magnetic field are neglected, 2) the core material is highly permeable and is laminated so that the eddy current loss is small.

In the bond graph model, the current driver of each electromagnet is modeled by an ideal flow source SF. The gyrators, with moduli n equal to the number

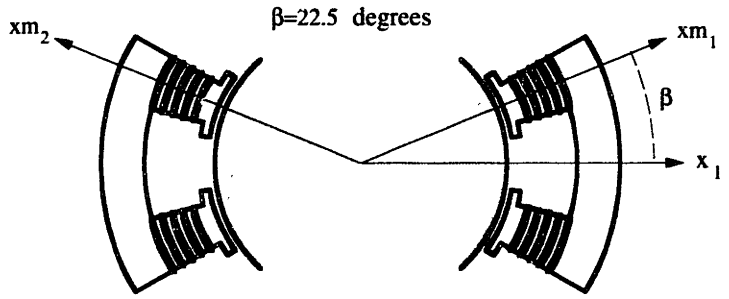

a. The schematic of the x1 magnetic bearing set

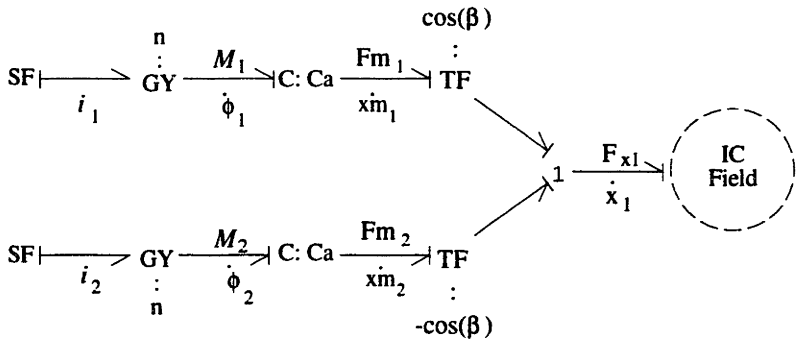

b. The bond graph model of the x1 magnetic bearing set

Figure 2.5: The schematic of the x_1 magnetic bearing and its bond graph model

of turns in each electromagnet, transduce the energy from the electrical domain to the magnetic domain. The magnetic energies are then delivered to the mechanical domain through C fields, which model the energy-storage behavior of bearing gaps. Because the magnetic forces F_{1m} and F_{2m} are not aligned with the x_1 direction, two tranformers, with moduli equal to κ and $-\kappa$ ($\kappa = \cos(22.5^o)$), are used to transmit the powers. Notice that the minus sign in the transformer modulus is to reflect that the net actuator force is an algebraic sum to the two magnetic forces acting in opposite

directions. Consequently, the magnetic forces are summed by the one junction and the net force is applied to the I-C field, which represents the rotor dynamics in (2.3).

The magnetomotive force $M_{(.)}$ (or MMF) and the magnetic flux rate $\dot{\phi}_{(.)}$ in the magnetic domain represent respectively the effort variable and the flow variable of the associated electromagnet. Furthermore, the magnetic energy $\mathcal{E}_{(.)}$ stored in the air gap is $\frac{\phi_{(.)}^2}{2C_{a(.)}}$. $C_{a(.)}$ denotes the generalized capacitance for each of the bearing gap and is equal to $\frac{\mu_0 A}{2(h_0 - x_{m(.)})}$. Here h_0 is the nominal bearing gap, $x_{m(.)} = x_{m1}$ or x_{m2} is the displacement of the rotor with respect to the pole faces of each electromagnet, μ_0 is the air permeability, A is the pole face area, and the existence of two air gaps in the electromagnet results in the factor 2 in the denominator. Based on the magnetic energy obtained, the constitutive relation for the C field in the bond graph can be derived as [24]:

$$F_{m(.)} = -\frac{\partial \mathcal{E}_{(.)}}{\partial x_{m(\ )}} = \frac{\phi_{(.)}^2}{\mu_0 A} \tag{2.4}$$

$$M_{(.)} = \frac{\partial \mathcal{E}_{(.)}}{\partial \phi_{(.)}} = \frac{2(h_0 - x_{m(.)})\phi_{(.)}}{\mu_0 A}, \tag{2.5}$$

where $F_{m(.)}$ is the attractive force generated and $\phi_{(.)}$ is the magnetic flux in each electromagnet. Consequently, the total force created by the x_1 magnetic bearing is given by:

$$F_{x1} = \kappa \left(\frac{\phi_1^2}{\mu_0 A} - \frac{\phi_2^2}{\mu_0 A} \right). \tag{2.6}$$

Moreover, because $M_{(.)}$ equals to $ni_{(.)}$ due to the gyration action, using (2.5), one can express $\phi_{(.)}$ as:

$$\phi_{(.)} = \frac{n\mu_0 A i_{(.)}}{2(h_0 - x_{m(.)})}. \tag{2.7}$$

Thus far, the analysis has been based on the fact that the magnetic core is not saturated. Because of saturation, the magnetic flux can never exceed $B_{sat}A$, where

B_{sat} is the saturation flux density of the core. Therefore, Eq.(2.7) will be assumed when

$$|\frac{n\mu_0 A i_{(.)}}{2(x_0 - x_{m(.)})}| \leq \mathcal{B}_{sat} A \tag{2.8}$$

and $\phi_{(.)} = \mathcal{B}_{sat} A$ otherwise. If both electromagnets are not saturated, one can rewrite the magnetic force equation as:

$$F_{x1} = \left(\frac{n^2 \mu_0 A i_1^2 \kappa}{4(h_0 - x_1\kappa)^2} - \frac{n^2 \mu_0 A i_2^2 \kappa}{4(h_0 + x_1\kappa)^2} \right). \tag{2.9}$$

This indicates that the actuator force is highly nonlinear in the displacement and coil currents. Notice that in obtaining the above equation. x_{m1} and x_{m2} were substituted by $x_1\kappa$ and $-x_1\kappa$ respectively using the corresponding transformer moduli.

Since the radial bearings are the same, magnetic force equations similar to (2.9) can be derived for the y_1, x_2, and y_2 bearings as well. Moreover, same expressions also apply to the thrust bearing to account for the magnetic force along the Z axis, although the parameter κ equals 1 instead. In this case, the magnetic force for the thrust bearing has the following expression:

$$F_z = \left(\frac{n^2 \mu_0 A i_{zu}^2}{4(h_0 - z)^2} - \frac{n^2 \mu_0 A i_{z\ell}^2}{4(h_0 + z)^2} \right), \tag{2.10}$$

where i_{zu} and $i_{z\ell}$ are the coil currents of the upper and lower annular electromagnets respectively. Notice that because the magnetic force is now aligned with the relative movement between the rotor and the bearing pole faces, transformers are not needed and the parameter κ equals 1.

2.2.3 Overall System Dynamics

Since the radial bearings are the same, magnetic force equations similar to Eq.(2.9) can be derived for the y_1, x_2, and y_2 bearings as well. These equations, together with

the rotor dynamics in Eq.(2.3), compose the overall system dynamics. Obviously, by regulating the coil currents properly, the magnetic bearings can provide forces to control the rotor and achieve good disturbance rejection. Therefore, the success of using magnetic bearings lies in how the control system is designed. Assuming the coil current of each electromagnet is accessible and the relative displacements x_1, y_1, x_2, y_2 and z are measurable, the overall system contains ten inputs and five outputs[1]. Because the major nonlinearites in the resulting dynamic equations arise from the actuator dynamics, linearization schemes are usually performed first to reduce the nonlinearities in the actuator dynamics and facilitate the control system design. In the following section, two linearization schemes and the associated performance constraints are investigated.

2.3 Current Control Schemes and Performance Constraints

Typically, two linearization schemes are employed for magnetic bearings. One is the input-state linearization, the other is the bias current linearization. Before discussing these schemes and the associated performance constraints in detail, we begin with introducing the following dimensionless variables: Among the variables, i_0 is a reference current which will be selected as the bias current later, $\omega_n = \sqrt{\frac{B_{sat}^2 A}{m h_0 \mu_0}}$ is a reference frequency, and P_{max}, v_s are respectively the maximum power output and the DC supply voltage of the current drivers[2]. With the help of these dimensionless variables, the dependence of the system characteristics on the physical parameters can be easily revealed. Particularly, the selection of ω_n, P_{max}^* and v_s^* allows one to

[1]The dynamics of the spinning motion is not considered here: hence, the rotation speed Ω is not a state variable and is assumed to be measurable.

[2]Parameters such as i_0, A, h_0 , P_{max} and v_s for the thrust bearing may be different from those of the radial bearings.

$F^*_{(.)} = \frac{F_{(.)}\mu_0}{B^2_{sat}A}$	Normalized Force
$i^*_{(.)} = \frac{i_{(.)}}{i_0}$	Normalized Current
$x^*_{(.)}, y^*_{(.)}, z^* = \frac{x_{(.)}, y_{(.)}, z}{h_0}$	Normalized Displacement
$B^* = \frac{n\mu_0 i_0}{2h_0 B_{sat}}$	Normalized Flux Density
$t^* = t\omega_n$	Normalized Time
$\varepsilon^* = \frac{\varepsilon}{x_0}$	Normalized Static Unbalance
$\tau^* = \frac{a_1 \tau}{x_0}$	Normalized Dynamic Unbalance
$P^*_{max} = \frac{2\kappa P_{max}\mu_0}{B^2_{sat}A\omega_n x_0(2-\kappa)}$	Normalized Power
$v^*_s = \frac{2v_{s0}\mu_0}{B^2_{sat}A\omega_n x_0}$	Normalized DC Supply Voltage
$\Omega^* = \Omega\omega_n$	Normalized Rotation Speed
$g^* = \frac{g}{\omega_n^2}$	Normalized Gravity

Table 2.1: Dimensionless variables

concisely present the subsequent analysis on performance constraints.

2.3.1 Input-State Linearization Scheme

As the title suggests, this linearization scheme is achieved by a combination of a state transformation and an input transformation, so that the nonlinear system dynamics can be transformed into a linear one [45, 46]. Taking the x_1 bearing as an example, the transformations are:

$$\begin{aligned}
\text{if } F_{x1} &\geq 0 \\
i_1 &= \sqrt{\frac{4F_{x1}(h_0 - x_1\kappa)^2}{n^2\mu_0 A\kappa}} \\
i_2 &= 0 \\
\text{if } F_{x1} &< 0 \\
i_1 &= 0 \\
i_2 &= \sqrt{\frac{-4F_{x1}(h_0 - x_1\kappa)^2}{n^2\mu_0 A\kappa}}.
\end{aligned} \tag{2.11}$$

One can now directly use the linear system in Eq.(2.1) for controller design by treating $F_{(.)}$'s as the control inputs. However, in practice, the hardware components are far

from ideal and they will impose performance constraints on the system.

First, emergency touchdown bearings are usually placed to prevent the rotor from colliding into the magnetic bearing pole faces. In the ensuing discussion, it is assumed that the touchdown bearings would limit the displacements of the rotor so that

$$|x_1, x_2, y_1, y_2, z| \leq \frac{h_0}{2}. \tag{2.12}$$

Second, due to the saturation of the magnetic flux, the magnitude of magnetic forces can never exceed $\kappa \frac{B_{sat}^2 A}{\mu_0}$. Such a constraint is referred as the fixed load capacity in the literature. Finally, the rate of change of magnetic forces is limited. The resulting effect is known as the fixed force slew rate limit. To view this, one can use the constitutive relation of the C field. For the x_1 bearing, the derivative of $F_{m(.)}$ with respect to time t can be written as:

$$\frac{dF_{m(.)}}{dt} = \frac{2\phi\dot{\phi}}{\mu_0 A} = \frac{M\dot{\phi}}{h_0 - x_{m(.)}}, \tag{2.13}$$

where the first equality follows from Eq.(2.4) and the second equality makes use of Eq.(2.5). Because power is assumed to be conserved in gyrators, the output power $M\dot{\phi}$ equals the input power $v_{(.)}i_{(.)}$, which is always less than the maximum power of the driver. Then the limit of the force slew rate can be given by:

$$|\frac{dF_{x1}}{dt}| = \kappa|\frac{dF_{m(.)}}{dt}| \leq \frac{2\kappa P_{max}}{h_0(2-\kappa)}. \tag{2.14}$$

The above inequality uses facts that only one electromagnet is turned on and $|h_0 - x_{m(.)}| \geq h_0(1 - \frac{\kappa}{2})$ due to the existence of the touchdown bearings.

Now, one can express the overall system dynamics and the performance constraints in terms of the dimensionless variables. They are given by:

$$\begin{aligned} \ddot{x}_1^* + \eta\Omega^*(\dot{y}_1^* - \dot{y}_2^*) &= \alpha F_{x1}^* + \beta F_{x2}^* + \zeta_1 F_{dx}^* + \\ &\quad \Omega^{*2}\left[\varepsilon^* \cos(\Omega^* t^* + \delta_1) + \xi\tau^* \sin(\Omega^* t^* + \delta_2)\right] \end{aligned}$$

$$
\begin{aligned}
\ddot{x}_2^* - \eta\nu\Omega^*(\dot{y}_1^* - \dot{y}_2^*) &= \beta F_{x1}^* + \gamma F_{x2}^* + \zeta_2 F_{dx}^* + \\
&\quad \Omega^{*2}\left[\varepsilon^* \cos(\Omega^* t^* + \delta_1) - \xi\nu\tau^* \sin(\Omega^* t^* + \delta_2)\right] \\
\ddot{y}_1^* - \eta\Omega^*(\dot{x}_1^* - \dot{x}_2^*) &= \alpha F_{y1}^* + \beta F_{y2}^* + \zeta_1 F_{dy}^* + \\
&\quad \Omega^{*2}\left[\varepsilon^* \sin(\Omega^* t^* + \delta_1) - \xi\tau^* \cos(\Omega^* t^* + \delta_2)\right] \\
\ddot{y}_2^* + \eta\nu\Omega^*(\dot{x}_1^* - \dot{x}_2^*) &= \beta F_{x1}^* + \gamma F_{x2}^* + \zeta_2 F_{dy}^* + \\
&\quad \Omega^{*2}\left[\varepsilon^* \sin(\Omega^* t^* + \delta_1) + \xi\nu\tau^* \cos(\Omega^* t^* + \delta_2)\right] \\
\ddot{z}^* &= F_z^* - g^*, \qquad (2.15)
\end{aligned}
$$

and

$$
\begin{aligned}
\left|x_1^*\right|, \left|x_2^*\right|, \left|y_1^*\right|, \left|y_2^*\right|, |z| &\leq \tfrac{1}{2} \qquad (2.16) \\
\left|F_{x1}^*\right|, \left|F_{x2}^*\right|, \left|F_{y1}^*\right|, \left|F_{y2}^*\right| &\leq \kappa \\
\left|F_z^*\right| &\leq 1 \qquad (2.17) \\
\left|\frac{dF_{x1}^*}{dt^*}\right|, \left|\frac{dF_{x2}^*}{dt^*}\right|, \left|\frac{dF_{y1}^*}{dt^*}\right|, \left|\frac{dF_{y2}^*}{dt^*}\right|, \left|\frac{dF_z^*}{dt^*}\right| &\leq P_{max}^*, \qquad (2.18)
\end{aligned}
$$

where $\eta = \frac{a_1}{a_1+a_2}\frac{I_a}{I_r}$, and $\xi = \frac{I_r - I_a}{I_r}$.

2.3.2 Bias Current Linearization Scheme

Instead of directly dealing with the actuator nonlinearites, this scheme is based on the conventional Jacobian linearization for small range operation. Still illustrating the idea using the x_1 bearing, we apply the following transformation to the coil currents:

$$
i_1 = i_0 + i_{x1}, \quad i_2 = i_0 - i_{x1}, \qquad (2.19)
$$

where i_0 is the bias current and i_{x1} is the control current. Subsituting the above relations into Eq.(2.9) and performing linearization at $x_1 = 0$ and $i_{x1} = 0$, the magnetic force now becomes

$$
F_{x1} = \frac{n^2\mu_0 A\kappa i_0^2}{x_0^2}\left(\frac{i_{x1}}{i_0} + \kappa\frac{x_1}{x_0}\right) + F_{x1,h.o.t.}. \qquad (2.20)
$$

Rewritting the above equation using the dimensionless variables, we have

$$F_{x1}^* = 4\kappa B^{*2} i_{x1}^* + 4\kappa^2 B^{*2} x_1^* + F_{x1,h.o.t.}^*. \tag{2.21}$$

Regarding the performance constraints issues. Eq.(2.12) is still applicable for the purpose of limiting the rotor displacements. Furthermore, Eq.(2.21) is valid only when both electromagnets are not saturated. namely. the conditions in Eq.(2.8) are true. Again, expressing Eq.(2.8) in terms of dimensionless variables. we have

$$\left|\frac{1 \pm i_{x1}^*}{1 \mp \kappa x_1^*}\right| \leq \frac{1}{B^*}. \tag{2.22}$$

However, in order to simplify the analysis afterwards. rather than using the above equation, we impose a more restrictive constraint:

$$\frac{1 + |i_{x1}^*|}{1 - \kappa |x_1^*|} \leq \frac{1}{B^*}. \text{ or } B^*|i_{x1}^*| + \kappa |x_1^*| \leq 1 - B^*, \tag{2.23}$$

by the use of the inequality $\left|\frac{1 \pm i_{x1}^*}{1 \mp \kappa x_1^*}\right| \leq \frac{1+|i_{x1}^*|}{1-\kappa|x_1^*|}$. Eq.(2.23) can somehow guarantee that the range of operation is small, so the high order terms in the magnetic forces are negligible. For other constraints, first notice that typically in systems driven by current sources, voltage drops across the terminals of current drivers can never exceed the DC supply voltage [10, 27]. In addition, $\frac{d}{dt}(n\phi)$, which is known as the flux linkage rate. equals this voltage drop. Consequently. the flux rate $\dot{\phi}$ is limited by

$$|\dot{\phi}| \leq \frac{v_s}{n}. \tag{2.24}$$

Substitution of ϕ by the expression in Eq. (2.7) and the current transformations in Eq. (2.19) yields

$$\left|\frac{n\mu_0 A}{2(x_0 \mp \kappa x_1)}\left(\frac{di_{x1}}{dt} + \frac{\kappa(i_0 \pm i_{x1})}{x_0 \mp \kappa x_1}\frac{dx_1}{dt}\right)\right| \leq \frac{v_s}{n}. \tag{2.25}$$

Assuming a the small range of operation and using the dimensionless variables. the above inequality can be written as:

$$|4B^{*2} i_{x1}^* + 4B^{*2}\kappa x_1^*| \leq v_s^*. \tag{2.26}$$

Such a constraint is similar to the force slew rate limit discussed previously because of the first order force terms in Eq. (2.21).

All of the constraints obtained thus far strongly depend on the normalized flux density B^*. It has been reported in the literature [27, 50] that, when the displacement is small, choice of $B^* = 0.5$, or having the nonminal flux density equal to half of the saturation flux density, can maximize the range of the linear force. Therefore, $B^* = 0.5$ will be assumed through the subsequent investigations. Ignoring the high order terms in the magnetic forces, the dimensionless linear dynamic equations and performance constraints are given by:

$$\begin{aligned}
\ddot{x}_1^* + \eta\Omega^*(\dot{y}_1^* - \dot{y}_2^*) - \kappa^2(\alpha x_1^* + \beta x_2^*) &= \kappa(\alpha i_{x1}^* + \beta i_{x2}^*) + \zeta_1 F_{dx}^* \\
&+ \Omega^{*2}\left[\varepsilon^* \cos(\Omega^* t^* + \delta_1) + \xi\tau^* \sin(\Omega^* t^* + \delta_2)\right] \\
\ddot{x}_2^* - \eta\nu\Omega^*(\dot{y}_1^* - \dot{y}_2^*) - \kappa^2(\beta x_1^* + \gamma x_2^*) &= \kappa(\beta i_{x1}^* + \gamma i_{x2}^*) + \zeta_2 F_{dx}^* \\
&+ \Omega^{*2}\left[\varepsilon^* \cos(\Omega^* t^* + \delta_1) + \xi\nu\tau^* \sin(\Omega^* t^* + \delta_2)\right] \\
\ddot{y}_1^* - \eta\Omega^*(\dot{x}_1^* - \dot{x}_2^*) - \kappa^2(\alpha y_1^* + \beta y_2^*) &= \kappa(\alpha i_{y1}^* + \beta i_{y2}) + \zeta_1 F_{dy}^* \\
&+ \Omega^{*2}\left[\varepsilon^* \sin(\Omega^* t^* + \delta_1) + \xi\tau^* \cos(\Omega^* t^* + \delta_2)\right] \\
\ddot{y}_2^* + \eta\nu\Omega^*(\dot{x}_1^* - \dot{x}_2^*) - \kappa^2(\beta y_1^* + \gamma y_2^*) &= \kappa(\beta i_{y1}^* + \gamma i_{y2}^*) + \zeta_2 F_{dy}^* \\
&+ \Omega^{*2}\left[\varepsilon^* \sin(\Omega^* t^* + \delta_1) + \xi\nu\tau^* \cos(\Omega^* t^* + \delta_2)\right] \\
\ddot{z}^* &= i_z^* - g^*. \qquad (2.27)
\end{aligned}$$

and

$$|x_1^*|, |x_2^*|, |y_1^*|, |y_2^*|, |z| \le \tfrac{1}{2} \qquad (2.28)$$

$$\begin{aligned}
|i_{x1}^*| + 2\kappa|x_1^*|, |i_{x2}^*| + 2\kappa|x_2^*|. |i_{y1}^*| + 2\kappa|y_1^*|, |i_{y2}^*| + 2\kappa|y_2^*| &\le 1 \\
|i_z^*| + 2|z^*| &\le 1 \qquad (2.29) \\
\left|\frac{di_{x1}^*}{dt^*} + \kappa\frac{dx_1^*}{dt^*}\right|, \left|\frac{di_{x2}^*}{dt^*} + \kappa\frac{dx_2^*}{dt^*}\right|, \left|\frac{di_{y1}^*}{dt^*} + \kappa\frac{dy_1^*}{dt^*}\right|, \left|\frac{di_{y2}^*}{dt^*} + \kappa\frac{dy_2^*}{dt^*}\right| &\le v_s^*
\end{aligned}$$

$$\left|\frac{di_z^*}{dt^*} + \frac{dz^*}{dt^*}\right| \leq v_s^*. \qquad (2.30)$$

From now on, all *'s will be ommitted for the purpose of simplicity, but one still has to keep in mind that only the dimensionless variables are to be dealt with.

2.4 Summary and Remarks

This chapter has presented a finite dimensional model for magnetically levitated rotating machines. The plant dynamics including the actuator dyanmics, rigid rotor dynamics were described. The complexity and nonlinearities in the system characteristics were illustrated through this dynamic analysis. In order to simplify the controller design, two different current control schemes were introduced. The major difference between these two current control schemes lies in the induced system dynamics. Taking the radial bearing system consisting of x_1, y_1, x_2 and y_2 axes for example, if the rotor is not spinning, according to Eq.(2.15)the open-loop system for the input-state linearization scheme has all of its poles located at the origin, while the poles introduced by Eq.(2.27, the open loop dynamics of the bias current schemes, are the roots of the following characteristic equation:

$$\left[s^4 - 4\kappa^2(\alpha+\gamma)s^2 + 16\kappa^4(\alpha\gamma - \beta^2)\right]^2 = 0. \qquad (2.31)$$

Chapter 3
Achievable System Performance

3.1 Introduction

Because the induced open-loop dynamics of either current control scheme is not strictly stable[1], a stabilizing controller is absolutely required. This chapter introduces an LTR (Loop Transfer Recovery) based procedure to initiate the integration of design and control and solve the achievable performance problem for magnetically levitated rotating machines. Combining LTR's asymptotic properties and the performance constraints from hardware components, it is possible to investigate the relation between the system bandwidth and the achievable performance more closely.

In rotating machine applications, one of the crucial factors that determines the system performance is the disturbance rejection capability. Consequently, the discussion is particularly focused on the disturbance-rejection related issues, namely, system stiffness (or equivalently, compliance) properties and allowable unbalances, for the radial bearing system. Such an investigation will be demonstrated using the existing magnetically levitated turbo pump. Comparisons between the two current control schemes on the achievable performance will also be given. First of all, a brief review of the LTR methodology is provided below.

[1]It is not difficult to show that Eq. (2.31) has four roots in the right half plane.

3.2 LTR Controllers

LTR is a linear quadratic Gaussian (or LQG) optimal control based methodology. With the stability guaranteed, it offers engineers a relatively simple technique to perform frequency shaping in multivariable systems. There are two major ways to design LTR controllers, recovering the loop transer function at the control input or at the plant output. In this paper, the latter approach will be adopted.

Consider a linear, time invariant, minimum-phase system described by:

$$\begin{aligned} \dot{\mathbf{x}} &= \mathbf{A}\mathbf{x} + \mathbf{B}\mathbf{u} \\ \mathbf{y} &= \mathbf{C}\mathbf{x}. \end{aligned} \tag{3.1}$$

where $\mathbf{x}$ is the state vector, $\mathbf{u}$ is the control input, and $\mathbf{y}$ is the output. If one applies LQG control, which is a combination of LQ and Kalman filter designs, to the system, the resulting loop transfer function has the following asymptotical behavior [26, 42]:

$$\lim_{\rho \to 0} \mathbf{\Phi}(s)\mathbf{K}_{LQG}(s) = \mathbf{G}_{KF} = \mathbf{C}(s\mathbf{I} - \mathbf{A})^{-1}\mathbf{H}, \tag{3.2}$$

where $\mathbf{\Phi}(s) = \mathbf{C}(s\mathbf{I} - \mathbf{A})^{-1}\mathbf{B}$ is the open-loop tranfer function, $\mathbf{K}_{LQG}(s)$ is the LQG controller, $\mathbf{G}_{KF}$ is the loop transfer fucntion of the Kalman filter, $\mathbf{H}$ is the Kalman filter gain matrix corresponding to a fictitious output noise intensity μ, and ρ is the control weighting parameter of LQ. As implied in Eq. (3.2), by implementing the cheap control LQ problem in LQG, one can have the system loop tranfer function approximate the Kalman filter loop transfer function. Consequently, if $\mathbf{G}_{KF}$ is selected properly, the frequency shaping of the loop transfer funtion can also be performed accordingly.

Usually, the selection of $\mathbf{G}_{KF}$ makes use of the Kalman filter equality,

$$\sigma_i[\mathbf{I} + \mathbf{G}_{KF}(j\omega)] = \sqrt{1 + \frac{1}{\mu}\sigma_i^2\left[\mathbf{C}(j\omega\mathbf{I} - \mathbf{A})^{-1}\mathbf{L}\right]}, \tag{3.3}$$

where $\mathbf{L}$ is the process noise influencing matrix in the Kalman filter problem and the notation $\sigma_i[.]$ represents the singular value of the quantity between brackets. This equality is particularly useful when an integrator is added to each control input channel. In such LTR with integral control problems, it is shown in the Appendix A that $\mathbf{L}$ can be suitably selected so that $\mathbf{C}(j\omega\mathbf{I}-\mathbf{A})^{-1}\mathbf{L}$ approximately equals $\frac{1}{j\omega}\mathbf{I}$ at the high frequencies. Substituting this result into Eq. (3.3), the following estimation for $\mathbf{G}_{KF}(j\omega)$ in high frequencies can be easily obtained:

$$\sigma_i\left[\mathbf{G}_{KF}(j\omega)\right] \approx \frac{1}{\omega\sqrt{\mu}}. \tag{3.4}$$

Due to the loop recovery action of Eq. (3.2), one can immediately conclude that

$$\Phi(j\omega)\mathbf{K}_{LQG}(j\omega) \approx \frac{1}{\omega\sqrt{\mu}}. \tag{3.5}$$

Because the cross-over frequency now becomes $\frac{1}{\mu}$, adjusting the system bandwidth ω_b can be easily accomplished by the formula:

$$\mu = \frac{1}{\omega_b^2}. \tag{3.6}$$

3.3 Performance of Rotating Machines

In order to apply the LTR method to the radial bearing substem of the magnetically levitated rotating machine, the dynamic equations have to be expressed in the following state-space form:

$$\begin{aligned} \dot{\mathbf{x}}_p &= \mathbf{A}_p\mathbf{x}_p + \mathbf{B}_p\mathbf{u}_p + \mathbf{L}_d\mathbf{d}_f + \mathbf{L}_u\mathbf{d}_u \\ \mathbf{y} &= \mathbf{C}_p\mathbf{x}_p. \end{aligned} \tag{3.7}$$

where $\mathbf{x}_p = [x_1, x_2, y_1, y_2, \dot{x}_1, \dot{x}_2, \dot{y}_1, \dot{y}_2]^T$ is the state vector, $\mathbf{y} = [x_1, x_2, y_1, y_2]^T$ is the output vector, $\mathbf{u}_p$ is the control input which equals $[F_{x1}, F_{x2}, F_{y1}, F_{y2}]^T$ for the

input-state linearization scheme and equals $[i_{x1}, i_{x2}, i_{y1}, i_{y2}]^T$ for the bias current scheme, $\mathbf{d}_f = [F_{dx}, F_{dy}]^T$ is the external disturbance vector, and $\mathbf{d}_u = \Omega^2[\epsilon\cos(\Omega t + \delta_1), \tau\sin(\Omega t + \delta_2), \epsilon\sin(\Omega t + \delta_1), \tau\cos(\Omega t + \delta_2)]^T$ denotes the unbalance vector. According to Eq.(2.15) and Eq.(2.27), the matrices in Eq. (3.7) have the following forms:

$$\mathbf{A}_p = \begin{bmatrix} \mathbf{0}_{4\times4} & & \mathbf{I}_{4\times4} & \\ & 0 & 0 & -\eta\Omega & \eta\Omega \\ & 0 & 0 & \eta\nu\Omega & -\eta\nu\Omega \\ & \eta\Omega & -\eta\Omega & 0 & 0 \\ & -\eta\nu\Omega & \eta\nu\Omega & 0 & 0 \end{bmatrix}$$

for the input-state linearization scheme.

$$\mathbf{A}_p = \begin{bmatrix} \mathbf{0}_{4\times4} & & & & \mathbf{I}_{4\times4} & & & \\ \kappa^2\alpha & \kappa^2\beta & 0 & 0 & 0 & 0 & -\eta\Omega & \eta\Omega \\ \kappa^2\beta & \kappa^2\gamma & 0 & 0 & 0 & 0 & \eta\nu\Omega & -\eta\nu\Omega \\ 0 & 0 & \kappa^2\alpha & \kappa^2\beta & \eta\Omega & -\eta\Omega & 0 & 0 \\ 0 & 0 & \kappa^2\beta & \kappa^2\gamma & -\eta\nu\Omega & \eta\nu\Omega & 0 & 0 \end{bmatrix}$$

for the bias current linearization scheme, and $\mathbf{B}_p = \begin{bmatrix} \mathbf{0}_{4\times4} \\ \alpha & \beta & 0 & 0 \\ \beta & \gamma & 0 & 0 \\ 0 & 0 & \alpha & \beta \\ 0 & 0 & \beta & \gamma \end{bmatrix}$, $\mathbf{L}_d = \begin{bmatrix} \mathbf{0}_{4\times2} \\ \zeta_1 & 0 \\ \zeta_2 & 0 \\ 0 & \zeta_1 \\ 0 & \zeta_2 \end{bmatrix}$.

$\mathbf{L}_u = \begin{bmatrix} \mathbf{0}_{4\times4} \\ 1 & \xi & 0 & 0 \\ 1 & \nu\xi & 0 & 0 \\ 0 & 0 & 1 & \xi \\ 0 & 0 & 1 & \nu\xi \end{bmatrix}$, $\mathbf{C}_p = \begin{bmatrix} \mathbf{I}_{4\times4} & \mathbf{0}_{4\times4} \end{bmatrix}$ for both current control schemes.

Figure 3.1 shows the block diagram of the closed-loop system under the LTR integral control. In this diagram, according to [6, 4],

$$\mathbf{K}_{LQG}(s) = \mathbf{G}\,[s\mathbf{I} - \mathbf{A} + \mathbf{B}\mathbf{K} + \mathbf{H}\mathbf{C}]^{-1}\,\mathbf{H}, \tag{3.8}$$

in which $\mathbf{G} = \frac{1}{\rho}\mathbf{B}'\mathbf{P}$ and $\mathbf{H} = \frac{1}{\mu}\mathbf{Q}\mathbf{C}'$ $with \mathbf{P} and \mathbf{Q}$ satisfying the Riccati equations,

$$\mathbf{P}\mathbf{A} + \mathbf{A}'\mathbf{P} + \mathbf{C}'\mathbf{C} - \frac{1}{\rho}\mathbf{P}\mathbf{B}\mathbf{B}'\mathbf{P} = 0 \tag{3.9}$$

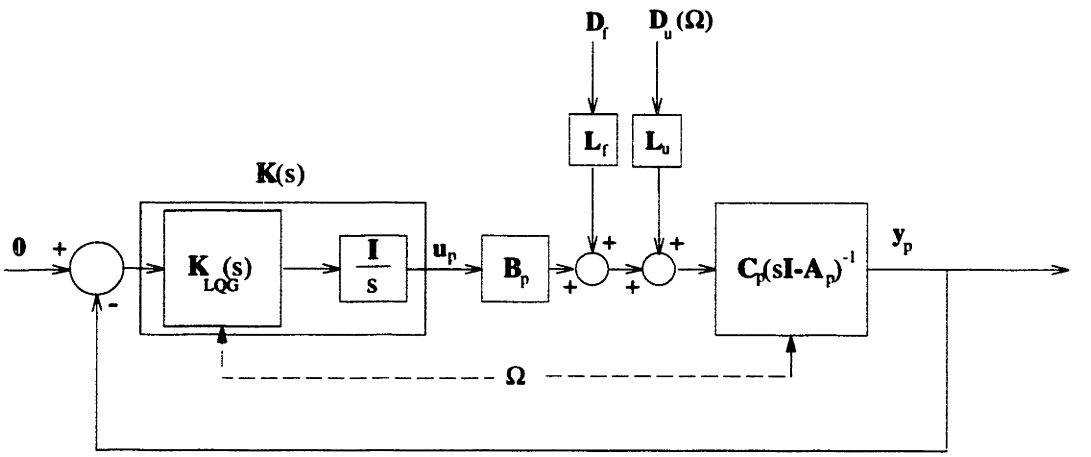

Figure 3.1: The block diagram of the closed-loop system under LTR integral control

and

$$\mathbf{AQ} + \mathbf{QA}' + \mathbf{I} - \frac{1}{\mu}\mathbf{QC}'\mathbf{CQ} = 0. \tag{3.10}$$

Notice that the definitions of matrices **A**, **B** and **C** can be found in Appendix A.

In rotating machine applications, one of the crucial factors that determine the system performance is the disturbance rejection capability. Therefore, we will focus on the disturbance-rejection related issues, namely, system stiffness (or equivalently, compliance) properties and allowable unbalances. The system compliance matrix $\mathbf{S}(s)$, which is the transfer function from the external disturbance $\mathbf{d}_f$ to the output $\mathbf{y}_p$, is given by:

$$\mathbf{S}_d(s) = \mathbf{S}(s)\mathbf{L}_d, \tag{3.11}$$

where $\mathbf{S}_d(s) = \left[\mathbf{I} + \mathbf{C}_p(s\mathbf{I} - \mathbf{A}_p)^{-1}\mathbf{B}_p\mathbf{K}(s)\right]^{-1}\mathbf{C}_p(s\mathbf{I} - \mathbf{A}_p)^{-1}$. A similar expression can also be obtained for the transfer function from the unbalance vector $\mathbf{d}_u$ to the output. However, what concerns us here is how to compute maximum "magitudes"

of the unbalances so that when they are imposed to the system, the performance constraints such as Eqs.(2.28)-(2.30) or Eqs.(2.28)-(2.30) would not be violated.

To solve this problem, let us take a close look at $\mathbf{d}_u$. Due to the sinusoidal nature of this vector and the identity $\sin(\vartheta + \frac{\pi}{2}) = \cos(\vartheta)$, to study the effect of unbalances, it is sufficient to examine how the transfer functions in question behaves at the frequency Ω in the input direction $\Omega^2 \left[j\epsilon e^{j\delta_1}, \tau e^{j\delta_2}, \epsilon e^{j\delta_1}, j\tau e^{j\delta_2}\right]^T$. For example, the quantity $\frac{di_{x1}}{dt} + \kappa \frac{dx_1}{dt}$ has a sinusoidal nature with the amplitude equal to $j\Omega^3 \left[\begin{array}{cccc} 1 & 0 & 0 & 0 \end{array}\right] (-\mathbf{K}(j\Omega) + \kappa \mathbf{I})\, \mathbf{S}(j\Omega) \mathbf{L}_u \left[\begin{array}{c} j\epsilon e^{j\delta_1} \\ \tau e^{j\delta_2} \\ \epsilon e^{j\delta_1} \\ j\tau e^{j\delta_2} \end{array}\right]$. Since

$$\left[\begin{array}{c} j\epsilon e^{j\delta_1} \\ \tau e^{j\delta_2} \\ \epsilon e^{j\delta_1} \\ j\tau e^{j\delta_2} \end{array}\right] = \left[\begin{array}{cc} j & 0 \\ 0 & 1 \\ 1 & 0 \\ 0 & j \end{array}\right] \left[\begin{array}{c} \epsilon e^{j\delta_1} \\ \tau e^{j\delta_2} \end{array}\right], \tag{3.12}$$

it is easy to see, by treating $\left[\epsilon e^{j\delta_1}, \tau e^{j\delta_2}\right]^T$ as a new input vector, that $|\frac{di_{x1}}{dt} + \kappa \frac{dx_1}{dt}| \leq v_s$ if

$$\sqrt{\epsilon^2 + \tau^2} \leq \; v_s \sigma_{max}^{-1} \left[j\Omega^3 \left[\begin{array}{cccc} 1 & 0 & 0 & 0 \end{array}\right] (-\mathbf{K}(j\Omega) + \kappa \mathbf{I})\, \mathbf{S}(j\Omega) \mathbf{L}_u \left[\begin{array}{cc} j & 0 \\ 0 & 1 \\ 1 & 0 \\ 0 & j \end{array}\right] \right] \tag{3.13}$$

for any arbitrary phase angles δ_1 and δ_2. This inequality, in which σ_{max} denotes the maximum singular value of the quantity between brackets, utilizes the fact that the maximum singular value of a tranfer function matrix represents the largest principle gain among all possible input directions [26]. Similar analysis can also be applied to obtain the upper bounds of unbalances for the other constraints. The largest quantity $\sqrt{\epsilon^2 + \tau^2}$ that meets all the performance constraints is defined as the allowable unbalance.

3.4 Achievable Performance of a Magnetically Levitated Turbo Pump

Now we use the properties of LTR controllers to investigate the achievable performance of a real machine. We are particularly interested in how the system bandwidth and hardware parameters influence the disturbance-rejection. The example used here is the magnetically levitated turbo pump discussed in [56]. Main system parameters are listed in table 3.4. In addition, the radial bearings employed, which have

System parameters	
$m = 2.2Kg$	mass
$I_a = 1.555 \times 10^{-3} Kg - m^2$	longitudinal moment of inertia
$I_r = 8.285 \times 10^{-3} Kg - m^2$	transverse moment of inertia
$a_1 = 0.0238M$	moment arm
$a_2 = 0.0691M$	moment arm
$v_s = 24volts$	supply DC voltage
$P_{max} = 72Watts$	maximum supply power

Table 3.1: System parameters

$h_0 = 2.5 \times 10^{-4} m$, $A = 9.75 \times 10^{-5} m^2$, and $n = 200turns.$ are made of laminated silicon steel with $\mathcal{B}_{sat} \approx 1.2Telsa.$ For the pupose of reducing the heat dissipation and avoiding excessive flux leakage and fringe fluxes due to the high flux intensity, a safety factor of 1.5 is adpoted and $\mathcal{B}_{sat} = 0.8Telsa$ is assumed. This leads to $\omega_n = 300.47 \frac{rads}{s}$ and $i_0 = 0.7958Amps$ when $B^* = 0.5$ is used. Consequently, we have $P^*_{max} = 33.14$ and $v^*_s = 10.34$. Now the LTR controller $\mathbf{K}(s)$ in Figure 3.1 is applied to the system by choosing $\rho = 1 \times 10^{-10}$ to recover the loop. The achievalbe performance, in terms of the system compliance and the allowable unbalance, of the control system will be investigated belowed.

Figure 3.2 and Figure 3.3 show the maximum singular value of the system compliance[2]

[2]To recover the true compliances, one has to mutiply the normalized values by a factor $\frac{r_0 \mu_0}{B^2_{sat} A}$,

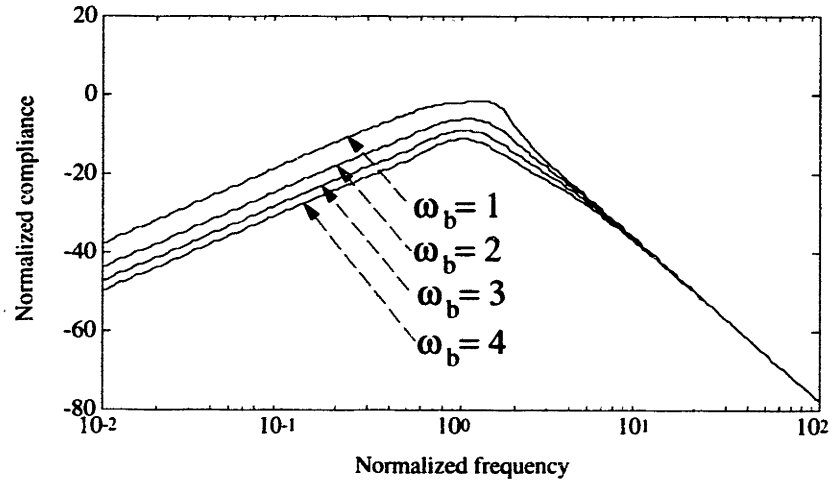

Figure 3.2: The system compliance curves of the input-state linearization scheme

$\mathbf{S}_d(j\omega)$ for these two current control schemes when the disturbance $\mathbf{F}_d$ is exerted at the first radial bearing (or $\ell = -a$) and the rotor is spinning at 25000RPM. Both figures reveal that the compliance is low at low frequencies, which is due to the integral action. Then the compliance increases with the frequency. After it reaches the maximum, the compliance decreases monotonously, and the two current control schemes present similar behavior at high frequencies regardless the system bandwidth changes. However, the input-state linearization scheme has smaller maximum compliances in the low frequency region, and its compliance curves are generally lower than those of the bias current scheme. This is possibly attributed to the fact that the input-state tranformation, which assumes that perfect linearization is possible, can cancel the actuator nonlinearities and thus eliminate the system instability; therefore, in input- state linearization scheme the controller does not have to deal with instability problems which would occurred in the bias current linearization scheme.

which equals $5.03\frac{\mu m}{N}$ in this case.

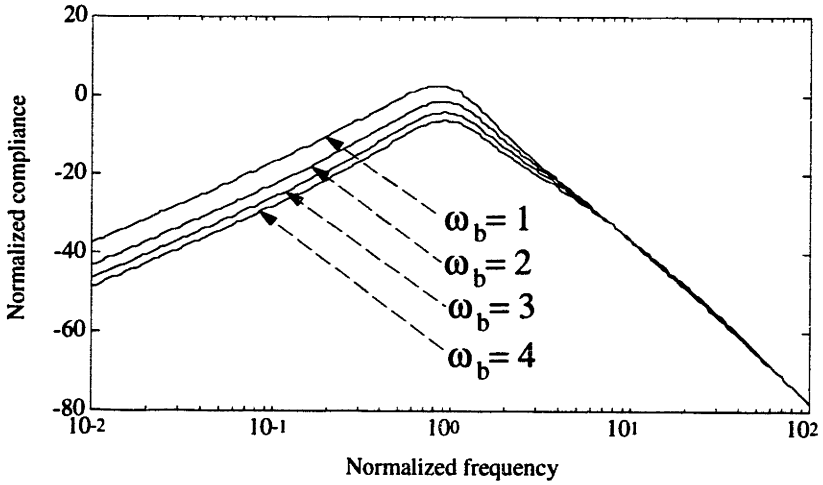

Figure 3.3: The system compliance curves of the bias current scheme

It can also be observed from Figure 3.2 and Figure 3.3 that, in either scheme, when one increase the system bandwidth, the compliance curves are lowered down accordingly. Such an observation tends to make one conclude that a high bandwith system is more favorable than a low bandwidth one. This argument is true only when unmodeled dynamics is not excited by the control action. Practically, unmodeled dynamics such as rotor flexibilities always exist and would make the model invalid at high frequencies. These effects usually prevent one from increasing the system bandwidth infinitely. The analysis on how the first mode constrains the system bandwidth can be found in Appendix B.

Figure 3.4 and Figure 3.5 show that, for both schemes, the allowable unbalance decreases as the normalized rotation speed increases and the unbalance curves get lower when one increases the system bandwidth. Since the unbalances of the rotor are fixed quantities, in order to assure that the system can pass all desired rotation speeds, the rotor unbalance $\sqrt{\epsilon^2 + \tau^2}$ has to be at least less than the minimum value

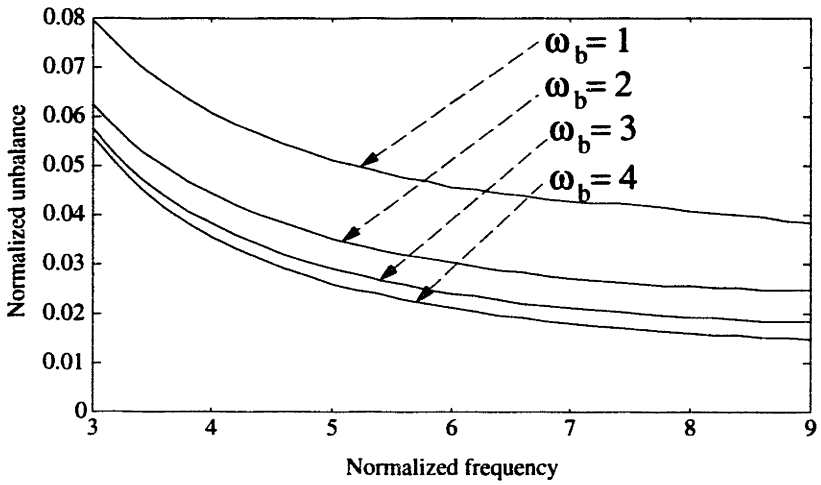

Figure 3.4: The allowable unbalance curves of the input-state linearization scheme

of unbalance curves. For example, if the system bandwidth is selected as 1 and the rated rotation speed is 25000RPM. which corresponds to a normalized speed of 8.7, this minimum value is about 0.038 for input-state linearization scheme and is about 0.023 for the bias currrent scheme. However. readers have to keep in mind that if perfect linearization is not obtained for the input-state linearization scheme. the performance may be deteriorated and the instability may occur.

Basically. increasing the bandwidth makes the system stiffer; however, the bearings also become more vulnerable to the unbalances. Figures 3.2-3.5 can be used to select a proper bandwidth so that the system not only has desired stiffness properties but is also robust enough against the expected unbalances. For instance. if the expected static unbalance. the expected dynamic disturbance, and the rated speed are known, then Figure 3.4 or Figure 3.5 can be employed to determine the minimum bandwidth so that the associated characteristic curve is above the normalized disturbance quantity across the operating speed range. Once the minimum bandwidth is

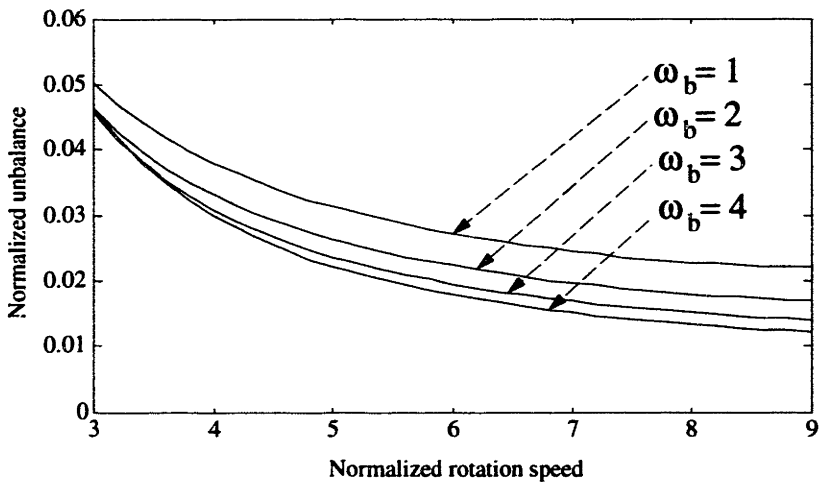

Figure 3.5: The allowable unbalance curves of the bias current scheme

acquired, one can use Figure 3.4 or Figure 3.5 to select the appropriate bandwidth which gives satisfactory compliance responses.

When designing magnetically levitated machines, plotting similar system compliance curves and allowable disturbance curves also enable engineers to check whether the hardware parameters, such as the bearing gap x_0, the pole area A,the DC supply voltage v_s, the maximum power P_{max}, the rotor inertias and the system geometry, are well-chosen. For instance, if the DC supply voltage is only $12volts$, the allowable unbalance curves for the bias current scheme appear to be those in Figure 3.6. It is shown that due to the low voltage supplied, the allowable unbalance are significantly reduced.

3.5 Summary and Remarks

An analysis procedure for evaluating the achievable performance of magentically levitated machines was presented. By applying the LTR methodology to systems in

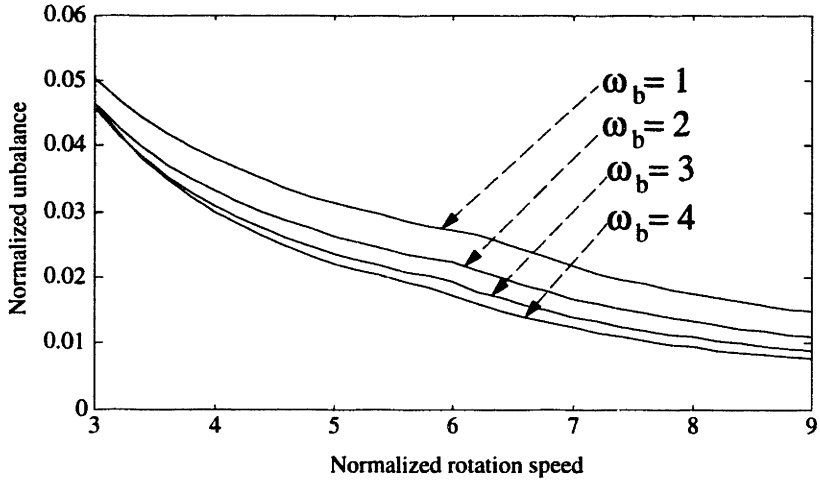

Figure 3.6: The allowable unbalance curves of the bias current scheme for $v_s = 12volts$

dimensionless form, the disturbance rejection characteristics for two different current control schemes were investigated. It was shown that while increasing the system bandwidth decreases the system compliances, the allowable unbalances are dominated by the hardware constraints. Morever, according the simulation curves, it was also observed the the input-state linearization scheme, which relies on a precise description of the actuator dynamics, generally exhibits better performance compared to the bias current scheme.

The analyi this chapter makes use of the simple model developed previously. The LTR design assumes all the system parameters are known and there is no model uncertainties. However, frequently in practical applications, the behavior of real systems is not the same as that of the theoretical model and the information about system dynamics is only partially available. As a result, linear control design such as LTR may be inappropriate and one often needs to seek different control methods that are capable of dealing with nonlinear, uncertain systems such as the magnetically

levitated rotating machines. Due to this reason, an adaptive controller for nonlinear uncertain system was proposed and will be described in Chapter 5. But in the next chapter, a model refining procedure will be first presented so that a simple but accurate model can be used later for extensive simulations and to faciliate control system design.

Chapter 4

System Idenfication and Model Refinement

4.1 Introduction

The discussions thus far use the system model developed in chapter 2. The actuator dynamics in this model, despites its simplicity, is valid only when the nonideal effects such as the flux leakage, the fringing fluxes and the eddy current are negligible. In this chapter, system identification is performed on the existing magnetically levitated turbo pump to study its dynamic behavior. Because this machine is open-loop unstable, an stabilizing linear analog compensator is used in the identification processes. The frequency responses of the theoretical actuator models are compared to the experimental results. Then a detail analysis on the magnetic fluxes is used to explain the discrepencies and provide knowledge in refining the system model.

4.2 A description of the existing analog control system

The magnetically levitated turbo pump under investigation basically utilizes the bias current linearization scheme discussed previously. Furthermore, to reduce the power consumption, one coil current in each of the opposite coil pairs is turned off if the corresponding control current becomes too excessive. Taking the thrust bearing for

example, we have

$$\begin{array}{lll} i_{zu} = i_0 + 0.5u_z, & i_{z\ell} = i_0 - 0.5u_z & \text{if } |u_z| \leq 2i_0 \\ i_{zu} = i_0 + 0.5u_z, & i_{z\ell} = 0 & \text{if } u_z > 2i_0 \\ i_{zu} = 0. & i_{z\ell} = i_0 - 0.5u_z & \text{if } u_z < 2i_0, \end{array} \quad . \tag{4.1}$$

where u_z is the control signal.

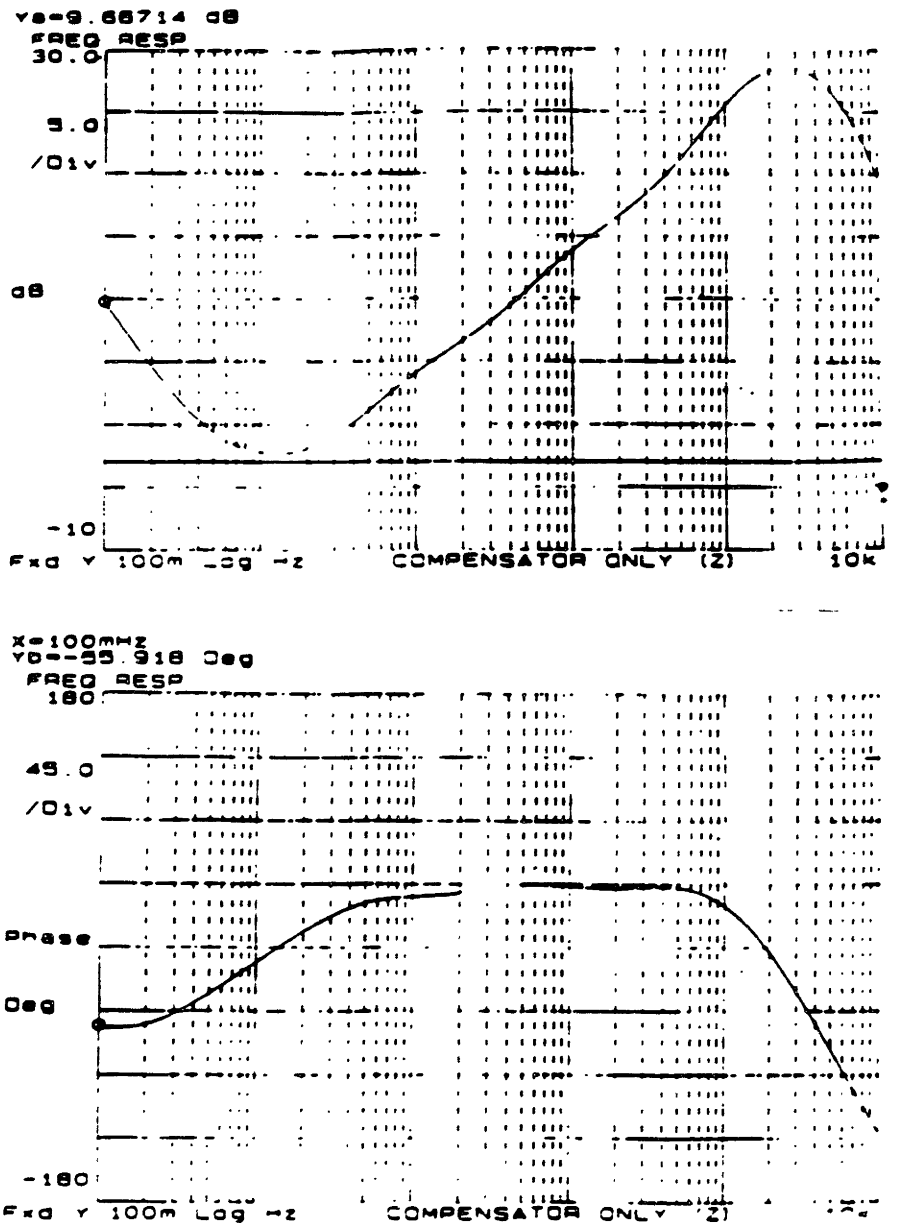

Figure 4.1: Frequency response of a typical analog compensator

This nonlinear relation in Eq. (4.1) is implemented using electronics and the resul-

tant current signals, which are in voltage form, are applied to linear power amplifiers. The power amplifiers then output appropriate coil currents to the bearings. Figure 4.2 shows the frequency responses of the power amplifier associated with the thrust bearing. Basically, the amplifier dynamics for all the five axes can be approximated by the the form:

$$g(s) = \frac{1}{(\frac{s}{2\pi\omega_n})^2 + (\frac{1.4s}{2\pi\omega_n}) + 1}, \tag{4.2}$$

in which ω_n ranges from $1KHz$ to $1.7KHz$. Because the controller bandwidth chosen later will be much less than the ω_n's. the amplifier dynamics will be ignored.

The system is also equipped with a fairly complicated linear analog compensator. The compensator circuit is made up of an integration circuit to increase static rigidity, a phase lead circuit to increase the damping force of the rotor in the intermediate frequency range. The amplitude and phase characteristics of the frequency response of a typical compensator used are shown in Figure 4.1. The compensator for the thrust bearing has six zeros and seven poles and an overall gain while that for the radial bearing has five zeros, five poles and an overall gain. Therefore, totally there are 58 parameters that need to be tuned. The control law is fixed for all operating speeds. The controller is decentralized and the design is based on linearized theoretical models ignoring the coupling effects among various axes.

The purpose of this research is to improve the bearings' stiffness properties by redesigning the control system. A simple but accurate model can greatly facilitate this design process. Because the system is unstable, as revealed by the characteristic equation such as Eq. (2.31). performing system identification in the open loop sense is not feasible. However. with the help of the analog compensator. we can still conduct frequency-response analysis to obtain the linearized dynamic behavior of the open system. The system identification procedure is described in the following section.

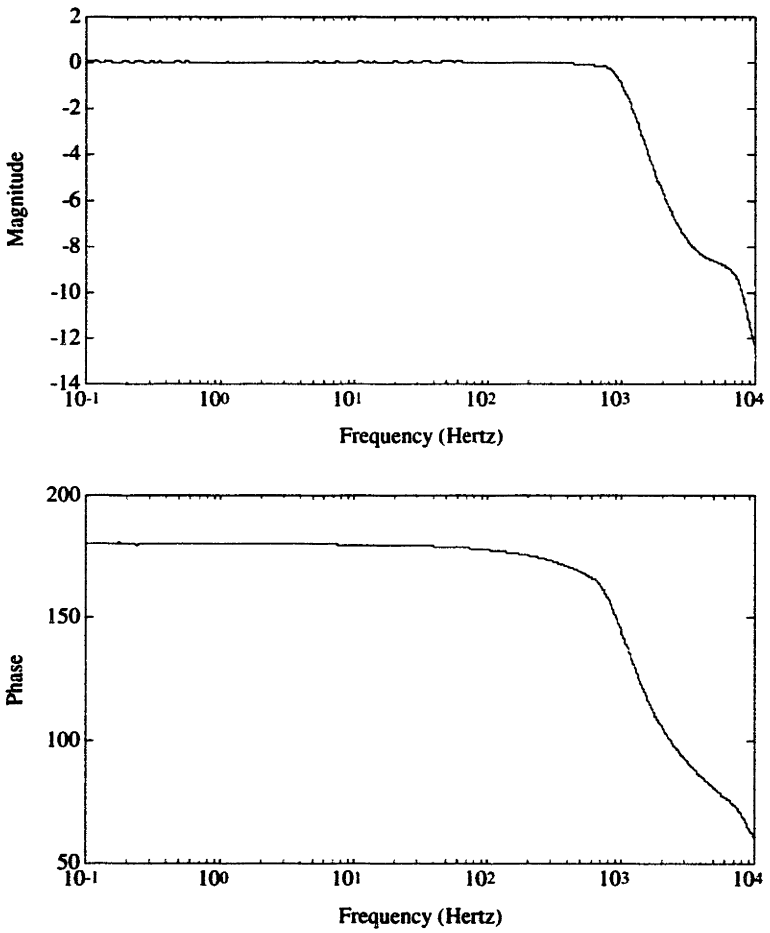

Figure 4.2: Bode plots for the power amplifier associated with the thrust bearing

4.3 System Idenfication and Linearized Dynamics

Figure 4.3 shows the experimental setup for system identification. This identification procedure is based on the frequency response tests. During the tests, the rotor was at rest and the analog controller was turned on to stabilize the system. An HP dynamic signal analyzer was used to send a swept sine signal, which acted as a disturbance, to one of the bearings. The signal frequency ranges from 0.1 Hz to 10 KHz. The

frequency response is the experimental transfer function between the output position and the input current, both measured in terms of voltage, of the associated bearing. The carrier frequency of the source signals used in the induction position sensors is $25KHz$ and the sensor dynamics is ignored in the thesis. The sensor gains are $25000\frac{V}{m}$ for the radial bearings and $9450\frac{V}{m}$ for the thrust bearing. Besides, the control currents were measured using $0.3Ohms$ sensing resistors.

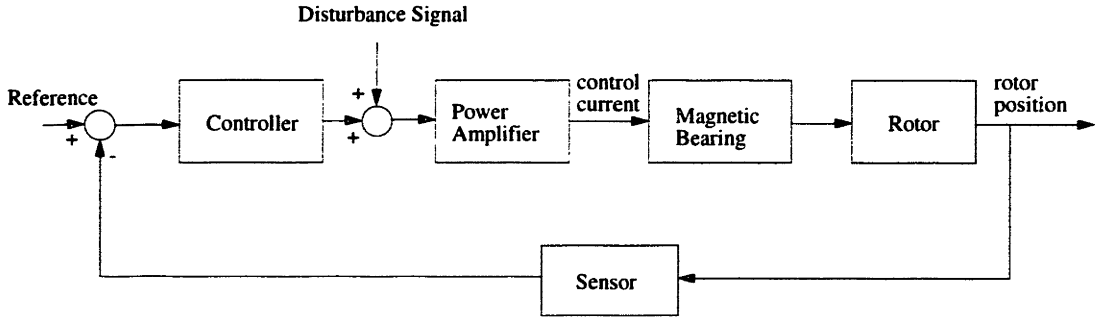

Figure 4.3: Experimental setup for the frequencey response tests

Due to the small amplitude of disturbances injected ($0.01Volts$), the frequency response tests reflect the local open-loop dynamic behavior of each bearing. The behavior depicts the linearized system dynamics around the operating point x_1, x_2, y_1, y_2, z, $\dot{x}_1$, $\dot{x}_2$, $\dot{y}_1$, $\dot{y}_2$, $\dot{z}$, u_{x1}, u_{x2}, u_{y1}, $u_{y2} = 0$, $u_z = u_{ss}$, where u_{ss} is the steady state current required to support the weight of the rotor at the nominal position.

4.3.1 Theoretical Linearized Dynamics

The system model obtained in Section 2.2 can be used to study the theoretical linearized dynamics. Take the thrust bearing for example. Assuming $u_{ss} > 2i_0$, which means $i_{zu} = i_0 + 0.5u_z$ and $i_{z\ell} = 0$, linearizing the thrust bearing dynamics gives us

$$\ddot{\delta z} = \frac{\mu_0 A n^2 u_{ss}^2}{2mh_0^3}\delta z + \frac{\mu_0 A n^2 u_{ss}}{2mh_0^2}\delta u_z. \tag{4.3}$$

where δz is a perturbed displacement due to a perturbed control current δu_z around u_{ss}. Therefore, the theoretical transfer function from δu_z to δz is given by the following expression:

$$\frac{\delta z(s)}{\delta u_z(s)} = \frac{\frac{\mu_0 A n^2 u_{ss}}{2mh_0^2}}{s^2 - \frac{\mu_0 A n^2 u_{ss}^2}{2mh_0^3}}, \tag{4.4}$$

The resultant system is obviously unstable and it has poles located at $\pm\sqrt{\frac{\mu_0 A n^2 u_{ss}^2}{2mh_0^3}}$.

Similar derivations can be applied to the radial bearings. However, it should be noticed that the radial bearing system is an MIMO system and even the rotor is at rest, x_1 and x_2 (y_1 and y_2) are coupled due to the geometic and inertia properties of the rotor-bearing assembly. The frequency response test of a single axis may not produce useful information about the linearized radial bearing dynamics. However, it is observed that during the tests, due to the control action of the analog compensator, for $\omega \leq 100Hz$ the displacements of all axes remain stationary except the axis on which the frequency response is conducted.

For example, when the disturbance signal is applied to the x_1 axis, $x_2 \approx 0$. Consequently, there is only one degree of freedom in the X direction at low frequencies and the dynamics as part of Eq. (2.3) is simplified to:

$$\ddot{x_1} = \frac{(a_1 + a_2)^2}{I_r + ma_1^2} F_{x1}, \tag{4.5}$$

in which the expression for F_{x1} id given by Eq.(2.6). At the levitated equilibrium position, the current in both electromagnets equals i_0; therefore, $u_{x1} = 0$, $x_1 = 0$, and $\dot{x}_1 = 0$. Thus the linearized model becomes:

$$\delta\ddot{x}_1 = \frac{(a_1 + a_2)^2}{I_r + ma_2^2} \frac{\kappa\mu_0 A i_0 n^2}{h_0^2} \left(\frac{\kappa i_0}{h_0} \delta x_1 + \frac{1}{2} \delta u_{x1} \right). \tag{4.6}$$

The theoretical x_1 transfer function corresponing to the frequency response test con-

ditions can be given by the following expression:

$$\frac{\delta x_1(s)}{\delta u_{x1}(s)} = \frac{\frac{(a_1+a_2)^2}{I_r+ma_2^2}\frac{\kappa\mu_0 Ai_0 n^2}{2h_0^2}}{s^2 - \frac{(a_1+a_2)^2}{I_r+ma_2^2}\frac{\kappa^2\mu_0^2 Ai_0 n^2}{h_0^3}}. \tag{4.7}$$

4.3.2 Experimental and Theoretical Frequency Responses

Now we present experimental frequency responses together with the theoretical transfer functions of the magnetic bearings. The theoretical responses are calculated using the system parameters in Table 3.4 and the bearing parameters in Table 4.3.2.

Radial Bearing	Thrust Bearing
$i_0 = 0.35 Amps$	$i_0 = 0.50 Amps$
$n = 200 turns$	$n = 133 turns$
$A = 9.75 \times 10^{-5} m^2$	$A = 7.0 \times 10^{-4} m^2$
$h_0 = 2.5 \times 10^{-4} m$	$h_0 = 4.0 \times 10^{-4} m$

Table 4.1: Magnetic bearing parameters

Figure 4.4 shows the experimental frequency response of the x_1 radial bearing. Also shown in this figure is the frequency response of the theoretical transfer function. Substituting the associated parameters into Eq. (4.7), the theoretical transfer function for the x_1 bearing is found to be

$$\frac{\delta x_1(s)}{\delta u_{x1}(s)} = \frac{65.7}{(\frac{s}{117.8})^2 - 1}(\frac{V}{V}), \tag{4.8}$$

but the experimental frequency response can be curve-fitted by the following transfer function:

$$\frac{\delta x_1(s)}{\delta u_{x1}(s)} = \frac{74.1}{(\frac{s}{81.7})^2 - 1}(\frac{V}{V}). \tag{4.9}$$

Although the model in Eq. (4.7) is valid only for $\omega \leq 100 Hz$, from Figure 4.4, it is clear that this model is not accurate enough to predict the experimental responses

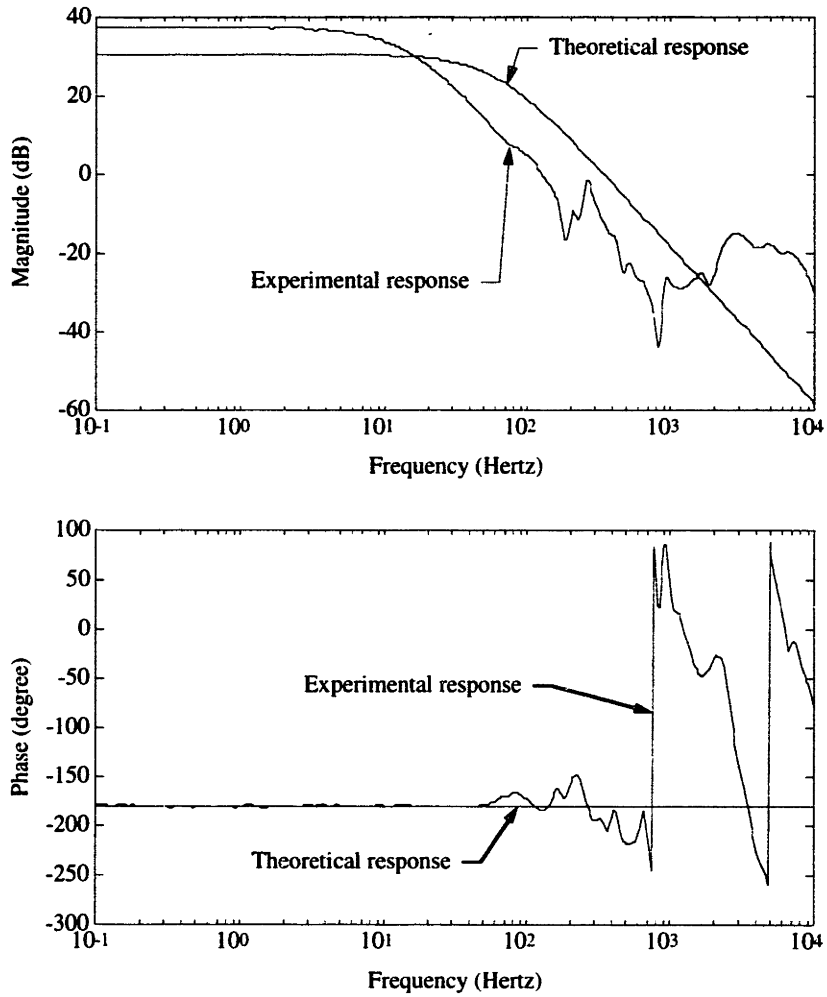

Figure 4.4: Experimental and theoretical frequency responses of the x_1 bearing

especially the DC gain and the break frequency. Before getting into the detail of how to refine the theoretical model to match the experimental behavior, let us also take a look at the frequency responses of the thrust bearing.

Figure 4.5 shows the experimental and theoretical responses. In this case, the measured steady state current $u_{ss} = 1.5 Amps$ is substitued in the theoretical model.

Different from the radial bearings, discrepencies exist not only in the DC gains and break frequencies but also in the roll-off rates. Actually, in the low frequency range, the experimental frequency response can be curve-fitted as

$$\frac{\delta z(s)}{\delta u_z(s)} = \frac{11.15}{\frac{1}{5}(\frac{s}{\omega_n})^3 + (\frac{s}{\omega_n})^2 - 1}(\frac{V}{V}), \tag{4.10}$$

where $\omega_n = 191.64\frac{rad}{s}$ (30.5 Hz), while the analytical one has the following expression:

$$\frac{\delta z(s)}{\delta u_z(s)} = \frac{8.40}{(\frac{s}{352.60})^2 - 1}(\frac{V}{V}). \tag{4.11}$$

4.4 Model Refinement

In order to refine the theoretical models, one has to examine the validity of modeling assumptions made in Section 2.2.2, namely, the flux leakage, fringing fluxes are neglected, and the core material is highly permeable. Figure 4.6 shows the typical magnetic fluxes existing in the radial bearing. Both the flux leakage and the fringing fluxes are shown in this figure. If the lumped-parameter modeling approach is still adopted, one can discretize the whole system according to the assumed flux behavior and obtain a more detailed picture. Figure 4.7.(a) presents a more precise bond graph model of the radial bearing. In this model, the magnetomotive force ni is discretized as a collection of effort sources S_e. These effort sources are connected, through 1 junctions, to the generialized capacitances C_c which models the core permeance. C_ℓ's represent the effects of the flux leakage across the legs of the electromagnet, while C_f's model the permeances of fringing fluxes. The permeances inside the rotor are also modeled by C_c's. $C_{a(.)}$ still characterize the generalized capacitance for the useful fluxes. Notice that it is also assumed in this model that magnetic forces contributed from the fringing fluxes are negligible compared to those due to the useful fluxes. This is a resonable assumption for our current system (see Appendix C). Therefore, $C_{a(.)}$'s imposes magnetic forces to the I-C field exclusively.

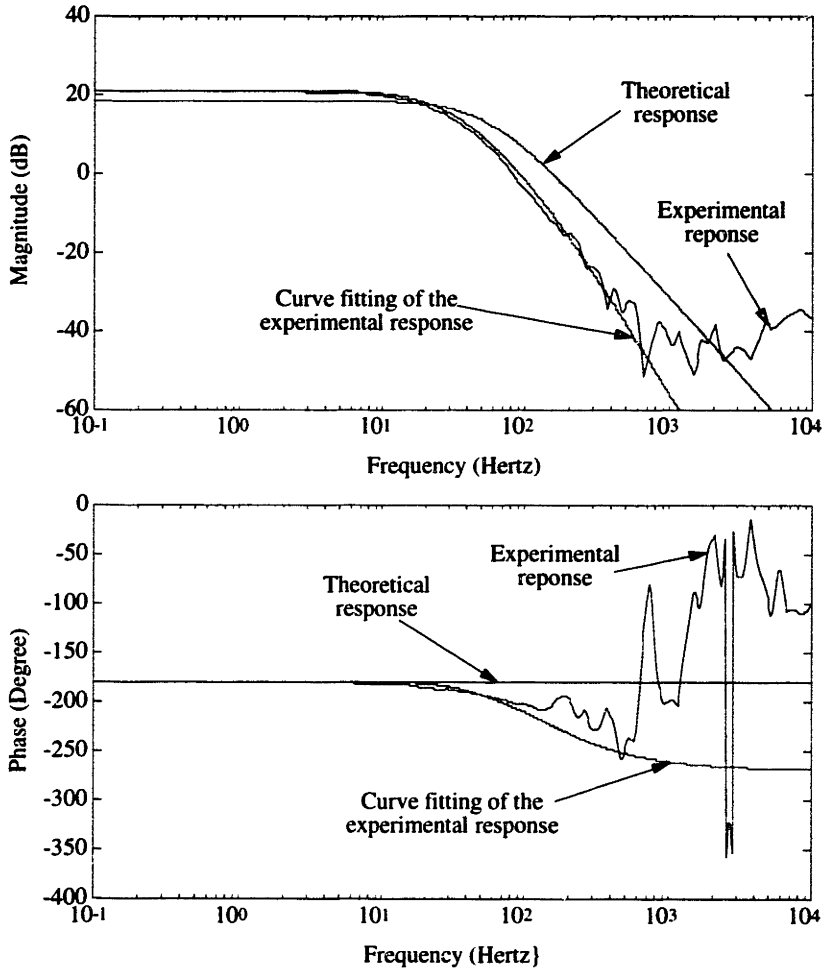

Figure 4.5: Experimental and theoretical frequency responses of the thrust bearing

Analyzing this bond graph seems to be a formidable task at the first glance. However, using Thevenin's theorem it is possible to separate C_a and the I-C field and then obtain a simple representation of the rest of the system , namely, the effort source-capacitance network. Figure 4.7.(b) shows the equivalent system model. The network consisting of effort sources and generalized capacitances is now represented by

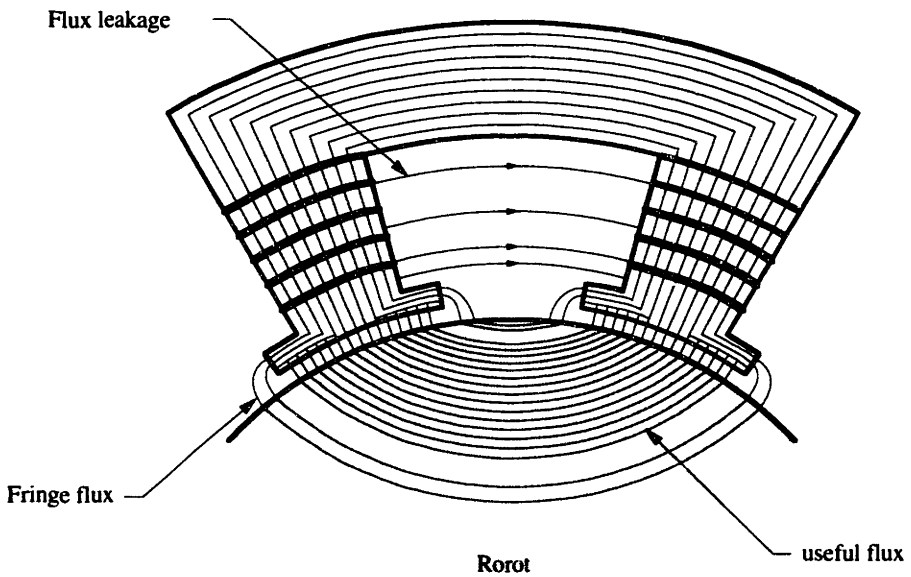

Figure 4.6: Magnetic fluxes existing in the radial bearing

an equivalent effort source αni and an equivalent linear capacitance C_{eq}. Identifying the constants α and C_{eq} using the experimental data allows us to refine the theoretical model to match the real system.

Using the casuality assignemt method in [24], it is easy to see that the system in Figure 4.7.(b) only has two energy storage elements with integral casualities [1]. This means the model is a second order system. This is compatible to the experimental results associated with the radial bearings, say. x_1, which has $-40\frac{dB}{decade}$ roll-off rate. However, the $-60\frac{dB}{decade}$ roll-off rate of experimental response for the thrust bearing implies that it is a third order system. Such a difference is due to the fact that the

[1] Because the rotor is not spinning, the I-C field behaves like pure inertial elements

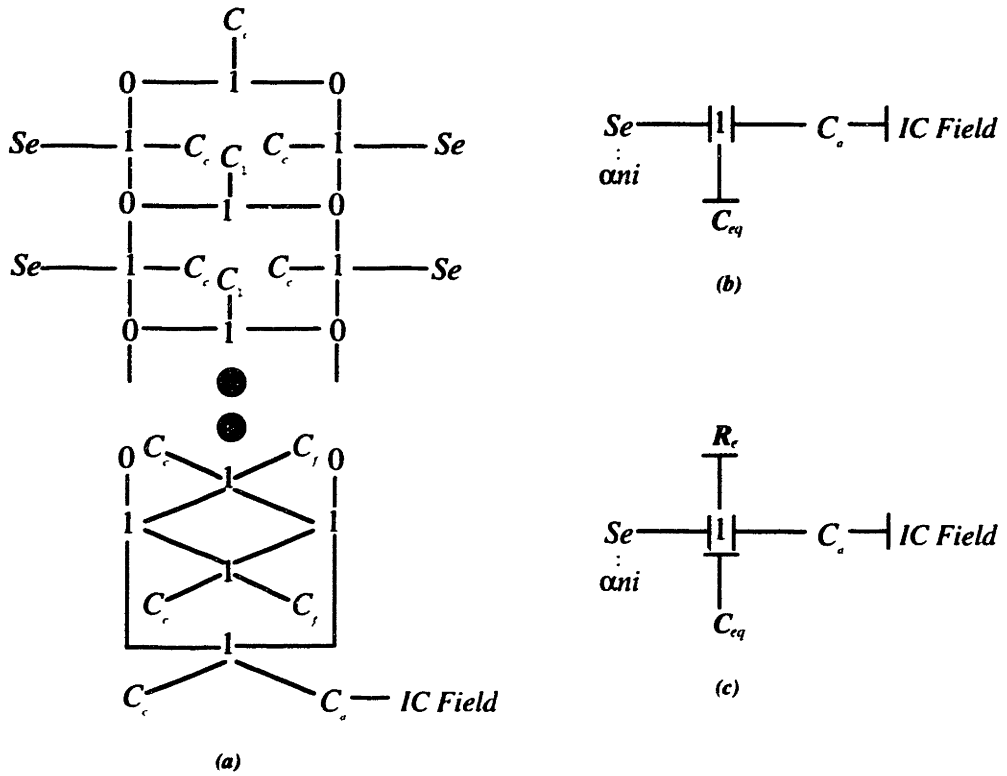

Figure 4.7: Bond graph model of the radial bearing

thrust bearing cores are not laminated so that the eddy current loss is significant. Modeling of this energy loss can be achieved by using the relation $P_{eddy} \propto (\frac{d\phi}{dt})^2$[44], where P_{eddy} is the power loss due to the eddy current, ϕ is the magnetic flux, and the proportional constant is a function of the geometry and material properties. According to the argument in the appendix, the power dissipated for the resistive element R is equal to $R\left(\frac{d\phi}{dt}\right)^2$. Therefore, we can identify the resistance induced by the eddy current by a generalized resistence R_e. The new system with R_e augumented is shown in Figure 4.7.(c). Due to the existence of the generalized resistence, one can assign integral casualities for all the capacitances and the order of the system becomes three.

Accordingly, the state equations for the thrust bearing can be written as,

$$\dot{\phi} = -\frac{1}{R_e}\left[\frac{1}{C_{eq}} + \frac{2(h_0 - z)}{\mu_0 A}\right]\phi + \frac{\alpha n}{R_e}u_z \tag{4.12}$$

$$\dot{z} = v_z \tag{4.13}$$

$$\dot{v_z} = \frac{1}{m}\frac{\phi^2}{\mu_0 A} - g, \tag{4.14}$$

and, after the linearization, the transfer function can be computed as,

$$\frac{\delta z(s)}{\delta u_z(s)} = \frac{\frac{h}{u_{ss}}}{mR_e(\frac{h}{\alpha n u_{ss}})^2 s^3 + \frac{2mh^3}{\mu_0 A(\alpha n u_{ss})^2}s^2 - 1}, \tag{4.15}$$

where $h = \frac{\mu_0}{2C_{eq}} + h_0$ is the equivalent nominal bearing gap. By comparing the coefficients of Eq. (4.15) with those of the experimental response, the constants R_e, α, h, and thus C_{eq} can be identified. Then one can use state equations such as Eq. (4.15), instead of Eqs. (2.6) and (2.7), to model the actuator dynamics more accurately. In the current application, the parameters α, h and R_e are identified for all the bearings and they are outlined in Table 4.4.

	α	h	R_e
x_1 bearing	0.8135	$282.2\mu m$	0
y_1 bearing	0.8856	$276.7\mu m$	0
x_2 bearing	0.4940	$163.0\mu m$	0
y_2 bearing	0.7656	$214.5\mu m$	0
thrust bearing	0.8318	$531.23\mu m$	$1258.8\frac{amper-turn\cdot sec}{Wb}$

Table 4.2: Magnetic bearing parameters

Among the parameters, $R_e = 0$ is assumed for all radial bearings because of the lamination. Despite the the seemingly similar configurations, bearings in the radial 2 axes are very different from those of the radial 1 axes. Particularly, the parameters α are much lower in 2 axes and the equalivent bearing gaps h are less then the nominal

gap $h_0 = 250\mu m$ [2]. This is possibly due to the fact that the 2 axis bearings were not manufactured and assembled precisely according to the specifications.

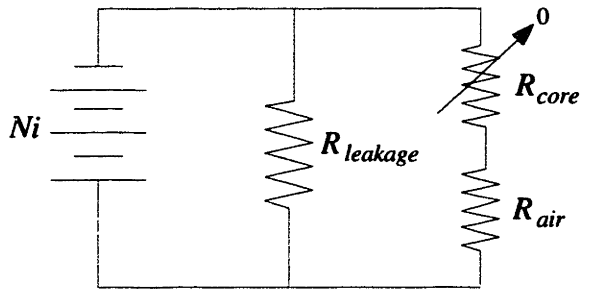

Figure 4.8: A magnetic circuit model

A different model has been suggested in [17]. This model is reproduced in Figure 4.8. Basically, there are several disadvantages associated with this model. First, the author used resistors instead of generalized capacitances to characterize the magnetic reluctances. This certainly does not capture the energy storage behavior of the magnetic field. Furthermore, the flux leakage is directly modeled as a resistor in parallel with the voltage source resulting from the magnetomotive force, and the core reluctance is only considered to be in series with air reluctance. It is obvious from Figure 4.6 and Figure 4.7 that the core reluctances and reluctances of fringe flux paths are coupled in a way that it is impossible to isolate either one of them from the other. Therefore, the refined model discussed in this thesis, which considers the detailed flux behavior, makes a better connection between the physics and the experimental data.

[2]Intuitively, the equivalent bearing gap should be larger that the nominal gap because of the additional core reluctances

4.5 Summary and Remarks

In this chapter, more detailed behavior of the magnetic bearings such as flux leakages, fringing fluxes and the eddy current loss are investigated. The use of the Thevenin's theorem to obtain simple but accurate refined models is presented. The refined models not only match the experimental linear responses but also explain the nonlinear characteristics of the magnetic forces.

Chapter 5

Adaptive Control of Nonlinear, Uncertain Systems Using Local Function Estimation

5.1 Introduction

The preceding analysis has shown that, depending on the current linearization scheme employed, the dynamics of the magnetically levitated rotating machines is either marginally stable or unstable. To achieve high performance, a stabilizing controller is absolutely required. In chapter 3, the LTR methodology is applied to investigate the achievable system performance. However, the use of this controller is only for analysis purpose. In practical applications, one usually encounters nonlinearities and uncertainties which mainly result from the magnetic bearing dynamics. These effects are not considered in the LTR design.

Furthermore, the magnetically levitated rotating machines also experience dynamic changes during the acceleration and deceleration periods. To illustrate how significant the dynamics changes, we use the state equations in Eq.(2.27) to plot the root locus of the linearized open-loop radial bearing system as the rotor spins from $0RPM$ to $30000RPM$. The result is shown in Figure 5.1. When the rotor is at rest, the system has poles at $\pm 118.9 rad/s$, $\pm 136.0 rad/s$, $\pm 263.5 rad/s$ and $\pm 265.8 rad/s$. As the rotor starts spinning, due to the gyroscopic efffect, the poles migrate toward the $j\omega$ axis and they settle at $\pm j516.8 rad/s$, $\pm j46.3 rad/s$, and $\pm 217.3 \pm j11.8 rad/s$ when the speed reaches $30,000RPM$. The LTR controller assumes that the spinning

speed of the rotor is constantly measured and used as one of the system parameters to compute the control effort. Practically, one may not have the luxury to access the spinning speed on-line and stability of the resultant time-varying controller may not be guaranteed due to the imprecise measurement, sensor noises, computational lag and so on.

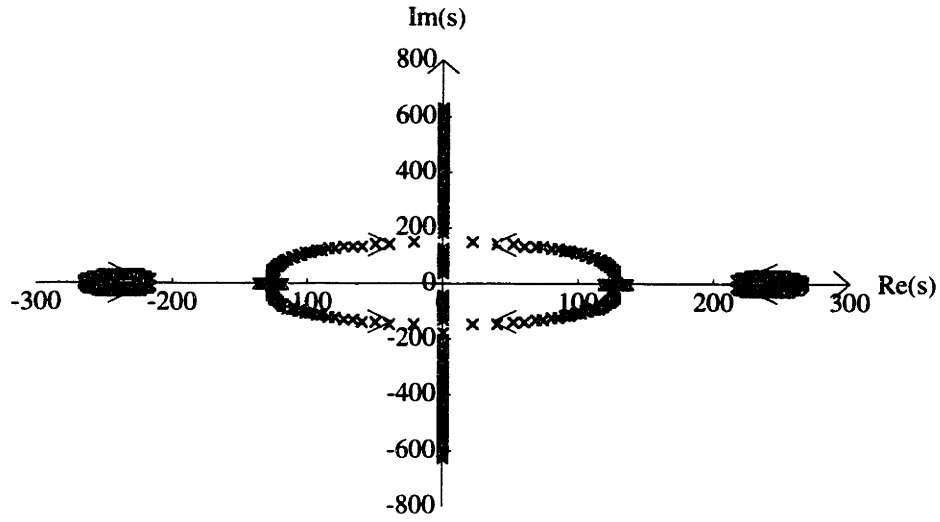

Figure 5.1: The root locus of the linearized open-loop radial bearing system

In order to directly address these critical issues associated with nonlinearities, uncertainties and changing dynamics as part of the control system design, a new adaptive control scheme is proposed. The scheme uses the local function estimation to cancel the nonlinear and uncertain dynamics present in the system and introduce some desired dynamics. With the help of a proper designed sampling rule, the neighborhood of approximation can be moved from time to time in order to capture the fast changing system dynamics. The main concept and related stability proofs are described in this chapter. Chapter 6 discusses the practical implementation issuses and presents the simulations of several dynamic systems.

5.2 Problem Statement

Consider a plant and a reference model described by

$$\dot{\mathbf{x}} = \mathbf{A}\mathbf{x} + \mathbf{f}(\mathbf{x}) + \mathbf{B}\mathbf{u} \text{ (Plant)}, \tag{5.1}$$

$$\dot{\mathbf{x}}_m = \mathbf{A}_m\mathbf{x}_m + \mathbf{B}_m\mathbf{r} \quad \text{(Reference Model)}, \tag{5.2}$$

where $\mathbf{x}$, $\mathbf{x}_m \in \mathcal{R}^n$ are the state vectors of the plant and the model respectively, $\mathbf{A}, \mathbf{A}_m \in \mathcal{R}^{n\times n}$, $\mathbf{B}, \mathbf{B}_m \in \mathcal{R}^{n\times m}$ are all known matrices and $\mathbf{A}_m$ is asymptotically stable, $\mathbf{f}(\mathbf{x}) = [f_1(\mathbf{x})\ f_2(\mathbf{x}) \ldots f_n(\mathbf{x})]^T$ is an uncertain, nonlinear vector function, $\mathbf{u} \in \mathcal{R}^m$ is a control input, and $\mathbf{r} \in \mathcal{R}^m$ is a bounded reference input. The task is to design a controller which will estimate and cancel the function $\mathbf{f}(\mathbf{x})$ on-line and force $\mathbf{x}(t)$ to follow the reference trajectory $\mathbf{x}_m(t)$. In order to define the control objective more specifically, assumptions regarding the plant and the model are made as follows.

1) *Approximation Conditions:* $\mathbf{f}(\mathbf{x})$ is smooth and there exist a constant $M_p > 0$ and a positive integer p such that $\mathbf{f}_p(\mathbf{x}, \mathbf{x}_i)$, the *pth* order Taylor's expansion of $\mathbf{f}(\mathbf{x})$ near $\mathbf{x}_i$, satisfies:

$$\|\mathbf{f}_p(\mathbf{x}, \mathbf{x}_i) - \mathbf{f}(\mathbf{x})\| \leq \frac{M_p}{(p+1)!}\|\mathbf{x} - \mathbf{x}_i\|^{p+1} \tag{5.3}$$

$\forall \mathbf{x}, \mathbf{x}_i \in \mathcal{R}^n$, where $||.||$ represents the Euclidean norm. This inequality allows one to approximate $\mathbf{f}(\mathbf{x})$ using $\mathbf{f}_p(\mathbf{x}. \mathbf{x}_i)$ when $\|\mathbf{x} - \mathbf{x}_i\|$ is sufficiently small. In fact, Eq.(5.3) is true if the $(p+1)th$ derivative of $\mathbf{f}(\mathbf{x})$ is bounded [18]. For simplicity, we would take $p = 1$ in the ensuing investigation; however, the case associated with $p > 1$ can be treated in a similar way with no further difficulties.

2) *Matching Conditions:* $Rank(\mathbf{B}) = m$, and $\forall \mathbf{x} \in \mathcal{R}^n$, there exist matrices $\mathbf{C}_0(\mathbf{x})$ and $\mathbf{C}_1(\mathbf{x})$ of order $m \times n$ such that

$$\mathbf{B}\mathbf{C}_k(\mathbf{x}) = -\mathbf{G}_k(\mathbf{x}) \tag{5.4}$$

for $k = 0, 1$, where $\mathbf{G}_0(\mathbf{x}) = diag\,[f_1(\mathbf{x}), \ldots, f_n(\mathbf{x})]$ and $[\mathbf{G}_1(\mathbf{x})]_{ij} = \left[\frac{\partial f_i(\mathbf{x})}{\partial x_j}\right]$.

3) *Controllability Conditions:* There exist matrices $\mathbf{K}$ and $\mathbf{\Delta}$ such that

$$\mathbf{A} + \mathbf{BK} = \mathbf{A}_m \text{ and } \mathbf{B\Delta} = \mathbf{B}_m. \tag{5.5}$$

Remark: Some classes of systems automatically satisfy the matching conditions in Eq.(5.4). Examples include SISO systems expressed in the canonical form:

$$x^{(n)} + f(x, \dot{x}, \ldots, x^{(n-1)}) = bu \tag{5.6}$$

with the state vector $\mathbf{x} = [x, \dot{x}, \ldots, x^{(n-1)}]^T$ and MIMO systems taking the form

$$\ddot{\mathbf{y}} + \mathbf{f}(\mathbf{y}, \dot{\mathbf{y}}) = \mathbf{Bu} \tag{5.7}$$

with the state vector $\mathbf{x} = \begin{bmatrix} \mathbf{y} \\ \dot{\mathbf{y}} \end{bmatrix}$.

5.3 An Adaptive Control Scheme Using Local Function Estimation

In this section, we formulate the idea of using local function estimation for control. Let us first introduce a controller structure. Assume that the control law for $\mathbf{u}$ is given by

$$\mathbf{u} = \mathbf{Kx} + \mathbf{\Delta r} + \mathbf{u}_{ad}, \tag{5.8}$$

where $\mathbf{Kx}$ is a full-state feedback component, $\mathbf{\Delta r}$ is a feedforward term based on the reference input $\mathbf{r}$, and $\mathbf{u}_{ad}$ is an adaptive compensating control signal. Here we use $\mathbf{u}_{ad}$ to estimate and cancel $\mathbf{f}_1(\mathbf{x}, \mathbf{x}_i)$. the first order Taylor's expansion of $\mathbf{f}(\mathbf{x})$ near $\mathbf{x}_i$. The reason for doing this is that the polynomial-like function $\mathbf{f}_1(\mathbf{x}, \mathbf{x}_i)$, which is a good approximation to $\mathbf{f}(\mathbf{x})$ in the neighborhood of $\mathbf{x}_i$, has a linearly-parameterizable form which makes the design of a fast, stable adaptation law possible. This point will be futher exploited later.

Combining Eqs.(5.1), (5.5) and (5.8) and denoting $\mathbf{B}\mathbf{u}_{ad} = -\hat{\mathbf{f}}_1(\mathbf{x}, \mathbf{x}_i)$ as the estimate of $\mathbf{f}_1(\mathbf{x}, \mathbf{x}_i)$, we then have the error dynamics

$$\dot{\mathbf{e}} = \mathbf{A}_m \mathbf{e} + \mathbf{f}_e(\mathbf{x}, \mathbf{x}_i) + \tilde{\mathbf{f}}_1(\mathbf{x}, \mathbf{x}_i), \tag{5.9}$$

where $\mathbf{e} = \mathbf{x} - \mathbf{x}_m$ is the error state vector, $\mathbf{f}_e(\mathbf{x}, \mathbf{x}_i) = [\mathbf{f}(\mathbf{x}) - \mathbf{f}_1(\mathbf{x}, \mathbf{x}_i)]$ is the approximation error between the system function $\mathbf{f}(\mathbf{x})$ and its Taylor's expansion $\mathbf{f}_1(\mathbf{x}, \mathbf{x}_i)$ and $\tilde{\mathbf{f}}_1(\mathbf{x}, \mathbf{x}_i) = \left[\mathbf{f}_1(\mathbf{x}, \mathbf{x}_i) - \hat{\mathbf{f}}_1(\mathbf{x}, \mathbf{x}_i)\right]$ is the estimation error. In this equation, $\mathbf{f}_e(\mathbf{x}, \mathbf{x}_i)$ and $\tilde{\mathbf{f}}_1(\mathbf{x}, \mathbf{x}_i)$ can be treated as two exogenous inputs to a stable, linear, time-invariant system. Consequently, to keep the tracking error within acceptable limits, these two inputs must be guaranteed to be " sufficiently small ". In other words, not only should $\mathbf{x}$ stay close enough to $\mathbf{x}_i$ so that $\mathbf{f}_1(\mathbf{x}, \mathbf{x}_i)$ can approximate $\mathbf{f}(\mathbf{x})$ well, but also a proper adaptative control law must be provided so that $\hat{\mathbf{f}}_1(\mathbf{x}, \mathbf{x}_i)$ can estimate $\mathbf{f}_1(\mathbf{x}, \mathbf{x}_i)$ accurately.

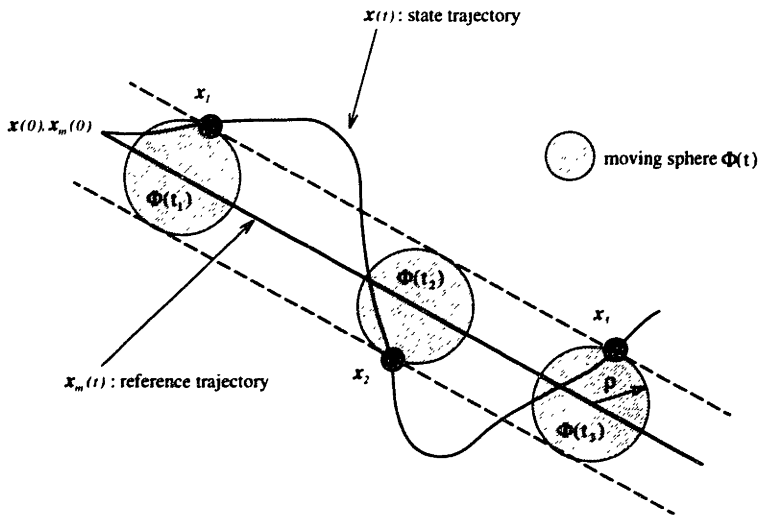

Figure 5.2: An adaptive control scheme using local function estimation

To solve these problems, an adaptive control scheme using local function estimation is proposed. The basic concept is shown in Figure 5.2. First, we define

an n dimensional " moving sphere " $\Phi(t)$ centered at $\mathbf{x}_m(t)$; i.e., $\Phi(t) = \{\mathbf{y} \in \mathcal{R}^n | \ \|\mathbf{y} - \mathbf{x}_m(t)\| \leq \rho\}$, where $\rho > 0$ is the radius of the sphere. Assume that initially $\|\mathbf{x}(0) - \mathbf{x}_m(0)\| \leq \rho$, so $\mathbf{x}(0)$ is in $\Phi(0)$. While both the full-state feedback and the feedforward terms are always used as part of $\mathbf{u}$, the adaptation term $\mathbf{u}_{ad}$ is initially set to zero. If the evolution of $\mathbf{x}$ is such that at $t = t_1$ it first " penetrates " the surface of the moving sphere $\Phi(t_1)$, or $\|\mathbf{x}(t_1) - \mathbf{x}_m(t_1)\| = \|\mathbf{e}(t_1)\| = \rho$, we sample $\mathbf{x}(t_1)$ as $\mathbf{x}_1$. The controller turns on the adaptation immediately to estimate and cancel $\mathbf{f}_1(\mathbf{x}, \mathbf{x}_1)$. Before going too far away from $\mathbf{x}_1$, $\mathbf{x}$ will be forced to return into $\Phi(t)$. Then, the controller turns off the adaptation and waits for the next time $\mathbf{x}$ leaves $\Phi(t)$. The same sampling and adaptation processes repeat for $\mathbf{x}_2, \mathbf{x}_3, \ldots, \mathbf{x}_i$ and so on.

Obviously, the key issue in this scheme is to design $\mathbf{u}_{ad}$ such that it can estimate and cancel $\mathbf{f}_1(\mathbf{x}, \mathbf{x}_i)$ properly. In view of Eq.(5.4), we express $\mathbf{f}_1(\mathbf{x}, \mathbf{x}_i)$ as

$$\mathbf{f}_1(\mathbf{x}, \mathbf{x}_i) = -\mathbf{B} \sum_{k=0}^{k=1} \mathbf{C}_k(\mathbf{x}_i) \mathbf{w}_k(\mathbf{x}, \mathbf{x}_i), \tag{5.10}$$

where $\mathbf{w}_0(\mathbf{x}, \mathbf{x}_i) = [1 \ldots 1]^T$ and $\mathbf{w}_1(\mathbf{x}, \mathbf{x}_i) = \mathbf{x} - \mathbf{x}_i$. This equation suggests that $\mathbf{u}_{ad}$ takes the form:

$$\mathbf{u}_{ad} = \sum_{k=0}^{k=1} \hat{\mathbf{C}}_k(\mathbf{x}_i, t) \mathbf{w}_k(\mathbf{x}, \mathbf{x}_i), \tag{5.11}$$

where $\hat{\mathbf{C}}_k(\mathbf{x}_i, t)$'s are the estimates of $\mathbf{C}_k(\mathbf{x}_i)$'s. Notice that the time dependency of $\hat{\mathbf{C}}_k(\mathbf{x}_i, t)$'s is due to the fact that $\mathbf{C}_k(\mathbf{x}_i)$'s will be on-line estimated using the adaptation laws presented later.

$\hat{\mathbf{C}}_k(\mathbf{x}_i, t)$'s are functions of time t as well as $\mathbf{x}_i$.

since their Substituting Eqs.(5.10) and (5.11) into Eq.(5.9), we get

$$\dot{\mathbf{e}} = \mathbf{A}_m \mathbf{e} + \mathbf{f}_e(\mathbf{x}, \mathbf{x}_i) + \mathbf{B} \sum_{k=0}^{k=1} \hat{\mathbf{C}}_k(\mathbf{x}_i, t) \mathbf{w}_k(\mathbf{x}, \mathbf{x}_i), \tag{5.12}$$

where $\tilde{\mathbf{C}}_k(\mathbf{x}_i,t) = \hat{\mathbf{C}}_k(\mathbf{x}_i,t) - \mathbf{C}_k(\mathbf{x}_i)$ for $k = 0, 1$. Here $\hat{\mathbf{C}}_k(\mathbf{x}_i,t)$'s can be treated as the estimation error matrices, and we will denote them by $\tilde{\mathbf{C}}_k$'s for simplicity from now on.

To derive a stable adaptation law for $\hat{\mathbf{C}}_k(\mathbf{x}_i,t)$'s, we first observe that $\mathbf{A}_m$ is asymptotically stable, so there exists a matrix $\mathbf{P}$ so that

$$\mathbf{A}_m^T\mathbf{P} + \mathbf{P}\mathbf{A}_m = -\mathbf{I}. \tag{5.13}$$

Such a $\mathbf{P}$ matrix allows us to define a Lyapunov function $\mathcal{V}$, where

$$\mathcal{V}(\mathbf{x}_i,t) = \frac{1}{2}\mathbf{e}^T\mathbf{P}\mathbf{e} + \frac{1}{2\gamma}\sum_{k=0}^{k=1} Tr\left[\tilde{\mathbf{C}}_k^T\tilde{\mathbf{C}}_k\right] \tag{5.14}$$

for each $\mathbf{x}_i$. Note that γ is the adaptation gain and $Tr[.]$ represents the trace of the quantity in question. Using Eqs.(5.12) and (5.13), $\dot{\mathcal{V}}$, the time derivative of $\mathcal{V}$ along the state trajectory, can be calculated as

$$\begin{aligned}\dot{\mathcal{V}} &= -\frac{1}{2}\mathbf{e}^T\mathbf{e} + \mathbf{e}^T\mathbf{P}\mathbf{f}_\epsilon(\mathbf{x},\mathbf{x}_i) + \mathbf{e}^T\mathbf{P}\mathbf{B}\sum_{k=0}^{k=1}\tilde{\mathbf{C}}_k\mathbf{w}_k(\mathbf{x},\mathbf{x}_i) \\ &\quad + \frac{1}{\gamma}\sum_{k=0}^{k=1} Tr\left[\dot{\tilde{\mathbf{C}}}_k^T\tilde{\mathbf{C}}_k\right].\end{aligned} \tag{5.15}$$

Because $\mathbf{C}_k(\mathbf{x}_i)$'s are constant matrices for a given $\mathbf{x}_i$, if we apply the adaptation law

$$\begin{aligned}\dot{\hat{\mathbf{C}}}_k(\mathbf{x}_i,t) &= -\gamma\mathbf{B}^T\mathbf{P}\mathbf{e}\mathbf{w}_k^T(\mathbf{x},\mathbf{x}_i) \quad \text{when } \|\mathbf{e}\| \geq \rho \\ &= 0 \qquad\qquad\qquad\qquad \text{otherwise}\end{aligned} \tag{5.16}$$

for $k = 0, 1$ and use the relation $Tr(\mathbf{a}\mathbf{b}^T) = \mathbf{b}^T\mathbf{a}$, where $\mathbf{a}$ and $\mathbf{b}$ are column vectors, Eq.(5.15) becomes

$$\dot{\mathcal{V}} = -\frac{1}{2}\mathbf{e}^T\mathbf{e} + \mathbf{e}^T\mathbf{P}\mathbf{f}_\epsilon(\mathbf{x},\mathbf{x}_i) \tag{5.17}$$

for $\|\mathbf{e}\| \geq \rho$.

Before investigating further the stability of the control system, we first show the following lemmas.

Lemma 5.3.1 *Every element in the matrices* $\mathbf{G}_k(\mathbf{x})$*'s in Eq.(5.4) is bounded for all* $\mathbf{x}$ *in* $\mathcal{B}$*, where*[1] $\mathcal{B} = \{\Phi(t) | \forall t \geq 0\}$.

Proof: Using the fact that $\mathbf{A}_m$ is asymptotically stable and $\mathbf{r}$ is bounded, obviously $\mathbf{x}_m(t)$ is bounded $\forall t \geq 0$. $\mathcal{B}$ is also bounded because of the triangle inequality $\|\mathbf{y}\| \leq \|\mathbf{x}_m(t)\| + \rho \ \forall \mathbf{y} \in \Phi(t)$. Then, $\bar{\mathcal{B}}$, the closure of $\mathcal{B}$, is closed and bounded. From the smoothness of $\mathbf{f}(\mathbf{x})$, one can conclude that elements of matrices $\mathbf{G}_k(\mathbf{x})$'s are bounded on $\bar{\mathcal{B}}$[5], thus on $\mathcal{B}$. □

Lemma 5.3.2 *The* $\mathbf{C}_0(\mathbf{x})$ *and* $\mathbf{C}_1(\mathbf{x})$ *matrices in Eq.(5.4) are unique.*

Proof: Assume, for example, there exists another $\mathbf{C}_0'(\mathbf{x})$ matrix such that $\mathbf{B}\mathbf{C}_0'(\mathbf{x}) = -\mathbf{G}_0(\mathbf{x})$. Substracting this equation from Eq.(5.4) with $k = 0$, we get $\mathbf{B}\left(\mathbf{C}_0(\mathbf{x}) - \mathbf{C}_0'(\mathbf{x})\right) = \mathbf{0}$. Since all the m-dimensional column vectors of $\mathbf{C}_0(\mathbf{x}) - \mathbf{C}_0'(\mathbf{x})$ are perpendicular to the $\mathbf{B}$ matrix's row vectors , which spans $\mathcal{R}^m$ because of the assumption $rank(\mathbf{B}) = m$, it is required that $\mathbf{C}_0(\mathbf{x}) - \mathbf{C}_0'(\mathbf{x}) = \mathbf{0}$. Thus. $\mathbf{C}_0(\mathbf{x})$ is unique. The same proof also applies to $\mathbf{C}_1(\mathbf{x})$. □

The above two lemmas establish the following corollary.

Corollary 5.3.1 *There exist constants* $N_0, N_1 > 0$ *such that* $Tr\left[\mathbf{C}_k^T(\mathbf{x}_i)\mathbf{C}_k(\mathbf{x}_i)\right] < N_k$ *for all* $\mathbf{x}_i$*'s and* $k = 0, 1$.

Proof: Inferring from Lemma 5.3.2, for $k = 0, 1$, elements of matrices $\mathbf{C}_k(\mathbf{x})$ can be solved as unique linear combinations of $[\mathbf{G}_k(\mathbf{x})]_{ij}$'s. Because of Lemma 5.3.1 and the definition of the trace function, $\sum_{k=0}^{k=1} Tr\left[\mathbf{C}_k^T(\mathbf{x})\mathbf{C}_k(\mathbf{x})\right]$ is bounded on $\mathcal{B}$. In particular, since $\mathbf{x}_i \in \mathcal{B}\ \forall i$, the result immediately follows. □

Now we turn to the stability issue. Let us temporarily assume that $\|\mathbf{f}_\epsilon(\mathbf{x}, \mathbf{x}_i)\| = \|\mathbf{f}(\mathbf{x}) - \mathbf{f}_1(\mathbf{x}, \mathbf{x}_i)\| \leq \epsilon$ for $\|\mathbf{e}\| \geq \rho$. Selecting $\rho = 4\|\mathbf{P}\|\epsilon$, where $\|\mathbf{P}\|$ is the induced

[1] $\mathcal{B}$ can be imagined as an n-dimensional tube.

matrix norm of $\mathbf{P}$ associated with the Euclidean norm, from Eq.(5.17) one obtains

$$\begin{aligned}\dot{\mathcal{V}} &\leq -\frac{1}{2}\|\mathbf{e}\|^2 + \|\mathbf{P}\| \cdot \|\mathbf{e}\| \cdot \|\mathbf{f}_e(\mathbf{x}, \mathbf{x}_i)\| \\ &\leq -\frac{1}{2}\|\mathbf{e}\|^2 + \frac{\rho}{4}\|\mathbf{e}\| \leq -\frac{\rho^2}{4} \end{aligned} \tag{5.18}$$

for $\|\mathbf{e}\| \geq \rho$, or $\dot{\mathcal{V}}(t)$ is upper bounded by $-\frac{\rho^2}{4}$ outside $\Phi(t)$. Such a condition allows us to claim the following lemma.

Lemma 5.3.3 *If $\|\mathbf{f}_e(\mathbf{x}, \mathbf{x}_i)\| \leq \epsilon$ for $\|\mathbf{e}\| \geq \rho$ and the $\hat{\mathbf{C}}_k(\mathbf{x}_i, t)$'s are initialized to zero matrices whenever $\mathbf{x}$ leaves Φ, then $\mathbf{x}$ has to return into Φ in finite time.*

Proof: Assume that $\mathbf{x}$ leaves Φ at $t = t_i$; i.e., $\mathbf{x}_i = \mathbf{x}(t_i)$. If $\|\mathbf{e}(t)\| \geq \rho \ \forall t \geq t_i$, then the Lyapunov function satisfies $\mathcal{V}(t_i) - \frac{\rho^2}{4}(t - t_i) \geq \mathcal{V}(t)$ because of Eq.(5.18). Equivalently, we have

$$\begin{aligned}&\left(\frac{1}{2}\mathbf{e}^T\mathbf{P}\mathbf{e} + \frac{1}{2\gamma}\sum_{k=0}^{k=1} Tr\left[\tilde{\mathbf{C}}_k^T\tilde{\mathbf{C}}_k\right]\right)\Big|_{(t=t_i)} - \frac{\rho^2}{4}(t - t_i) \\ &\qquad \geq \left(\frac{1}{2}\mathbf{e}^T\mathbf{P}\mathbf{e} + \frac{1}{2\gamma}\sum_{k=0}^{k=1} Tr\left[\tilde{\mathbf{C}}_k^T\tilde{\mathbf{C}}_k\right]\right)\Big|_t . \end{aligned} \tag{5.19}$$

Since $\sum_{k=0}^{k=1} Tr\left[\tilde{\mathbf{C}}_k^T\tilde{\mathbf{C}}_k\right] \geq 0$ and $\lambda_{min}[\mathbf{P}]\|e\|^2 \leq \mathbf{e}^T\mathbf{P}\mathbf{e} \leq \lambda_{max}[\mathbf{P}]\|e\|^2$, where $\lambda[\cdot]$ represents the eigenvalue of the corresponding matrix, the above inequality can be rewritten as

$$\begin{aligned}&\left(\frac{\lambda_{max}[\mathbf{P}]\|\mathbf{e}\|^2}{2} + \frac{1}{2\gamma}\sum_{k=0}^{k=1} Tr\left[\tilde{\mathbf{C}}_k^T\tilde{\mathbf{C}}_k\right]\right)\Big|_{(t=t_i)} - \frac{\rho^2}{4}(t - t_i) \\ &\qquad \geq \left(\frac{\lambda_{min}[\mathbf{P}]\|\mathbf{e}\|^2}{2}\right)\Big|_t . \end{aligned} \tag{5.20}$$

Moreover, $\hat{\mathbf{C}}_k(\mathbf{x}_i, t_i) = \mathbf{0}$ due to the initialization, so $\dot{\tilde{\mathbf{C}}}_k|_{(t=t_i)} = \mathbf{C}_k(\mathbf{x}_i)$. Eq.(5.20) is further reduced to

$$\begin{aligned}&\frac{1}{2\gamma}\sum_{k=0}^{k=1} Tr\left[\mathbf{C}_k^T(\mathbf{x}_i)\mathbf{C}_k(\mathbf{x}_i)\right] + \left(\frac{\lambda_{max}[\mathbf{P}]\|\mathbf{e}\|^2}{2}\right)\Big|_{(t=t_i)} \\ &\qquad - \frac{\rho^2}{4}(t - t_i) \geq \left(\frac{\lambda_{min}[\mathbf{P}]\|\mathbf{e}\|^2}{2}\right)\Big|_t . \end{aligned} \tag{5.21}$$

Using the relations $\|\mathbf{e}(t)\| \geq \rho$, $\|\mathbf{e}(t_i)\| = \rho$ and the constants N_0, N_1 in Corollary 5.3.1, we finally get

$$\frac{\lambda_{max}[\mathbf{P}]\rho^2}{2} + \frac{N_0 + N_1}{2\gamma} - \frac{\rho^2}{4}(t - t_i) \geq \frac{\lambda_{min}[\mathbf{P}]\rho^2}{2}, \tag{5.22}$$

or

$$t - t_i \leq 2\left[\lambda_{max}[\mathbf{P}] - \lambda_{min}[\mathbf{P}]\right] + \frac{2(N_0 + N_1)}{\gamma\rho^2}. \tag{5.23}$$

Consequently, the number $(t - t_i)$ must be bounded from above for all i's, which concludes that $\mathbf{x}$ can only stay outside Φ for a finite period of time. □

The argument just shown was mainly based on the assumption that $\|\mathbf{f}_e(\mathbf{x}, \mathbf{x}_i)\| \leq \epsilon = \frac{\rho}{4\|\mathbf{P}\|}$ for $\|\mathbf{e}\| \geq \rho$. This condition can be guaranteed by the following theorem.

Theorem 5.3.1 *For the adaptive control scheme proposed, if there exist positive numbers*[2] *r and δ such that $\|\mathbf{B}_m\mathbf{r}(t)\| \leq r$ for all $t \geq 0$ and*

$$\frac{1}{M_m}\left(\sqrt{\frac{\rho}{2\|\mathbf{P}\|M_1}} - \phi - \rho - \delta\right) \geq \frac{2(N_0 + N_1)}{\gamma\rho^2} + 2\left(\lambda_{max}[\mathbf{P}] - \lambda_{min}[\mathbf{P}]\right), \tag{5.24}$$

then $\|\mathbf{f}_e(\mathbf{x}, \mathbf{x}_i)\| \leq \epsilon = \frac{\rho}{4\|\mathbf{P}\|}$ for $\|\mathbf{e}(t)\| \geq \rho$. where $M_m = (\|\mathbf{A}_m\| \cdot \|\mathbf{x}_m(0)\| + r)\sqrt{\frac{\lambda_{max}[\mathbf{P}]}{\lambda_{min}[\mathbf{P}]}} + 2r$ and $\phi = \left(\frac{\lambda_{max}[\mathbf{P}]}{\lambda_{min}[\mathbf{P}]}\rho^2 + \frac{N_0+N_1}{\gamma\lambda_{min}[\mathbf{P}]}\right)^{\frac{1}{2}}$.

Proof: See Appendix E.

Basically, this theorem says that if the state trajectory can return into the moving sphere before the dyanmics changes too much, then the approximation error would be small. The term on the left side of Eq.(5.24) represents the time scale that the dynamics would change. the term on the right indicates how fast $\mathbf{x}$ can go back to the sphere.

The next corollary follows from the proof of Theorem 5.3.1 immediately.

[2] δ can be arbitrarily small.

Corollary 5.3.2 *If conditions in Theorem 5.3.1 are satisfied, then* $\|\mathbf{e}(t)\| \leq \phi$ *for all* $t \geq 0$.

Obviously, this corollary gives us a bounded tracking error. However, previous derivations requires that the initial condition $\|\mathbf{e}\|$ should be less than ρ and the $\hat{\mathbf{C}}_k(\mathbf{x}_i, t)$ matrices are initialized to zero whenever $\mathbf{x}$ leaves the moving sphere. Therefore, only localy stability can be guaranteed for this adaptive controller.

Notice that turning off the adaptation inside $\Phi(t)$ assures the boundness of the matrices $\hat{\mathbf{C}}_k$'s. This, and Theorem 5.3.1, together with Corollary 5.3.2, provide a sufficient condition for stability. Particularly, Eq. (5.24) can be used as a guide-line for selecting the adaptation gain (γ), the reference model dynamics ($\mathbf{A}_m$, thus $\mathbf{P}$) based on the prior knowledge about the uncertain dynamics (N_0, N_1 and M_1), the initial condition ($\mathbf{x}_m(0)$) and the reference input (r) to achieve the specified tracking acccuacy ($\|\mathbf{e}\| \approx \rho$). Besides, according to Corollary 5.3.2, in face of large uncertainty, the controller could inevitably require a high adaptation gain in order to have accurate tracking.

Besides $p = 1$, one can simply use the zeroth order Taylor's expansion to approximate $\mathbf{f}(\mathbf{x})$; i.e., take $p = 0$, and the resultant controller will have a PID like structure. Furthermore, the controller design procedure can be extended to the case $p > 1$. In this case, matching conditions similar to Eq.(5.4) need to be satisfied when $\mathbf{f}_p(\mathbf{x}, \mathbf{x}_i)$ is expressed in a linearly parametrized form as Eq.(5.10).

Because it is difficult to present results for higher order approximation concisely as what was done previously, we will use a simple example to illustrate the idea. Assume that $\mathbf{x} = [x_1, x_2, x_3]^T$ and the vectorial function $\mathbf{f}(\mathbf{x})$ has two components f_1 and f_2. If approximating $\mathbf{f}(\mathbf{x})$ using its second order Taylor's expansion is of interest, in addition to the matching conditions in Section 5.2, there should also exist a matrix

$\mathbf{C}_2(\mathbf{x})$ of order $m \times 6$ so that

$$\mathbf{B}\mathbf{C}_2(\mathbf{x}) = -\mathbf{G}_2(\mathbf{x}) \tag{5.25}$$

where

$$\mathbf{G}_2(\mathbf{x}) = \begin{bmatrix} \frac{\partial f_1}{\partial x_1^2} & \frac{\partial f_1}{\partial x_1 \partial x_2} & \frac{\partial f_1}{\partial x_1 \partial x_3} & \frac{\partial f_1}{\partial x_2^2} & \frac{\partial f_1}{\partial x_2 \partial x_3} & \frac{\partial f_1}{\partial x_3^2} \\ \frac{\partial f_2}{\partial x_1^2} & \frac{\partial f_2}{\partial x_1 \partial x_2} & \frac{\partial f_2}{\partial x_1 \partial x_3} & \frac{\partial f_2}{\partial x_2^2} & \frac{\partial f_2}{\partial x_2 \partial x_3} & \frac{\partial f_2}{\partial x_3^2} \\ \frac{\partial f_3}{\partial x_1^2} & \frac{\partial f_3}{\partial x_1 \partial x_2} & \frac{\partial f_3}{\partial x_1 \partial x_3} & \frac{\partial f_3}{\partial x_2^2} & \frac{\partial f_3}{\partial x_2 \partial x_3} & \frac{\partial f_3}{\partial x_3^2} \end{bmatrix}. \tag{5.26}$$

If such an additional matching condition also holds, one can express $\mathbf{f}_2(\mathbf{x}, \mathbf{x}_i)$, the second order Taylor's expansion of $\mathbf{f}(\mathbf{x})$ at $\mathbf{x}_i$, as

$$\mathbf{f}_2(\mathbf{x}, \mathbf{x}_i) = -\mathbf{B} \sum_{k=0}^{k=2} \mathbf{C}_k(\mathbf{x}_i)\mathbf{w}_k(\mathbf{x}, \mathbf{x}_i), \tag{5.27}$$

in which $\mathbf{w}_0(\mathbf{x}, \mathbf{x}_i)$ and $\mathbf{w}_1(\mathbf{x}, \mathbf{x}_i)$ are the same as those in Eq.(5.10) and

$$\mathbf{w}_2(\mathbf{x}, \mathbf{x}_i) = \begin{bmatrix} (x_1 - x_{1i})^2 \\ (x_1 - x_{1i})(x_2 - x_{2i}) \\ (x_1 - x_{1i})(x_3 - x_{3i}) \\ (x_2 - x_{2i})^2 \\ (x_2 - x_{2i})(x_3 - x_{3i}) \\ (x_3 - x_{3i})^2 \end{bmatrix}. \tag{5.28}$$

In the above equation, x_{1i}, x_{2i} and x_{3i} are the components of $\mathbf{x}_i$. After the parametrization such as Eq.(5.27) is obtained, deriving the adaptation law becomes straightforward. Nevertheless, it should be noticed that the term $\sqrt{\frac{\rho}{2\|\mathbf{P}\|M_1}}$ in Eq.(5.24) has to be replaced with $\sqrt[p+1]{\frac{(p+1)!\rho}{4\|\mathbf{P}\|M_p}}$ accordingly. Generally speaking, choosing p properly can improve the system performance because the uncertain, nonlinear system function can be estimated and cancelled more effectively.

The discussion up to now assumed that $\mathbf{B}$ is known. If $\mathbf{B}$ is constant but unknown, adaptation laws can still be derived using a similar approach. However, the first of the controllability conditions in Eq.(5.5) should be modified to

$$\mathbf{A} + \mathbf{B}_m\mathbf{K} = \mathbf{A}_m, \tag{5.29}$$

and the controller structure in Eq.(5.8) also needs to be changed to

$$\mathbf{u} = \hat{\mathbf{\Delta}} \left(\mathbf{Kx} + \mathbf{r} + \mathbf{u}_{ad} \right), \tag{5.30}$$

where $\hat{\mathbf{\Delta}}$ is the estimate of $\mathbf{\Delta}$[3]. Adding $\frac{1}{2\gamma} Tr\left[\mathbf{\Psi}^T \mathbf{\Psi}\right]$ to the Lyapunov function $\mathcal{V}$ with $\mathbf{\Psi} = \mathbf{\Delta}^{-1} - \hat{\mathbf{\Delta}}^{-1}$, one can obtain the adaptation laws as

$$\begin{aligned} \dot{\hat{\mathbf{C}}}_k(\mathbf{x}_i, t) = & \quad -\gamma \mathbf{B}_m^T \mathbf{P} \mathbf{e} \mathbf{w}_k^T(\mathbf{x}, \mathbf{x}_i) \quad \text{when } \|\mathbf{e}\| \geq \rho \\ = & \quad 0 \quad \text{otherwise} \end{aligned} \tag{5.31}$$

for $k = 0, 1$, and

$$\begin{aligned} \dot{\hat{\mathbf{\Delta}}} = & \quad -\gamma \hat{\mathbf{\Delta}} \mathbf{B}_m^T \mathbf{P} \mathbf{e} \mathbf{u}^T \hat{\mathbf{\Delta}} \quad \text{when } \|\mathbf{e}\| \geq \rho \\ = & \quad 0 \quad \text{otherwise.} \end{aligned} \tag{5.32}$$

Since the new Lyapunov function is not radially unbounded in the space of $\left\{\mathbf{e}, \hat{\mathbf{C}}_k\text{'s}, \hat{\mathbf{\Delta}}\right\}$, the stability result is further localized [32].

5.4 Summary and Remarks

In this chapter, an adaptive scheme for controlling nonlinear, uncertain systems using local function estimation concept is introduced. By making some mild assumptions about the system functions and selecting the control parameters properly, global stability can be guaranteed. Compared to other control methods, this scheme has a simpler structure which is more suitable for practical implementation. Nevertheless, several modifications still have to be made in the control law to avoid exciting the unmodeled dynamics, to reduce the noise sensitivity and to accommodate the various signal levels in system response. These issues are addressed in the next chapter.

[3] $\mathbf{\Delta}$ is assumed to be invertible in this case.

Chapter 6

Practical Implementation Issues and Simulations of the Adaptive Controller

In this chapter, several practical issues associated with implementing the proposed adaptive controller are first addressed. Then the important features and performance of the proposed controller are illustrated through simulations of some physical examples. Finally, comparisons of the adaptive controller with other control schemes are given.

6.1 Practical Implementation Issues

In this section, several modifications are suggested to make the implementation of the control scheme practical.

6.1.1 Avoiding Discontinuity in Control

For the $\mathbf{u}_{ad}$ designed above, $\hat{\mathbf{C}}_k(\mathbf{x}_i, t_i)$'s are reset to zero matrices when the sampling of $\mathbf{x}_i$ occurs. This will lead to a discontinuity in the control signal, which may in turn excite unmodeled dynamics of the system. Here a modification is given to avoid the discontinuity.

While we still have $\hat{\mathbf{C}}_1(\mathbf{x}_i, t_i) = \mathbf{0}$ $\forall i$'s, $\hat{\mathbf{C}}_0(\mathbf{x}_i, t_i)$'s are reset to

$$\begin{aligned} \hat{\mathbf{C}}_0(\mathbf{x}_i, t_i) &= \hat{\mathbf{C}}_0(\mathbf{x}_{i-1}, t_i) \\ &\quad + \hat{\mathbf{C}}_1(\mathbf{x}_{i-1}, t_i) diag\,[\mathbf{x}_i - \mathbf{x}_{i-1}] \end{aligned} \tag{6.1}$$

with $\hat{\mathbf{C}}_0(\mathbf{x}_1, t_1) = \mathbf{0}$. By direct substitution, the continuity of $\mathbf{u}_{ad}$ at $t = t_i$ can be easily verified.

However, in this case the boundness of the quantity $\sum_{k=0}^{k=1} \mathrm{Tr}\left[\tilde{\mathbf{C}}_k^{\mathrm{T}} \tilde{\mathbf{C}}_k\right]\Big|_{(t=t_i)}$ is not guaranteed as before and the stability condition is thus no longer valid. To solve the problem, one has to know the bounds on each component of $\mathbf{C}_0(\mathbf{x})$ $\forall \mathbf{x} \in \mathcal{B}$. In other words, we have to acquire a matrix $\mathbf{C}_{0max}$ such that $|[\mathbf{C}_0(\mathbf{x})]_{\ell m}| \leq [\mathbf{C}_{0max}]_{\ell m}$, where the notation $[\cdot]_{\ell m}$ represent the ℓmth component of the associated matrix. Using the matrix $\mathbf{C}_{0max}$ $\hat{\mathbf{C}}_0(\mathbf{x}_i, t_i)$ is reset to

$$\left[\hat{\mathbf{C}}_0(\mathbf{x}_i, t_i)\right]_{\ell m} = [\mathbf{C}_{0max}]_{\ell m}\, sat\left(\frac{\left[\check{\mathbf{C}}_0(\mathbf{x}_i, t_i)\right]_{\ell m}}{[\mathbf{C}_{0max}]_{\ell m}}\right), \tag{6.2}$$

where

$$\begin{aligned} \check{\mathbf{C}}_0(\mathbf{x}_i, t_i) &= \hat{\mathbf{C}}_0(\mathbf{x}_{i-1}, t_i) \\ &\quad + \hat{\mathbf{C}}_1(\mathbf{x}_{i-1}, t_i) diag\left[\mathbf{x}_i - \mathbf{x}_{i-1}\right], \end{aligned} \tag{6.3}$$

and the function $sat(.)$ satisfies

$$\begin{aligned} sat(y) = &\quad y \qquad \text{when} |y| \leq 1 \\ = &\quad sgn(y) \quad \text{when} |y| > 1. \end{aligned} \tag{6.4}$$

Assuming $Tr\left[\mathbf{C}_{0max}^T \mathbf{C}_{0max}\right] = N_0^*$ and using the inequalities $Tr\left[\hat{\mathbf{C}}_0^T(\mathbf{x}_i, t_i)\hat{\mathbf{C}}_0(\mathbf{x}_i, t_i)\right] \leq N_0^*$ and $(Tr\left[\mathbf{AB}\right])^2 \leq Tr\left[\mathbf{A}^T\mathbf{A}\right] Tr\left[\mathbf{B}^T\mathbf{B}\right]$, we have

$$\begin{aligned} Tr\left[\tilde{\mathbf{C}}_0^T \tilde{\mathbf{C}}_0\right]\Big|_{(t=t_i)} &= Tr\left[\hat{\mathbf{C}}_0^T(\mathbf{x}_i, t_i)\hat{\mathbf{C}}_0(\mathbf{x}_i, t_i)\right] \\ -2Tr\left[\hat{\mathbf{C}}_0^T(\mathbf{x}_i, t_i)\mathbf{C}_0(\mathbf{x}_i)\right] &+ Tr\left[\mathbf{C}_0^T(\mathbf{x}_i)\mathbf{C}_0(\mathbf{x}_i)\right] \\ &\leq \left(\sqrt{N_0^*} + \sqrt{N_0}\right)^2 \end{aligned} \tag{6.5}$$

Consequently, $\sum_{k=0}^{k=1} Tr\left[\tilde{\mathbf{C}}_k^T \tilde{\mathbf{C}}_k\right]\Big|_{(t=t_i)}$ is bounded by $\left(\sqrt{N_0^*} + \sqrt{N_0}\right)^2 + N_1$ for all x_i's.

6.1.2 Use of a Hysteresis Loop

To implement the sampling and adaptation processes in the proposed controller, one needs a flag to define the status of $\|\mathbf{e}(t)\|$. This flag equals 1 when $\|\mathbf{e}(t)\| > \rho$ and equals 0 otherwise. A rising edge in the flag triggers the sampling and adaptation process, and thereafter, the controller waits for the falling edge to turn off the adaptation. Since there is always noise present in the system, either from the sensor or the numerical calculation, the controller may trigger the sampling and switch the adaptation falsely around $\|\mathbf{e}\| = \rho$.

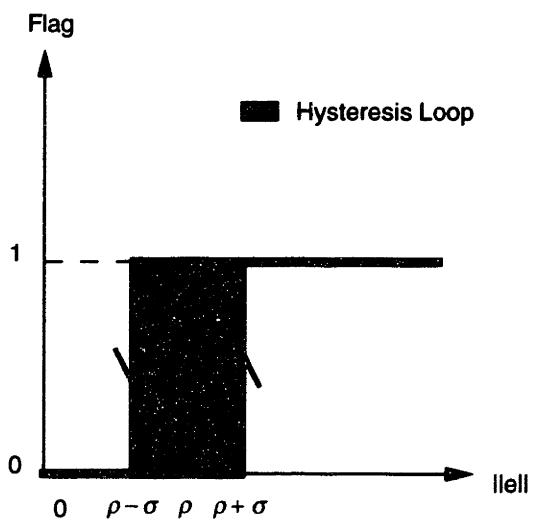

Figure 6.1: A hysteresis loop

To reduce the noise sensitivity of the controller, the use of a hysteresis loop is suggested. As shown in Figure 6.1, when the rising edge occurs, or the tracking error has a transition from $\|\mathbf{e}\| \leq \rho + \sigma$ to $\|\mathbf{e}\| > \rho + \sigma$, the sampling and adaptation are triggered. Whenever the flag resets to zero again, or the tracking error has a transition from $\|\mathbf{e}\| > \rho - \sigma$ to $\|\mathbf{e}\| \leq \rho - \sigma$, the adaptation is turned off. Obviously,

in order to justify the use of the hysteresis loop, 2σ, the thickness of the loop, needs to be at least larger than the noise intensity . This in turn means that the tracking accuracy should be at least of the same order of magnitude as the noise intensity because $\rho > \sigma$.

6.1.3 Scaling of State Variables

In the preceeding discussion, the Euclidean norm was used to compute the triggering level of the sampling and adaptation process; i.e. $\|\mathbf{e}\|^2 = e_1^2 + e_2^2 + \ldots + e_n^2$. This implicitly assumes a scaling relation among the state variables. However, similar to the weighting matrices used in optimal control problems, it is useful to employ a weighted Euclidean norm to accommodate the signal levels and the different units among the state variables.

Consider an SISO system for example. If the reference model is in the form

$$x_m^{(n)} + a_1 x_m^{(n-1)} + \ldots + a_{n-1}\dot{x}_m + a_n x_m = br \tag{6.6}$$

with n repeated poles at ω, then the position signal x_m has most of its frequency contents below ω. Heuristically, $\frac{1}{\omega}$ units of the velocity signal $\dot{x}_m$ is as significant as one unit of the position signal x_m. This suggests the use of a weighting matrix $\mathbf{W} = diag\left[1, \frac{1}{\omega}, \ldots, \frac{1}{\omega^{n-1}}\right]$ to rescale the state variables by the relation $\mathbf{x}^* = \mathbf{W}\mathbf{x}$. As a result. the norm and the eigenvalues of the associated $\mathbf{P}$ matrix are inversely proportional to ω^{n-1}. Recalling the rule $4\|\mathbf{P}\|\epsilon = \rho$, after the rescaling, it becomes

$$\omega^{n-1}\rho \approx \beta\epsilon. \tag{6.7}$$

where β is a certain constant. This is referred as the "balance condition" in [39]. Eq.(6.7), combined with the approximation $\epsilon \approx \frac{M_p}{(p+1)!}\|\mathbf{x} - \mathbf{x}_i\|^{p+1}$, produces

$$M_p\|\mathbf{x} - \mathbf{x}_i\|^{p+1} \approx (p+1)!\omega^{n-1}\rho. \tag{6.8}$$

Such a condition gives us an insight into how the localization of the estimation depends on the properties of the system function, the order of approximation, the system bandwidth, and the tracking accuracy. Basically, if the system function is quite nonlinear (large M_p), or the system bandwidth is low (small ω), or an accurate tracking is required (small ρ), the controller must constantly update its operating point $\|\mathbf{x}_i\|$ to adapt to the fast changing dynamics. Nevertheless, one can increase the order of approximation p to enlarge the " window size " $\|\mathbf{x} - \mathbf{x}_i\|$ used in estimating the uncertain, nonlinear system function.

6.2 Controller Simulations

Simulations of several examples are presented in this section to illustrate the main features of the proposed adaptive control scheme. The first example illustrates the conservatism of Theorem 5.3.1, while the second one shows the results of using different order of approximation in estimating the uncertain, nonlinear function. The effects of adjusting the adaptation gain are presented in the third example.

Example 1: Consider the following first order system

$$\dot{x} = f(x) + u \tag{6.9}$$

and the reference model

$$\dot{x}_m = -8x_m + 8sin(0.8\pi t). \tag{6.10}$$

with $x(0) = x_m(0) = 0$. In Eq.(6.9), $f(x)$ equals $sin(x)$ but will be assumed unknown to the controller. Using a first order approximation, the proposed control scheme will generate an estimate of $f(x)$ in order to cancel its effect.

According to the previous notations, $\mathbf{A}_m = -8$ and thus $\mathbf{P} = 0.0625$. To compute M_m, instead of using the expression in Theorem 5.3.1, we will take $M_m = 3$ since

$|\dot{x}_m(t)| < 3 \ \forall t \geq 0$. Furthermore, it is assumed that $f(x)$ and its derivatives are known *a priori* to be bounded by 1. This implies that $N_0^* = N_0 = N_1 = M_1 = 1$. Finally, $\rho = 0.08$ is chosen here in order to make the controller achieve such a tracking accuracy.

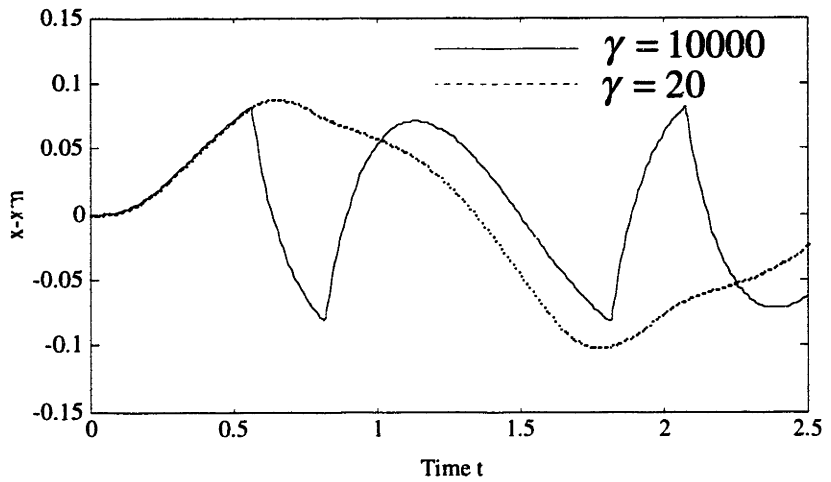

Figure 6.2: Tracking errors for $\gamma = 10000$ and $\gamma = 20$

Substituting these parameters into Eq.(5.24)[1], one obtains

$$\frac{1562.5}{\gamma} \leq \frac{1}{3}\left(0.72 - \sqrt{0.0064 + \frac{80}{\gamma}} - \delta\right). \tag{6.11}$$

This inequality can be used to solve for the adaptation gain γ. By trial and error, we get $\gamma \geq 10000$, which means that a very high adaptation gain is needed. Recalling that Eq.(5.24) is only a sufficient condition for stability, hence the resultant γ could be very conservative. Actually, depending on the system function $f(x)$, a " moderate " γ may achieve approximately the same tracking accuracy without requiring too high of a control authority. This argument is verified through simulations. Figure 6.2

[1]In all the examples, the use of the modified continuous control laws in Eqs.(6.1) and (6.2) is assumed. Therefore, one should replace the N_0+N_1 term with $\left(\sqrt{N_0^*}+\sqrt{N_0}\right)^2+N_1$ in this equation.

shows the tracking error results for $\gamma = 10000$ and $\gamma = 20$. For $\gamma = 10000$, it is seen that once x leaves $\Phi(t)$, which corresponds to the case $|x - x_m| > \rho$, the controller applies significant effort to force it to return immediately. On the other hand, when $\gamma = 20$, the controller allows x to leave $\Phi(t)$ for a while and does the adaptation in a milder way. Notice that the tracking performance for both cases are about the same. Consequently, one can simply apply a " sufficiently high " adaptation gain to ensure the stability and the tracking performance without obeying Eq.(5.24) exactly. This gives us more flexibility in designing the controller. Our current research focuses on obtaining a result leading to a less conservative γ.

Example 2: Here we still use the same system as above. However, we choose $\rho = 0.01$ and inject a white noise of intensity 0.0015 in the measurement of x. Moreover, a hysteresis loop of thickness $2\sigma = 0.004$ is employed to account for the noise effect.

Figure 6.3 shows the tracking performance corresponding to different orders of approximation in the control scheme, where $\gamma = 100$ is set for all cases. These simulation results show that we have a more accurate tracking with a higher order approximation for this particular nonlinear function. This can be futher explained by the simulations shown in Figures 6.4, 6.5 and 6.6. These results which show the uncertain function and its estimates by different controllers. It is clear that in this particular example the controller using high order approximation leads to a better function estimation.

Example 3: Now let us consider a second order plant and a reference model with the forms [38]

$$\ddot{x} = f(x, \dot{x}) + u. \tag{6.12}$$

$$\ddot{x}_m = -20\dot{x}_m - 100x_m + 100r, \tag{6.13}$$

where $f(x, \dot{x}) = -6sin(4\dot{x}) + 3e^{-2|x|} + x + \dot{x}$ and r is given by a $0.4Hz$, unity square

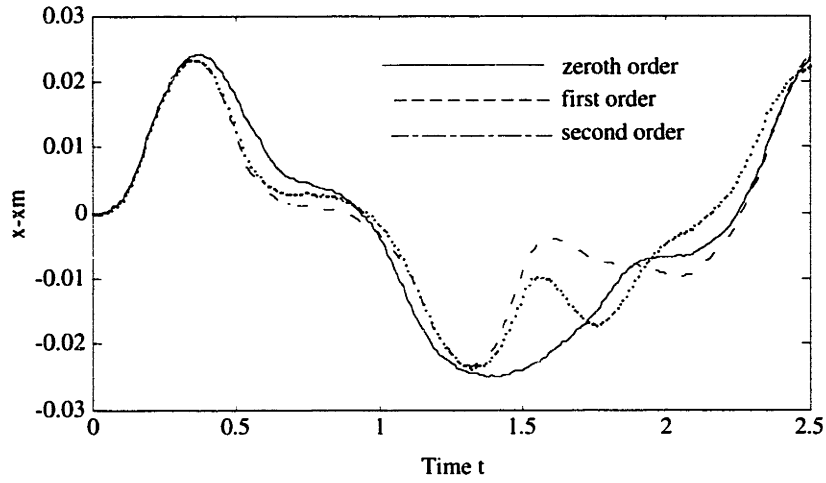

Figure 6.3: Tracking errors for different orders of approximation

wave filtered through a first order filter with a bandwidth of $10\frac{rad}{s}$.

For the purpose of accommodating the system dynamics, state variables are scaled as illustrated in Section 4. The values of the parameters ρ and σ are related as $\rho = 0.015$ and $\sigma = 0.001$. Note that the hysteresis loop is used to provide robustness against the noise resulting from numerical calculations. Figure 6.7 compares the tracking performance corresponding to different adaptation gains. The simulation results indicate that the performance improves as the adaptation gain is increased.

The function estimates using the proposed procedure are shown in Figure 6.8. It is seen that an increase in the adaptation gain results in a better estimate. We note, however, that the high frequency components of $f(x, \dot{x})$ do not appear in the function estimates. One possible explanation is that the reference model, which generates the desired trajectory, has a bandwidth of $10\frac{rad}{s}$, and consequently the adaptation scheme will be constrained to frequencies in that range.

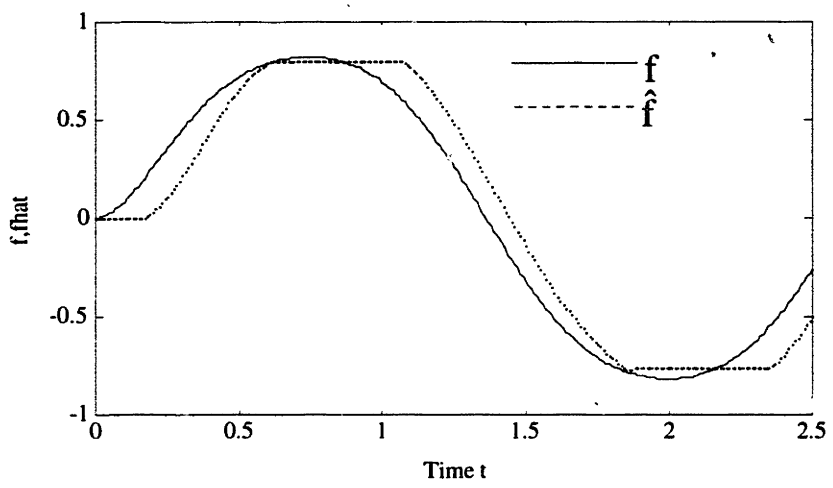

Figure 6.4: Uncertain function and its estimate for zeroth order approximation scheme

6.3 Comparisons of the Adaptive Controller with Other Control Schemes

The performance of the proposed adaptive controller using local function estimation is compared with other control schemes including a simple P controller, a sliding-mode controller and an adaptive controller. The simulation example used here is similar to the first-order system discussed in Example 1 except that the uncertain function $f(x)$ In Eq.(6.9) now equals x^2 and $x_m(0) = 0.04$, $x(0) = 0.02$. Notice that due to the square nonlinearity and nonzero initial condition, the solution for the open-loop system is

$$x(t) = \frac{x(0)}{1 - tx(0)}, \tag{6.14}$$

thus the state trajectory has a finite escape time equal to $\frac{1}{x(0)}$.

Adaptive control using local function estimation:

Again we still choose $\rho = 0.08$. Because $|x_m(t)| \leq 1 \ \forall t \geq 0$. $|x(t)| \leq |x_m(t)| + \rho =$

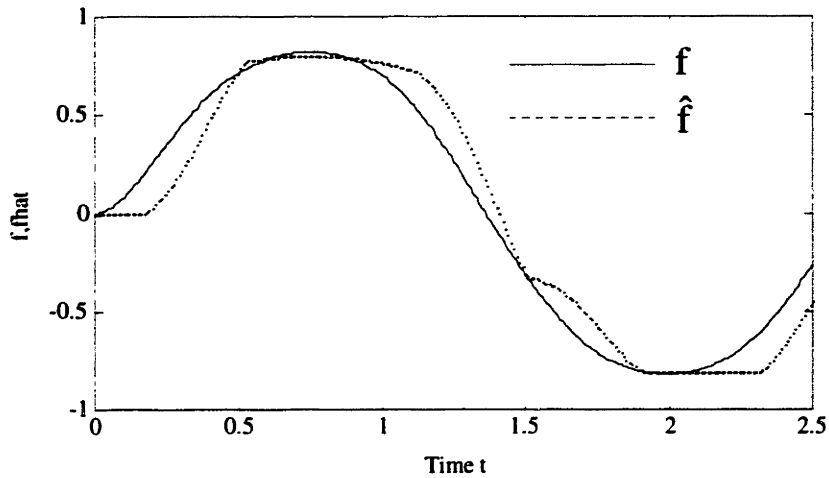

Figure 6.5: Uncertain function and its estimate for first order approximation scheme

1.08 if $x(t) \in \bar{\mathcal{B}}$. This implies $|f(x)| \leq 1.08$ and $|f'(x)| \leq 2.16$ for $x \in \bar{\mathcal{B}}$. In other words, we can select $N_0^* = N_0 = 1.08$ and $N_1 = 2.16$. Further, if the first order Taylor's expansion is used to approximate f, then $M_1 = 2$ due to the fact that $f''(x) = 2\ \forall x$.

Similar to Example 1, one can substitute the related parameters into Eq.(5.24), one obtains

$$\frac{2133}{\gamma} \leq \frac{1}{3}\left(0.4857 - \sqrt{0.0064 + \frac{109.21}{\gamma}} - \delta\right). \tag{6.15}$$

By trial and error, we get $\gamma \geq 20000$, which also means that a very high adaptation gain is needed.

Figure 6.9 shows the tracking error results for $\gamma = 20000$ and $\gamma = 200$. For $\gamma = 20000$, once x leaves $\Phi(t)$, which corresponds to the case $|x - x_m| > \rho$, the controller applies significant effort to force it to return immediately. On the other hand, when $\gamma = 200$, the controller allows x to leave $\Phi(t)$ for a while and does the adaptation in a milder way. Notice that the tracking performance for both cases are

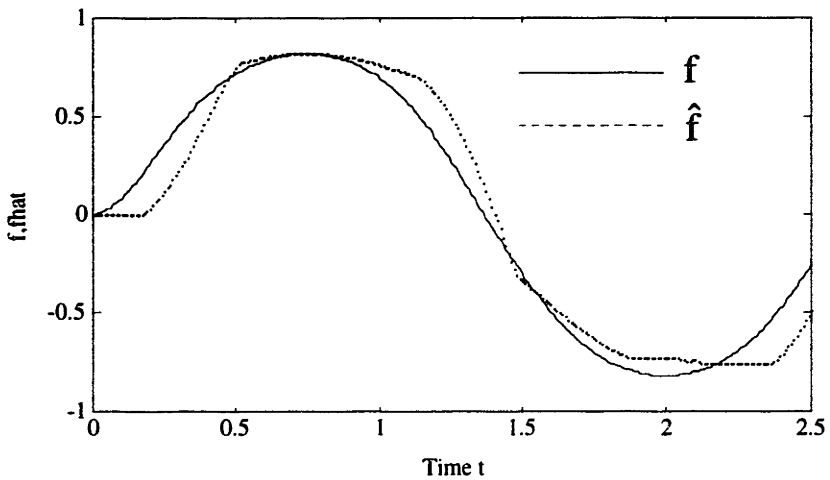

Figure 6.6: Uncertain function and its estimate for second order approximation scheme

about the same and the tracking errors are dictated by the parameter ρ.

P control:

Figure 6.10 shows the tracking error when a simple P control $u = -8x$ is applied to the plant. It is obvious that the resultant system presents larger tracking error compared to Figure 6.9.

Sliding-mode controller:

Now we assume that the dynamics of $f(x)$ is not exactly known but is bounded by a known function $2x^2$, in other words,

$$|f(x)| \leq 2x^2. \tag{6.16}$$

In order to have the plant track $x(t) \equiv x_m(t)$, we define a sliding surface $\epsilon = 0$. We then have:

$$\dot{e} = \dot{x} - \dot{x}_m = f(x) + u + 8x_m - 8sin(0.8\pi t). \tag{6.17}$$

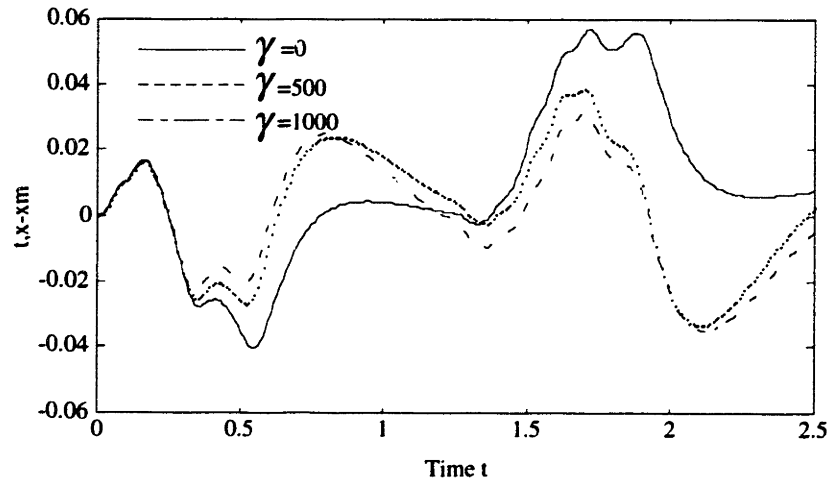

Figure 6.7: Tracking errors for $\gamma = 0$, $\gamma = 500$ and $\gamma = 1000$

According to [39], the sliding-mode controller can be selected as:

$$u = -8x_m + 8sin(0.8\pi t) - k(x)sat(\frac{\epsilon}{\rho}), \tag{6.18}$$

in which k(x) is a control gain to be determined, $\rho = 0.08$ is the boundary layer thickness [2] and $sat(.)$ is the saturation funtion defined in Eq. (6.4).

By choosing $k(x)$ to be large enough, we can guarantee the stability of the system. Indeed, we have from Eq. (6.17) and Eq. (6.18) that

$$\frac{1}{2}\frac{d}{dt}\epsilon^2 = \dot{\epsilon}\epsilon = f(x)\epsilon - k(x)sat(\frac{\epsilon}{\rho}). \tag{6.19}$$

Therefore, letting

$$k(x) = 2x^2 + 8. \tag{6.20}$$

from Eq. (6.19) we have

$$\frac{1}{2}\frac{d}{dt}\epsilon^2 \leq -8|\epsilon| \quad \text{for } |\epsilon| > \rho \tag{6.21}$$

[2]The boundary layer here is similar to the set $\mathcal{B}$ discussed in Lemma 5.3.1.

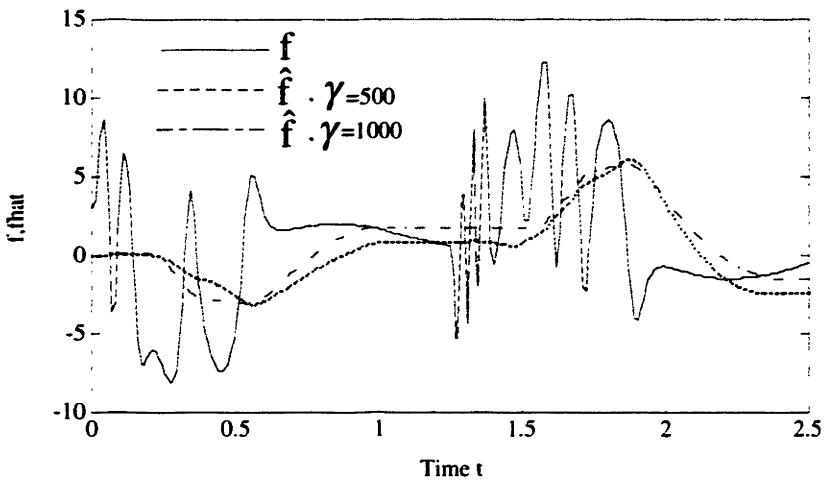

Figure 6.8: Uncertain function and its estimates for $\gamma = 500$ and $\gamma = 1000$

which guarantees that the boundary layer is attractive, hence invariant: all trajectories starting inside $\mathcal{B}(t = 0)$ remain inside $\mathcal{B}(t)$ for all $t \geq 0$. Such a fact can also be demonstrated by the simulations in Figure 6.11. in which the time response of the tracking error ϵ is plotted. Although the state trajectory stays inside the boundary layer all the time and more accurate tracking is achieved in this case. the selection of $k(x)$ requires the knowledge of the bound of $f(x)$. If such information is not available. a stabilizing sliding-mode controller can not be designed.

Conventional adaptive controller:

In this approach. it is assumed that the structure of the square nonlinearity in $f(x)$ is known but the parametric uncertainty exists. namely. it is known a priori that $f(x) = cx^2$ but the coefficient $c = 1$ is unknown.

The error dynamics in Eq. (6.17) motives us to choose the following control law:

$$u = -8x_m + 8sin(0.8\pi t) - 8\epsilon - \hat{f}(x) = -8x_m + 8sin(0.8\pi t) - 8\epsilon - \hat{c}x^2 \quad (6.22)$$

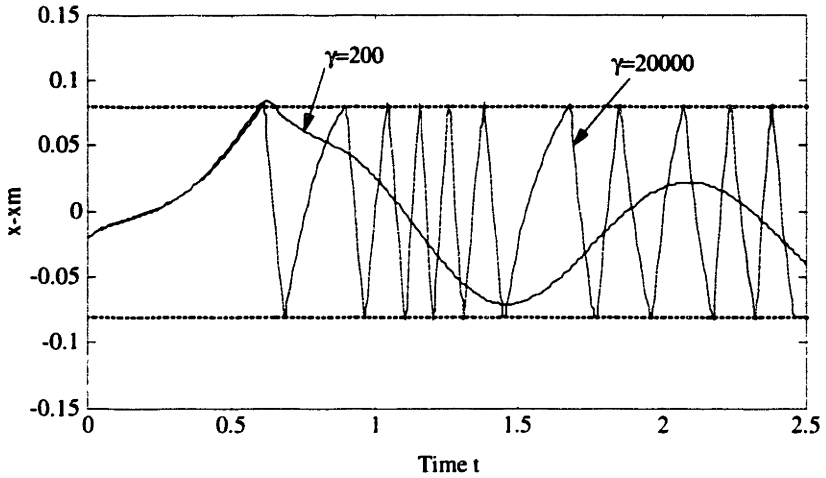

Figure 6.9: Tracking errors for the adaptive control using local function estimation

where $\hat{c}$ is the estimate of c. Substituting Eq. (6.22) into the error dynamics, we get

$$\dot{e} = -8e + \tilde{c}x^2 \tag{6.23}$$

where $\tilde{c} = 1 - \hat{c}$ is the estimation error.

To derive a stable adaptation law, we define a Lyapunov function $\mathcal{V} = \frac{1}{2}e^2 + \frac{1}{2}\tilde{c}^2$. Then the time derivative of $\mathcal{V}$ along the state trajectory can be calculated as

$$\begin{aligned} \dot{\mathcal{V}} &= e\dot{e} + \tilde{c}\dot{\tilde{c}} \\ &= -8e^2 + e\tilde{c}x^2 + \tilde{c}\dot{\tilde{c}} \end{aligned} \tag{6.24}$$

Consequently, if the adaptation law

$$\dot{\hat{c}} = ex^2 \tag{6.25}$$

is chosen, we have $\dot{\mathcal{V}} = -8e^2$. Thus the stability of the control system is guaranteed.

Simulations of this adaptive control system is shown in Figure 6.12. The tracking performance is very similar to the P controller discussed previously.

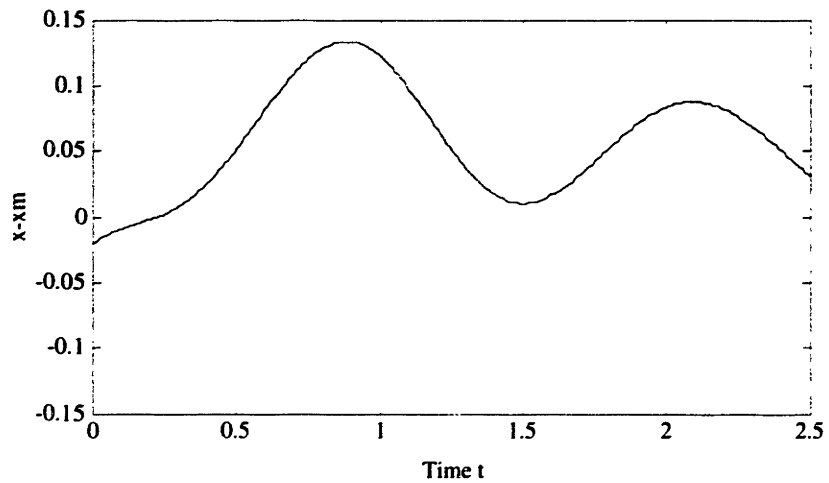

Figure 6.10: Tracking error for the P controller: $\gamma = 0$

6.4 Summary and Remarks

Practical implementation issues and simulation examples are presented in this chapter. Particularly, the performance of the proposed adaptive control scheme is compared with other control schemes. Although the sliding-mode control can achive high tracking performance, prior information on the bounds of the nonlinearity and the uncertainty is needed. On the other hand, the convention adaptive controller, which is mainly used to tackle systems with parametric uncertainty, heavily relies on the knowledge about the structure of the unknown system function. As will be shown later, the system functions for magnetically levitated rotating machines are both nonlinear and uncertain. The bounds for the system functions are usually unknown and it is difficult to express the system uncertainties in parametric forms. The only knowledge available is the smoothness of the system functions. As a result, it may be more appropriate to use the proposed adaptive control scheme to locally estimate

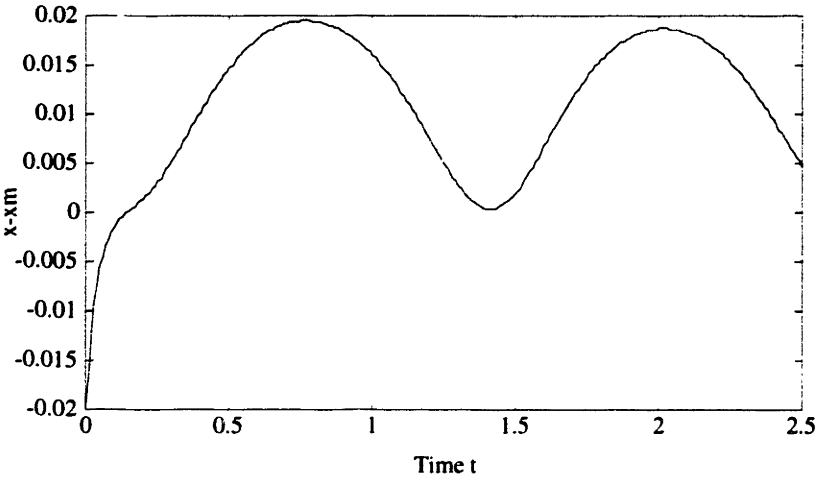

Figure 6.11: Tracking error for the sliding-mode controller

and cancel the system functions. This is the subject of the next chapter.

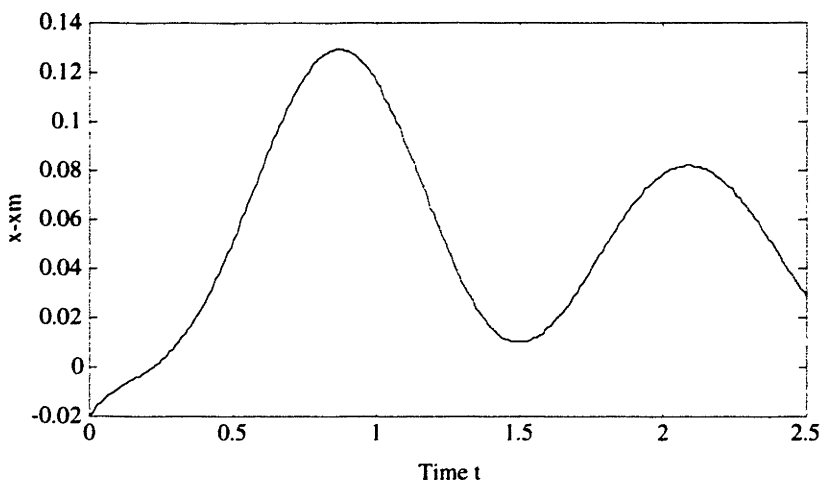

Figure 6.12: Tracking error for the conventional adaptive controller

Chapter 7

Adaptive Control of a Magnetically Levitated Turbo Pump

The successful operation of magnetically levitated rotating machines requires five-axis control simultaneously. If the rotor stands upright, which is the case for the turbo pump under consideration, the control of the thrust bearing is decoupled from the control of the radial bearing system. For the thrust bearing control, the controller has to counteract the gravity and cancel the system nonlinearities. On the other hand, the controller for the radial bearing system not only faces the nonlinearities, but it also has to deal with the MIMO nature of the system and provide consistent performance under the changing dynamics.

The adaptive control scheme proposed previously uses the local function estimation to cancel the nonlinear and uncertain dynamics present in the system and introduce some desired dynamics. With a proper designed sampling rule, the neighborhood of approximation can be moved from time to time in order to capture the fast changing system dynamics. Therefore, this scheme naturally lends itself to a promising approach for controlling the magnetically levitated rotating machines.

In this chapter, the implementation of the adaptive control scheme for the existing turbo pump is described. Numerical simulations as well as experimental results are used to evaluate the controller performance in comparison with the analog compensator.

7.1 Controller Design for the Magnetic Bearings

Now, we will use the thrust bearing to illustrate the controller structure. When the eddy current loss is ignored, the nonlinear equation of motion for the thrust bearing can be written as:

$$\dot{\mathbf{z}}(t) = \begin{bmatrix} 0 & 1 \\ 0 & 0 \end{bmatrix} \mathbf{z} + \begin{bmatrix} 0 \\ \frac{F_z(u_z, z)}{m} \end{bmatrix} - \begin{bmatrix} 0 \\ g \end{bmatrix}, \tag{7.1}$$

where the state vector $\mathbf{z} = [z \ \dot{z}]^T$, and $F_z(u_z, z)$ is obtained by subsitituting the transformation in Eq.(4.1) into Eq.(2.10). This adaptive controller is applicable if one technically assumes that the nonlinear function F can be approximated in the following manner,

$$F_z(u_z, z) \approx f_{z_i}(z - z_i) + b_z u_z, \quad \text{as } z \to z_i, \tag{7.2}$$

in which $f_{z_i}(\cdot)$ is a polynomial with its coefficeints depending on z_i, and b_z is a known constant. This assumption requires some justification.

Practically, the rotor displacements are constrainted by the existence of touchdown bearings and the maximum control currents should be limited to avoid damaging the power amplifier. For the thrust bearing, we consider the following operating region:

$$\begin{aligned} |z| &\leq z_{touchdown} \\ |u_z| &\leq i_{max}, \end{aligned} \tag{7.3}$$

in which $z_{touchdown} = 200\mu m$ and $i_{max} = 3Amps$. Figure 7.1 shows the 3-D surface plot of $F_z(u_z, z)$ as a function of z and u_z. It is clear that F is quite smooth in the operating region. If the region is further divided into several regions as Figure 7.2, for each region, one can use a function of the form $a_0 + a_1 z + b u_z$ to fit $F_z(z, u_z)$ in the least square sense. Notice that in subregions III, Figure 7.2 shows that the

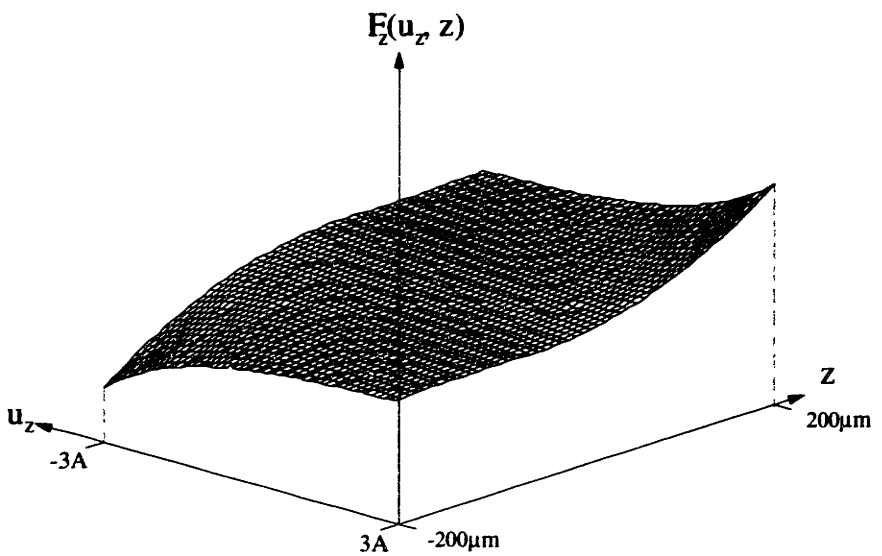

Figure 7.1: 3-D surface plot of the magnetic force

thrust bearing exerts a large force in the same direction as z. These regions are not considered because such cases should not happen when the controller is well-designed.

Table A in Figure 7.2 lists the fitting results when the nonlinear input transformation in Eq.(4.1) is applied, while the results for the bias current strategy[1] are listed in Table B. Obviously, in the nonlinear input transformation case, the parameter b does not vary much in different regions compared to what occurs in the bias current strategy. Thus it is reasonable to assume F_z can be approximated as

$$F_z(u_z, z) \approx f(z) + b_z u_z. \tag{7.4}$$

In this approximatin, we may use the average of b values in the least square fitting

[1]In this case, the relations $i_u = i_0 + 0.5u_z$; $i_\ell = i_0 - 0.5u_z$ are employed regardless of the magnitude of u_z.

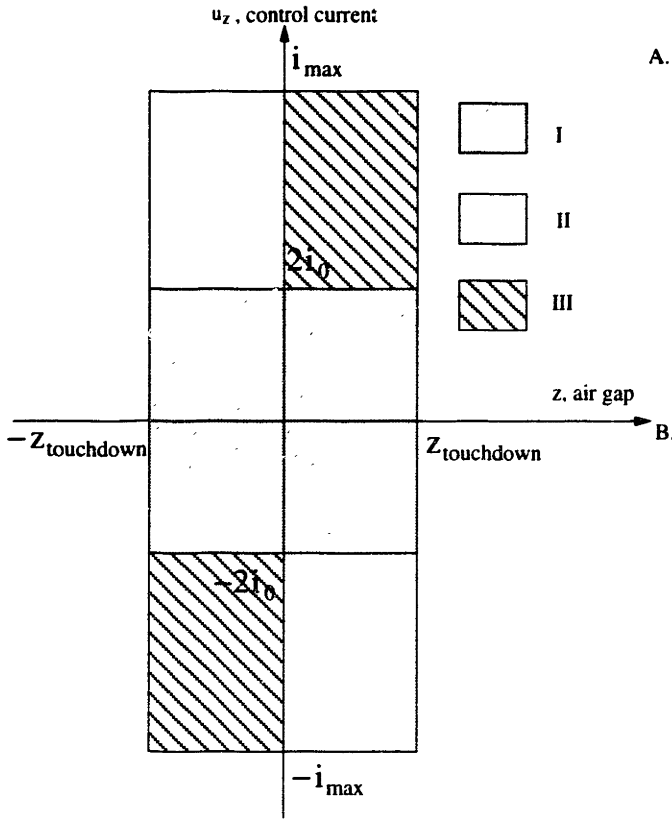

A. Fitting results with the nonlinear input transformation

	I	II
a_0	0 N	0.56N
a_1	2.92e+4N/m	5.16e+4N/m
b	11.2N/A	10.4 N/A
maximum error	7.50 N	6.38N

B. Fitting results with the bias current strategy only

	I	II
a_0	0 N	13.2N
a_1	2.92e+4N/m	7.58e+4N/m
b	11.2 N/A	2.74N/A
maximum error	7.50 N	10.6 N

1. $F(z,u_z) = a_0 + a_1 z + bu_z$ is assumed in the fitting.
2. In subregions III, the bearing applies a large force in the same direction as z. These regions are not considered here because such cases should not happen when the controller is well-designed.

Figure 7.2: Least square fitting of the magnetic force function

for the constant b_z. Moreover, the function $f(z)$ should be smooth and has bounded second derivative due to the smoothness of $F_z(u_z, z)$.

The function $f(z)$ certainly satisfies the approximation condition discussed in section 5.2, so the adaptive controller can be used to on-line estimate and cancel $f_{z_i}(z - z_i)$, the local first order Taylor's expansion of f, and force $\mathbf{z}(t)$ to follow the reference trajectory $\mathbf{z}_m(t)$. The trajectory $\mathbf{z}_m(t)$ is generated by a second order

reference model of the following form:

$$\dot{\mathbf{z}}_m = \mathbf{A}_m \mathbf{z}_m + \mathbf{B}_m r, \tag{7.5}$$

in which $\mathbf{A}_m = \begin{bmatrix} 0 & 1 \\ -\omega_n^2 & -2\zeta\omega_n \end{bmatrix}$, and $\mathbf{B}_m = \begin{bmatrix} 0 \\ \omega_n^2 \end{bmatrix}$. The parameters ζ and ω_n are the damping ratio and the natural frequency of the second order reference model respectively. Moreover, $r \equiv 0$ is assumed because regulator problems are of interest.

Similar to Eq.(5.8), the control law is chosen as:

$$u_z = \frac{1}{b_z}(\mathbf{K}\mathbf{z} + u_{ad}), \tag{7.6}$$

where $\mathbf{K}\mathbf{z}$ is a full-state feedback component with $\mathbf{K} = [-\omega_n^2 \ -2\zeta\omega_n]$, and u_{ad} is an adaptive compensating control signal used to to estimate and cancel $f_{z_i}(z - z_i)$.

The basic concept of designing u_{ad} is the following: First, we define an two dimensional " moving sphere " $\Phi(t)$ centered at $\mathbf{z}_m(t)$; i.e., $\Phi(t) = \{\mathbf{y} \in \mathcal{R}^2 | \ \|\mathbf{y} - \mathbf{z}_m(t)\| \leq \rho\}$, where $\rho > 0$ is the radius of the sphere (see Figure 5.2). Assume that initially $\|\mathbf{z}(0) - \mathbf{z}_m(0)\| \leq \rho$, so $\mathbf{z}(0)$ is in $\Phi(0)$. While the full-state feedback term is always used as part of u_z, the adaptation term u_{ad} is initially set to zero. If the evolution of $\mathbf{z}$ is such that at $t = t_1$ it first " penetrates " the surface of the moving sphere $\Phi(t_1)$, or $\|\mathbf{z}(t_1) - \mathbf{z}_m(t_1)\| = \rho$, we sample $\mathbf{z}(t_1)$ as $\mathbf{z}_1$. The controller turns on the adaptation term u_{ad} immediately to estimate and cancel $f_{z_1}(z - z_1)$.

Because $f_{z_1}(z, z_1)$ is expressed as

$$f_{z_1}(z - z_1) = a_0 + a_1(z - z_1). \tag{7.7}$$

where $a_0 = f|_{z=z_1}$ and $a_1 = \frac{\partial f}{\partial z}|_{z=z_1}$, then u_{ad} is given by:

$$u_{ad} = -\hat{a}_0 - \hat{a}_1(z - z_i), \tag{7.8}$$

with

$$\dot{\hat{a}}_0 = \quad \gamma \mathbf{e}^T \mathbf{P} \begin{bmatrix} 0 \\ 1 \end{bmatrix} \quad \text{when} \|\mathbf{e}\| \geq \rho$$

$$
\begin{aligned}
&= && 0 && \text{otherwise} \\
\dot{\hat{a}}_1 &= && \gamma(z - z_1)\mathbf{e}^T\mathbf{P}\begin{bmatrix} 0 \\ 1 \end{bmatrix} && \text{when} \|\mathbf{e}\| \geq \rho \\
&= && 0 && \text{otherwise.}
\end{aligned} \tag{7.9}
$$

In this adaptive control law, $\mathbf{e} = \mathbf{z} - \mathbf{z}_m$ is the error state vector, $\hat{a}_0$ and $\hat{a}_1$ are the estimates of a_0 and a_1, γ is the adaptation gain and $\mathbf{P}$ is the matrix satisfying $\mathbf{A}_m^T\mathbf{P} + \mathbf{P}\mathbf{A}_m = -\mathbf{I}$.

If $f(z)$ is estimated and canceled properly, $\mathbf{z}$ will be forced to return into $\Phi(t)$ before it goes too far away from $\mathbf{z}_1$. Then, the controller turns off the adaptation and waits for the next time $\mathbf{z}$ leaves $\Phi(t)$. The same sampling and adaptation processes repeat for $\mathbf{z}_2, \mathbf{z}_3, \ldots, \mathbf{z}_i$ and so on.

The controller structure shown in Eqs. (7.6), (7.8) and (7.9) still lacks of practicability. Modifications discussed in chapter 6 have to be made in the control law to avoid exciting the unmodeled dynamics, to reduce the noise sensitivity and to accommodate the various signal levels in system response.

Control of the radial bearing system is slightly different from that of the thrust bearing due to the coupling effects among the radial axes. While the rotor geometry always makes x_1 and x_2 (y_1 and y_2) axes coupled, the additional gyroscopic effects resulted from spinning causes the X axes dynamics to be influenced by the Y axes velocities and vice versa. In addition, the gyroscopic coupling forces also appear as part of system dynamics. In fact, denoting $\mathbf{x} = [x_1, x_2, y_1, y_2]^T$ and $\mathbf{u} = [u_{x1}, u_{x2}, u_{y1}, u_{y2}]^T$, the system dynamics can be expressed in the following form:

$$
\dot{\mathbf{x}} = \mathbf{A}\mathbf{x} + \mathbf{K}(\Omega)\mathbf{x} + \mathbf{F}(\mathbf{x}, \mathbf{u}). \tag{7.10}
$$

in which the vectorial function $\mathbf{K}(\cdot)$ represents the gyroscopic effect due to the rotor speed Ω, and $\mathbf{F}(\mathbf{x}, \mathbf{u})$ represents the magnetic force vector contributed by the radial bearings.

Similar to the previous arguments used in the axial bearing case. the vectorial force function $\mathbf{F}(\mathbf{x}, \mathbf{u})$ can be approximated as

$$\mathbf{F}(\mathbf{x}.\mathbf{u}) \approx \mathbf{f}_o(\mathbf{x}) + \mathbf{B}\mathbf{u}. \tag{7.11}$$

Combining Eqs.(7.10) and (7.11). the radial bearing dynamics is

$$\begin{aligned} \dot{\mathbf{x}} &= \mathbf{A}\mathbf{x} + \mathbf{K}(\Omega)\mathbf{x} + \mathbf{f}_o(\mathbf{x}) + \mathbf{B}\mathbf{u} \\ &= \mathbf{A}\mathbf{x} + \mathbf{f}(\mathbf{x}) + \mathbf{B}\mathbf{u} \end{aligned} \tag{7.12}$$

where the function $\mathbf{f}(\mathbf{x}) = \mathbf{K}(\Omega)\mathbf{x} + \mathbf{f}_o(\mathbf{x})$ explains the the actuator nonlinearities as well as the uncertain dynamics due to the gyroscopic effects. Eq.(7.12) is the same as the plant equation described in Eq.(5.1). Therefore, the MIMO version of the proposed adaptive controller is applicable to cancel the nonlinearities and uncertainties.

7.2 Controller System Implementation

The adaptive controller was implemented digitally using a high speed digital signal processor (DSP) board. This controller is intended to replace the analog compensator described previously. The sampling frequency for all the five axis is chosen to be $15KHz$. The position signals from the inductive sensors are filtered by second order Butterworth antialiasing filters with cut-off frequency of $3KHz$. Then the output signals are sent to analog to digital converters (A/D converters) which are linked to the DSP board. The control voltages are calculated by the DSP board and are send out through the digital to analog converters (D/A converters). The D/A converters contain low pass filters with $15KHz$ cut-off freqency. Moreover, because the rotor has major bending modes at $875Hz$ and $2.2KHz$. the control voltages are further filtered by two sets of notch filters to avoid exciting the unmodeled dynamics in the

bending mode frequency regions. Details on the DSP control software and the notch filters are provided below.

7.2.1 DSP Control Software

A high speed DSP board (ADSP-21000)[2, 3] interfaced with a PC is used for digital implementation of the controller. The control programs are written in assembly language. The program for the thrust bearing , "axialctr.asm", and the program for the radial bearings, "radctr.asm", are given in Appendix F. Figure 7.3 shows the steps to compile and run the programs. First, a reset program is used to reset the DSP chip. Then a batch file "asm" evokes the assembler, the linker and the PROM splitter to complile the program, to generate executable files and to generates PROM programer files in byte-stacked format. Then one can use the program "dumpdsp.exe" to download the byte-stacked format files (files with extension ".stk") into the DSP program memory. To run the control codes, "startdsp" is executed and thus a starting stroke is sent to the processor. Finally, the program "stopdsp" stops the program. The readers can refer to [48] on details about the PC interfacing and the DSP software development.

7.2.2 Notch Filters

The implementation of notch filters is achieved by using *MAX275* chips, the continuous-time active filters made by *MAXIM* company[29]. First, bandpass filters of the form

$$G(s) = \frac{Ks(\frac{\omega_0}{Q})}{s^2 + s(\frac{\omega_0}{Q}) + \omega_0^2} \tag{7.13}$$

are realized using the circuit diagram in Figure 7.4. In this diagram, INA(INB) is the input, BPOA(BPOB) is the output. The DC gain K, the bandpass frequency ω_0, and the bandpass width Q depends on the selection of R1, R2, R3, R4[29]. Notice

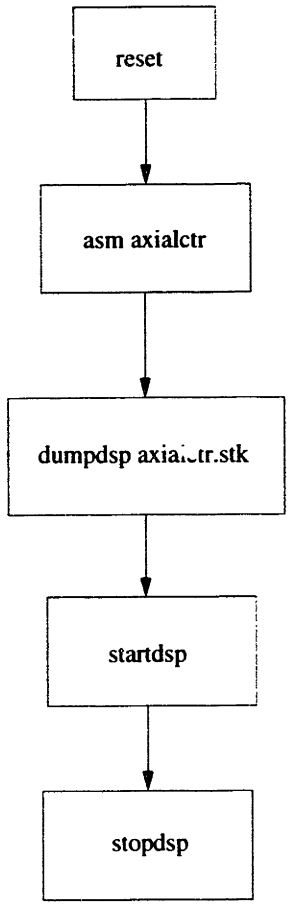

Figure 7.3: The block diagram for the DSP control software

that because the *MAX275* comprises two $2nd$-order sections, two bandpass filters (INA-BPOA and INB-BPOB) can be realized on one chip.

If we choose the DC gain K to be 1 and subtract the input from the output of the bandpass filter, then the overall transfer function becomes

$$G(s) = \frac{s^2 + \omega_0^2}{s^2 + s(\frac{\omega_0}{Q}) + \omega_0^2}, \tag{7.14}$$

which is a notch filter with notch frequency ω_0 and notch width ω_0. Notice that the substraction just mentioned can be implemented using simple operational amplifer

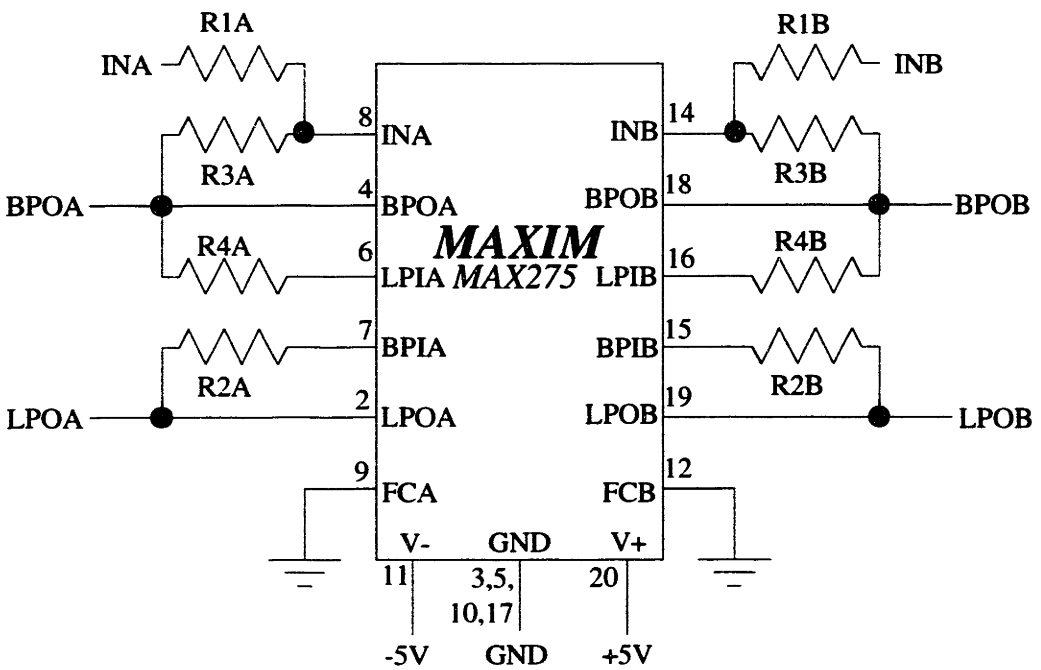

Figure 7.4: *MAX275* circuit diagram for bandpass filters

circuits shown in Figure 7.5. To effectively eliminate the structural resonance, the resistor values for the notch filters are selected as:

	first mode notch filter	second mode notch filter
R1	$1649k\Omega$	$1383k\Omega$
R2	$2M\Omega$	$1M\Omega$
R3	$1649k\Omega$	$1383k\Omega$
R4	2100Ω	$750k\Omega$

Table 7.1: Resistor values for notch filters

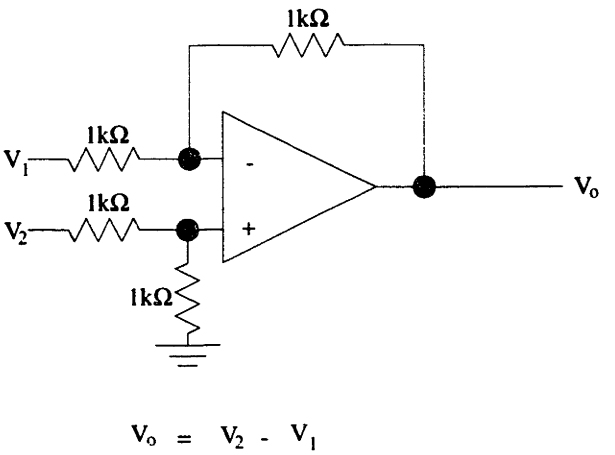

Figure 7.5: Basic difference amplifier circuit

Thus the first mode notch filters have the following form:

$$G_{notch1} = \frac{s^2 + 3.7452 \times 10^7}{s^2 + 1.5261 \times 10^3 s + 3.7452 \times 10^7}. \tag{7.15}$$

The magnitude and phase plots of this transfer function are shown in Figure 7.6. The second mode notch filters have the following form:

$$G_{notch1} = \frac{s^2 + 2.0884 \times 10^8}{s^2 + 1.8064 \times 10^3 s + 2.0884 \times 10^8}. \tag{7.16}$$

The magnitude and phase plots of this transfer function are shown in Figure 7.7.

7.3 Controller System Evaluation

In the ensuing discussion, we will present simulations of time responses using the refined nonlinear model along with the experimental results. Besides, robustness of the control system against disturbances will also be experimentally evaluated.

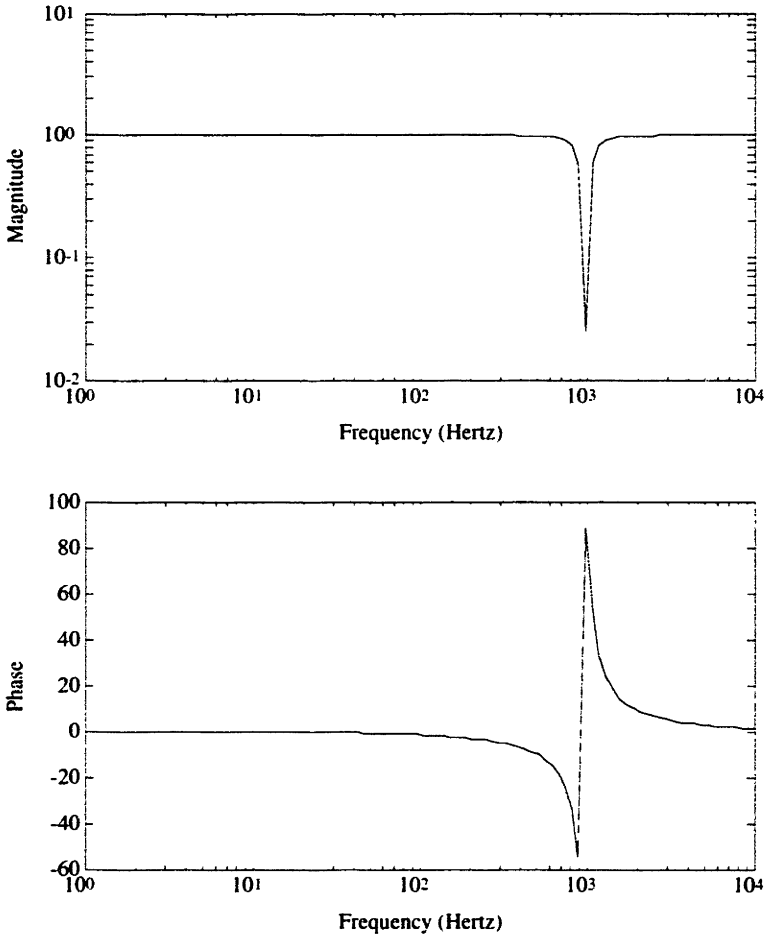

Figure 7.6: Bode plots for the first mode notch filter

7.3.1 Time responses

I. Thrust bearing:

Assuming that the controller is uncertain about the nonlinearity in the actuator forces, the goal is to levitate the rotor from the touchdown bearing to the nominal gap position. The control algorithm used the first order Taylor's expansion to estimate the system function. $\omega_n = 600\frac{rad}{s}$ and $\zeta = 1$ were chosen for the reference model. The velocities of the rotor was obtained by taking the backward difference on the

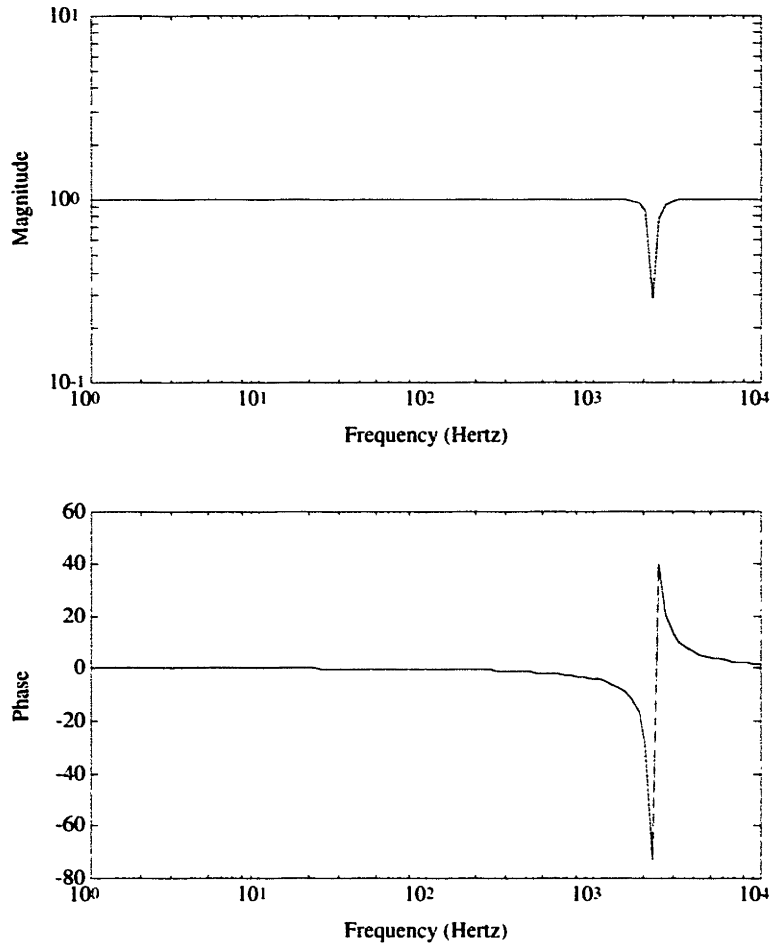

Figure 7.7: Bode plots for the second mode notch filter

position signals. Based on the results in the appendix, $b_z = 11.5\frac{N}{V}$ was adopted. Furthermore , $\rho = 1\mu m$ and a hysteresis loop of $0.5\mu m$ were used, and an adaptation gain $\gamma = 1 \times 10^{13}$ for the normalized state vectors was applied. A constant control voltage equivalent to $1.3A$ was used together with the full-state feedback and the adaptation signal in order to counteract the gravity.

Figure 7.8 shows the time responses of the thrust bearing system under closed-loop control. It is clear that the controller can adapt the uncertain system dynamics and

levitate the rotor quickly. The simulated position response is able to approximately portrait the experimental response particularly on the lag behind the reference trajectory and the settling time. However, the simulated control voltage is more oscillatory than the experimental one. One possible explanation for this is that the analog circuit used to implement Eq.(4.1) can not truely reproduce such ideal behavior.

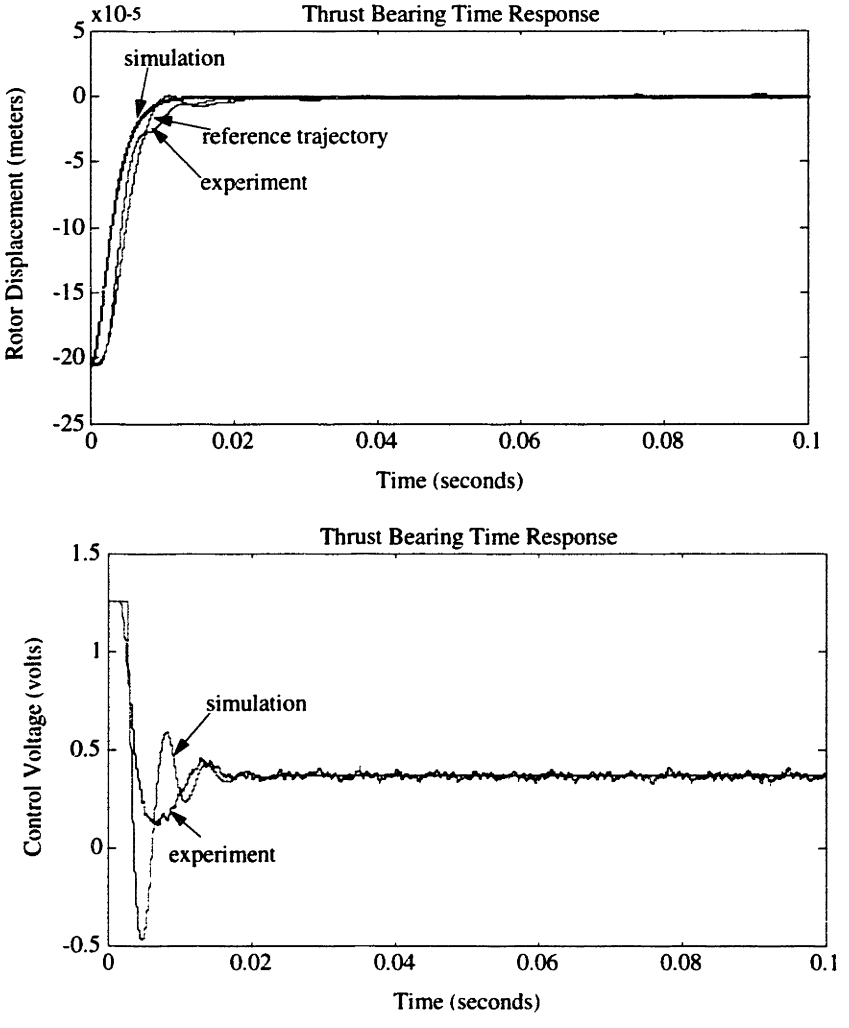

Figure 7.8: Time responses of the thrust bearing system

II. Radial Bearings

Table 7.3.1 lists the control parameters for the radial bearings. In the control algorithm, the zeroth order Taylor's expansion was used to estimate and cancel the nonlinearites in the actuator force functions and the uncertainties resulting from the gyroscopic effects. In addition, $\rho = 0.5\mu m$ and a hysteresis loop of $0.25\mu m$ were chosen in order to mimimize the noise effect. Because of the coupling nature among the radial axes, the radial bearings can be treated as either two $4th$ order system when the rotor is at rest, or an $8th$ order system as the rotor spins. Consequently, the sphere $\Phi(t)$ has higher dimensions than the thrust bearing case.

x_1, y_1 bearings	x_2, y_2 bearings
$\omega_n = 550\frac{rad}{s}$	$\omega_n = 770\frac{rad}{s}$
$\zeta = 1$	$\zeta = 1$
$\gamma = 7.0 \times 10^{13}$	$\gamma = 1.4 \times 10^{13}$
$b_{x1} = 9.64\frac{N}{A}$	$b_{x2} = 14.97\frac{N}{A}$
$b_{y1} = 11.99\frac{N}{A}$	$b_{y2} = 16.72\frac{N}{A}$

Table 7.2: Control parameters for radial bearings

The simulated and experimental time responses are shown in Figures 7.9 and 7.10. It is clear that the rotor tracks the reference trajectories very closely without using too much control authority. The simulated models are able to qualitively predict the experimental behavior except the oscillations occur initially in both position and control voltage responses. Such discrepencies are possibly due to the low frequency periodical noise observed in the position measurements. According to Figure 7.11, in which the spectrum of the position signal is plotted, major components of the sensor noise appear at $180Hz$, $360Hz$ and so on.

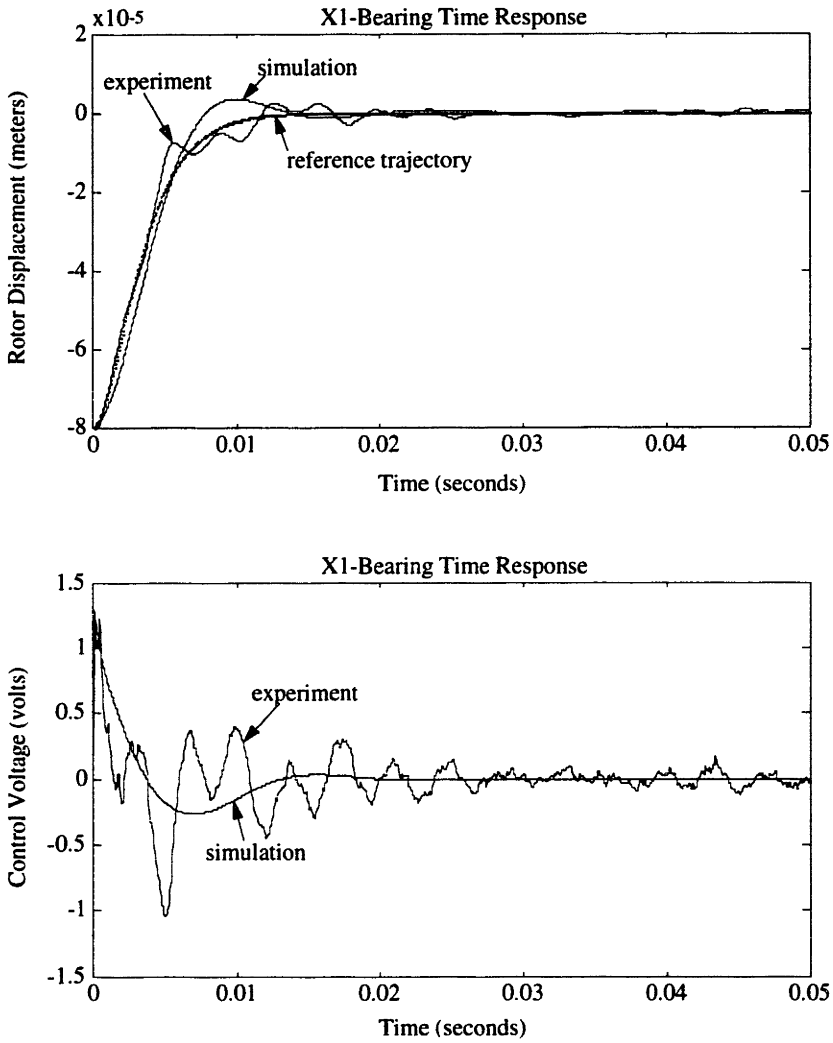

Figure 7.9: Time responses of the x_1 radial bearing

7.3.2 Disturbance Rejection

In the rotating machine applications, the presence of disturbances is inevitable. The disturbances may come from, for example, the machining forces in machine-tool spindles, and the air dynamic forces and the rotor unbalance in turbo machinery. Thus it is crucial to assure that the bearings have good disturbance rejection capability.

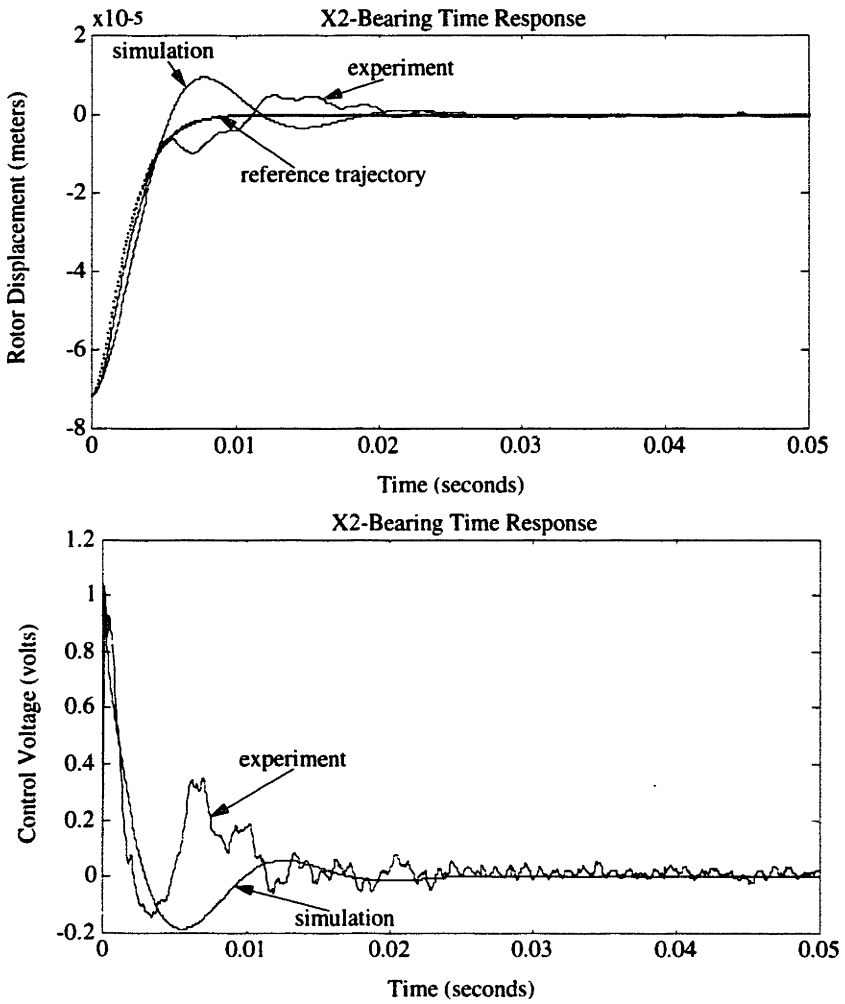

Figure 7.10: Time responses of the x_2 radial bearing

Since the derivations of the adaptive controller in the previous two chapters did not include the disturbances, it is also important to examine the robustness of the controller against external disturbances. Therefore, the disturbance rejection, in term of the bearing compliance, has been experimentally evaluated. The tests also used the same experimental setup as Figure 4.3. However, in the tests the experimental

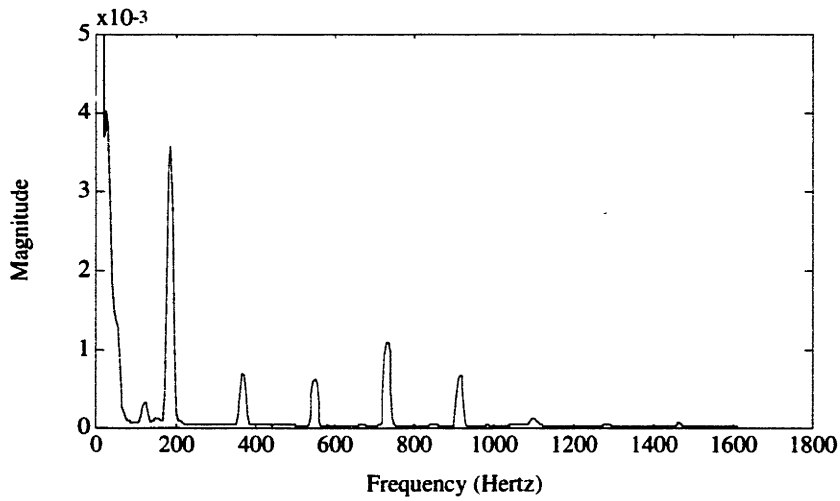

Figure 7.11: Noise spectrum of the position signal

transfer function between the output position and the input disturbance, which is equivalent to the bearing compliance, is desired.

Figure 7.12 shows the disturbance rejection responses of the thrust bearing for the analog and adaptive controllers. The maximum compliances of $3\frac{\mu m}{N}$ and $20\frac{\mu m}{N}$ were observed for the adaptive controller and the analog controller respectively. Particularly, the adaptive control system is about 20 times stiffer than the analog one for $\omega \leq 2Hz$.

The disturbance rejection responses of the x_1, x_2 radial bearings for two types of controllers are shown in Figures 7.13, 7.14. The tests were conducted when the rotor was at rest and while it was spinning at speeds of $15,000RPM$ and $30,000RPM$. The adaptive controller has lower maximum compliance than that of the analog controller, and the bearings are generally much more stiffer at low frequencies. In addition, at frequencies up to $150Hz$, the disturbance rejection properties are almost the same

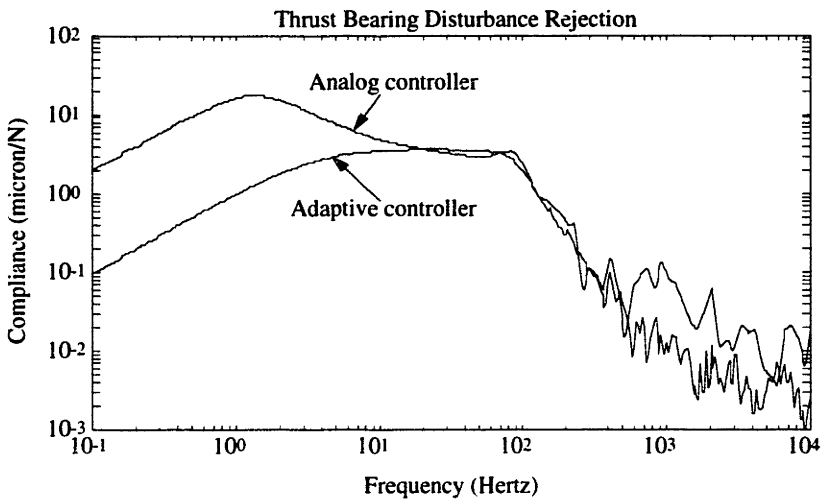

Figure 7.12: Disturbance rejection of thrust bearing under analog and adaptive controllers

for different operating speeds. Such superior performance of the adaptive controller is attributed to its abilitity to estimate the nonlinear, uncertain dyanmics on-line.

Nevertheless, for the adaptive controller, it can be noticed that the disturbance rejection gets degraded around $\omega = 875Hz$ as the the spinning speed increases. This is primarily due to the coupling between the gyroscopic effect and the rotor flexibility. A simple model shown in figure 7.15 explains the coupling behavior. Because the bearings present high stiffness at low frequencies, it makes sense to treat they as fixed point supports. Thus we can model the system as an overhung rotor with fixed supports in order to study the coupling behavior qualitatively. Figure 7.15 shows such a simple system. If it is further assumed that the rotor can be modeled as an axially symmetric spring with torsional spring constant $k_t = I_r\omega_t^2$, where ω_t is the first mode frequency of the rotor, then the equation of motion becomes [21]:

$$\ddot{\Psi} - j\frac{I_a}{I_r}\Omega\dot{\Psi} + \omega_t^2\Psi = \mathbf{0}, \tag{7.17}$$

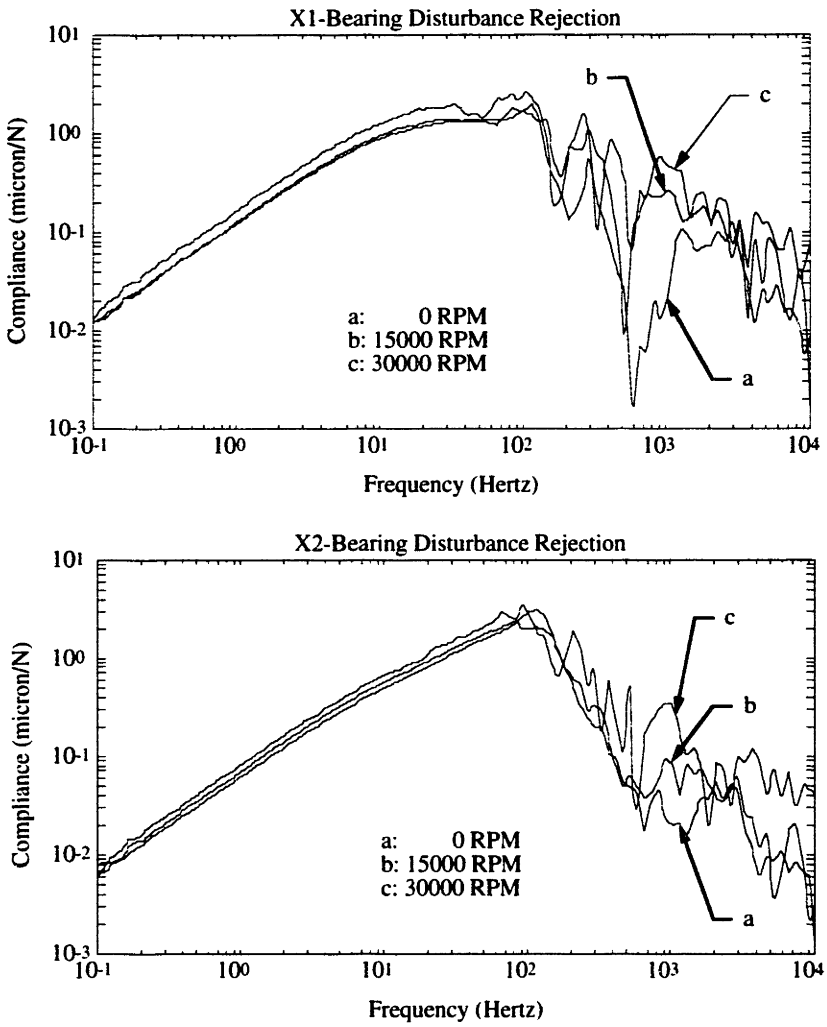

Figure 7.13: Disturbance rejection of radial bearings under adaptive controller

in which Ψ is a vectorial quantity and $\Psi = [\theta_{pitch}\ \varphi_{yaw}]^T$. The eigenvalues of the characteristic equation are given by:

$$\lambda = \pm j \left(\frac{I_a}{I_r} \frac{\Omega}{2} \pm \sqrt{\omega_t^2 + \left(\frac{I_a}{I_r} \frac{\Omega}{2} \right)^2} \right). \tag{7.18}$$

Consequently, as Ω increases, the poles associated with the first mode are splitted

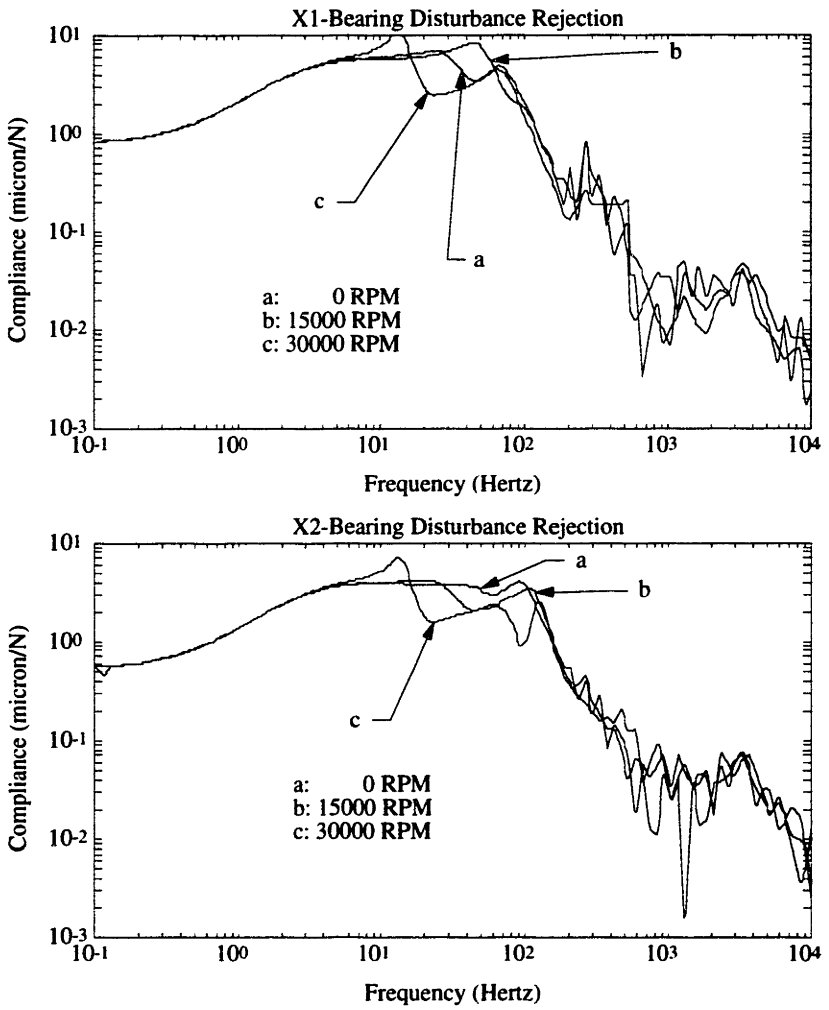

Figure 7.14: Disturbance rejection of radial bearings under analog controller

in the way that one pair goes to higher frequencies and the other goes to lower frequencies. Although the control system is equipped with notch filters with notch freqency equal to $875Hz$, at high speeds the width of the filters may not be wide enough to suppress the vibrations arising from the coupling effect described.

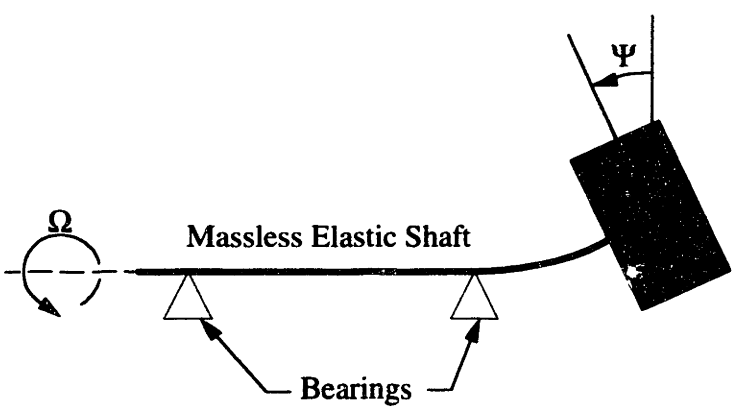

Figure 7.15: A simple overhung rotor with fixed supports model

Chapter 8

Conclusions and Recommendations

Total elimination of friction and the active control nature make magnetic bearings more attractive than conventional bearings. However, because of the unique behavior, issues associated with modeling, analysis and control need to be carefully studied. This thesis first presented a finite dimensional model for a magnetically levitated machine. The rigid rotor dynamics as well as the actuator dynamics were described. Such a model is used to motivated the three main research themes, namely, investigating achievable performance, obtaining a simple but accurate model and developing an adaptive controller that is robust to nonlinearities and changing dynamics.

Regarding the achievable performance of magnetically levitated machines, an analysis procedure is proposed. By applying the LTR methodology to systems in dimensionless form, the disturbance rejection characteristics for two different current control schemes were investigated. It was shown that while increasing the system bandwidth decreases the system compliances, the allowable unbalances are dominated by the hardware constraints.

On the modeling part, in order to further refine the simple finite dimensional model, more detailed system behavior such as flux leakages, fringing fluxes and the eddy current loss has been considered. Then Thevenin's theorem was used to obtain a simple equivalent model. Such an equivalent model is more capable of predicting the system behavior accurately because it makes good connection between the physics and experimental data. Thus one can use this model in extensive simulatione to facilitate the controller design.

Finally, we presented an adaptive scheme using local function estimation concept. This controller is able to tackle the actuator nonlinearities as well as the uncertainties arising from the gyroscopic effects in magnetically levitated rotating machines. By making some mild assumptions about the system functions and selecting the control parameters properly, stability can be guaranteed. Compared to other control methods, this scheme has a simpler structure which is more suitable for practical implementation. This controller was first validated using simulations based on the refined model. Then it was implemented as an alternative to an existing linear analog compensator. Experimental time responses were compared with the simulations. Disturbance rejection tests were also conducted for spinning and nonspinning conditions. Results indicate that the adaptive control system has much better stiffness properties at low frequencies. However, the disturbance rejection at high frequencies gets degraded as the spinning speed increases. A simple overhung rotor model showed that this phenomenon is unavoidable if the coupling between the gyroscopic effect and the rotor flexibility is not properly accounted for. Thus if a very high spinning speed is required, one either has to design adaptive notch filters with frequency tracking capabilities so as to avoid structural resonance, or to sacrifice the performace by designing less stiff bearing control systems.

Some issues in thesis can be further investigated. First, the analysis on the achievable performance uses LTR design. Some other control scheme such as H_∞ control, μ synthesis methods may also be employed to investigate how the hardware components constrain the system performance. In addition, the allowable unbalance analysis in section 3.4 is based on the fact that the magnetic cores and the power amplifiers are not saturated and thus the control system operates linearly. This assumption can lead to conservative results. Therefore, one may have to investigate how the saturation nonlinearities would affect the stability of the system and then perform stability

analysis using tools such as describing functions to compute the less conservative allowable unbalances.

In chapter 4, the modeling refining procedure strongly relies on the lumped-parameter approach to acquire the equivalent model. However, the true electromagnetic behavior is described by the Maxwell's equations. It would be interesting to solve these equations numerically and compare the results with the simple equivalent model. Then useful information for analysis and synthesis can be obtained.

For the control theory, since only the sufficient condition for stability is derived at this time, it may lead to a conservative design. A possible way in fixing this issue is to examine the nonlinear, uncertain system function in detail. For example, one can look into the system characteristics to investigate how the system function is composed, how many variables are involved, and thus reduce the dimensionality and make the estimation easier.

As far as the controller implementation to the magnetically levitated turbo pump is concerned, it was observed that the disturbance rejection at high frequencies gets degraded as the spinning speed increases. Consequently, to achieve better performance at high rotor speeds, further modifications on the adaptive controller need to be made so as to account for the coupling between the gyroscopic effect and the rotor flexibility.

Appendix A

LTR Designs with Integral Control

We start with adding integrators in each control channel to Eq.(3.7). While ignoring $\mathbf{d}_f$ and $\mathbf{d}_u$ for the purpose of simplicity, the state equations can be augumented as:

$$\begin{aligned}\begin{bmatrix}\dot{\mathbf{u}}_p\\ \dot{\mathbf{x}}_p\end{bmatrix} &= \begin{bmatrix}\mathbf{0} & \mathbf{0}\\ \mathbf{B}_p & \mathbf{A}_p\end{bmatrix}\begin{bmatrix}\mathbf{u}_p\\ \mathbf{x}_p\end{bmatrix}+\begin{bmatrix}\mathbf{I}\\ \mathbf{0}\end{bmatrix}\mathbf{u}\\ \mathbf{y} &= \begin{bmatrix}\mathbf{0} & \mathbf{C}_p\end{bmatrix}\begin{bmatrix}\mathbf{u}_p\\ \mathbf{x}_p\end{bmatrix}.\end{aligned} \tag{A.1}$$

Because only the control of the radial bearing system is considered here, the design plant model is a 12th order system in the form of Eq.(3.1). The new control vector is $\mathbf{u}$ and the new state vector is $\mathbf{x}^T = \left[\mathbf{u}_p^T, \mathbf{x}_p^T\right]$ in which $\mathbf{x}_p$ consists of four position measurements and four velocity measurments. Furthermore,

$$\mathbf{A} = \begin{bmatrix}\mathbf{0} & \mathbf{0}\\ \mathbf{B}_p & \mathbf{A}_p\end{bmatrix},\ \mathbf{B} = \begin{bmatrix}\mathbf{I}\\ \mathbf{0}\end{bmatrix},\ \mathbf{C} = \begin{bmatrix}\mathbf{0} & \mathbf{C}_p\end{bmatrix}. \tag{A.2}$$

In order to achieve the approximation in Eq.(3.4), $\mathbf{L}$, the process noise influencing matrix has to be selected carefully. Here we adopt the method in [6] to select $\mathbf{L}$. Writing $\mathbf{L}^T = \left[\mathbf{L}_L^T, \mathbf{L}_H^T\right]$, the matrix $\mathbf{C}(j\omega\mathbf{I}-\mathbf{A})^{-1}\mathbf{L}$ in Eq.(3.3) can be expanded as:

$$\begin{aligned}\mathbf{C}(j\omega\mathbf{I}-\mathbf{A})^{-1}\mathbf{L} &= \begin{bmatrix}\mathbf{0} & \mathbf{C}_p\end{bmatrix}\\ &\begin{bmatrix}\frac{\mathbf{I}}{j\omega} & \mathbf{0}\\ \frac{(j\omega\mathbf{I}-\mathbf{A}_p)^{-1}\mathbf{B}_p}{j\omega} & (j\omega\mathbf{I}-\mathbf{A}_p)^{-1}\end{bmatrix}\begin{bmatrix}\mathbf{L}_L\\ \mathbf{L}_H\end{bmatrix}\\ &= \frac{\mathbf{C}_p(j\omega\mathbf{I}-\mathbf{A}_p)^{-1}\mathbf{B}_p\mathbf{L}_L}{j\omega} + \mathbf{C}_p(j\omega\mathbf{I}-\mathbf{A}_p)^{-1}\mathbf{L}_H.\end{aligned} \tag{A.3}$$

At high frequencies, or $\omega \to \infty$, it easy to see that

$$\mathbf{C}(j\omega\mathbf{I}-\mathbf{A})^{-1}\mathbf{L} \to \frac{\mathbf{C}_p\mathbf{L}_H}{j\omega}. \tag{A.4}$$

Thus $\mathbf{L}_H$ can be selected, say, $\mathbf{L}_H = \mathbf{C}_p^T \left[\mathbf{C}_p\mathbf{C}_p^T\right]^{-1}$, to influence the high frequency behavior of the target feedback loop so that Eq.(3.4) is true at high frequencies. Note that $\mathbf{L}_L$ is still available as a design parameter. It can be selected to match the singular values at low frequencies. However, one needs some caution in selecting $\mathbf{L}_L$.

The matrix $\mathbf{A}_p$ in the bias current linearization scheme is nonsingular. Therefore, at low frequencies, or $\omega \to 0$, we have

$$\begin{aligned}\mathbf{C}(j\omega\mathbf{I}-\mathbf{A})^{-1}\mathbf{L} &\to -\frac{\mathbf{C}_p\mathbf{A}_p^{-1}\mathbf{B}_p\mathbf{L}_L}{j\omega} - \mathbf{C}_p\mathbf{A}_p^{-1}\mathbf{L}_H \\ &\approx -\frac{\mathbf{C}_p\mathbf{A}_p^{-1}\mathbf{B}_p\mathbf{L}_L}{j\omega}. \end{aligned} \tag{A.5}$$

Consequently, one can select $\mathbf{L}_L = -\left[\mathbf{C}_p\mathbf{A}_p^{-1}\mathbf{B}_p\right]^{-1}$ to make $\mathbf{C}(j\omega\mathbf{I}-\mathbf{A})^{-1}\mathbf{L}$, or $\mathbf{G}_{KF}(j\omega)$, behave like $\frac{\mathbf{I}}{j\omega}$ at low frequencies.

On the other hand, $\mathbf{A}_p$ in the input-state linearization scheme is singular due to the rigid body motions of the rotor, the above selection of $\mathbf{L}_L$ does not apply here. Nevertheless, the special structures of $\mathbf{A}_p$, $\mathbf{B}_p$, and $\mathbf{C}_p$, namely, $\mathbf{A}_p = \begin{bmatrix} \mathbf{0} & \mathbf{I} \\ \mathbf{0} & \mathbf{G} \end{bmatrix}$, $\mathbf{B}_p = \begin{bmatrix} \mathbf{0} \\ \mathbf{B}_1 \end{bmatrix}$, and $\mathbf{C}_p = \begin{bmatrix} \mathbf{I} & \mathbf{0} \end{bmatrix}$, provide us an insight to choose $\mathbf{L}_L$. First, one can express the resolvent matrix $(j\omega\mathbf{I}-\mathbf{A})^{-1}$ as

$$(j\omega\mathbf{I}-\mathbf{A}_p)^{-1} = \begin{bmatrix} \frac{\mathbf{I}}{j\omega} & \frac{(j\omega\mathbf{I}-\mathbf{G})^{-1}}{j\omega} \\ \mathbf{0} & (j\omega\mathbf{I}-\mathbf{G})^{-1} \end{bmatrix}. \tag{A.6}$$

Then at low frequencies,

$$\begin{aligned}\mathbf{C}(j\omega\mathbf{I}-\mathbf{A})^{-1}\mathbf{L} &\to \frac{\mathbf{C}_p(j\omega\mathbf{I}-\mathbf{A}_p)^{-1}\mathbf{B}_p\mathbf{L}_L}{j\omega} \\ &= -\frac{(j\omega\mathbf{I}-\mathbf{G})^{-1}\mathbf{B}_1\mathbf{L}_L}{\omega^2}. \end{aligned} \tag{A.7}$$

Because $\mathbf{B}_1$ is always nonsingular, and $\mathbf{G} \approx \mathbf{0}$ at low rotation speed and nonsingular otherwise, one can select $\mathbf{L}_L = -\mathbf{B}_1^{-1}$ so that

$$\mathbf{C}(j\omega\mathbf{I}-\mathbf{A})^{-1}\mathbf{L} \to \frac{\mathbf{I}}{(j\omega)^3} \tag{A.8}$$

at low rotation speeds and select $\mathbf{L}_L = -\mathbf{B}_1^{-1}\mathbf{G}$ so that

$$\mathbf{C}(j\omega\mathbf{I} - \mathbf{A})^{-1}\mathbf{L} \rightarrow \frac{\mathbf{I}}{(j\omega)^2} \tag{A.9}$$

otherwise. Note that both Eq.(A.8) and Eq.(A.9) are only valid at low frequencies.

Appendix B

System Bandwidth Constraints Imposed by the Flexibility Effects

The equations of motion in Eq.(2.3) assumed that the rotor is rigid; thus ignored the flexibility effects. In the reality, the rotor is not infinitely rigid and the flexural effects usually have significant influence on the stability of the control system. Among the flexibility effects, the bending modes of the rotor are particullary dominating in rotating machine applications [7]. For the purpose of investigating how the bending effects constrain the system banwidth, we start by constructing a flexible rotor model.

Figure B.1 shows a flexible rotor acted upon by two external forces, F_{x1} and F_{x2} which are generated by the x_1 and x_2 bearings respectively. The rotor is made of material with Young's modulus equal to E and density equal to ρ. The cross-sectional area of the rotor is A and the the area moment of inertia about the neutral axial is I. If the rotor is at rest, according to the Bernoulli-Euler beam theory, the equation of motion in the X direction can be written as [11, 24]:

$$EI\frac{\partial^4 w}{\partial v^4} + \rho A\frac{\partial^2 w}{\partial t^2} = F_{x1}\delta(v - v_1) + F_{x2}\delta(v - v_2), \tag{B.1}$$

where $\delta(.)$'s are impluse functions and $w(v,t)$ is the x-direction displacement of the position v at the time t. The partial differential equation has force free boundary conditions which mean that no shear force and no moment exist at $v = 0$ and $v = L$. The boundary conditions can be written in terms of $w(v,t)$ as

$$\frac{\partial^2 w}{\partial x^2}(0,t) = \frac{\partial^2 w}{\partial x^2}(L,t) = 0 \text{ for the zero-moment constraint,} \tag{B.2}$$

and

$$\frac{\partial^3 w}{\partial x^3}(0,t) = \frac{\partial^3 w}{\partial x^3}(L,t) = 0 \text{ for the zero-shear constraint.} \tag{B.3}$$

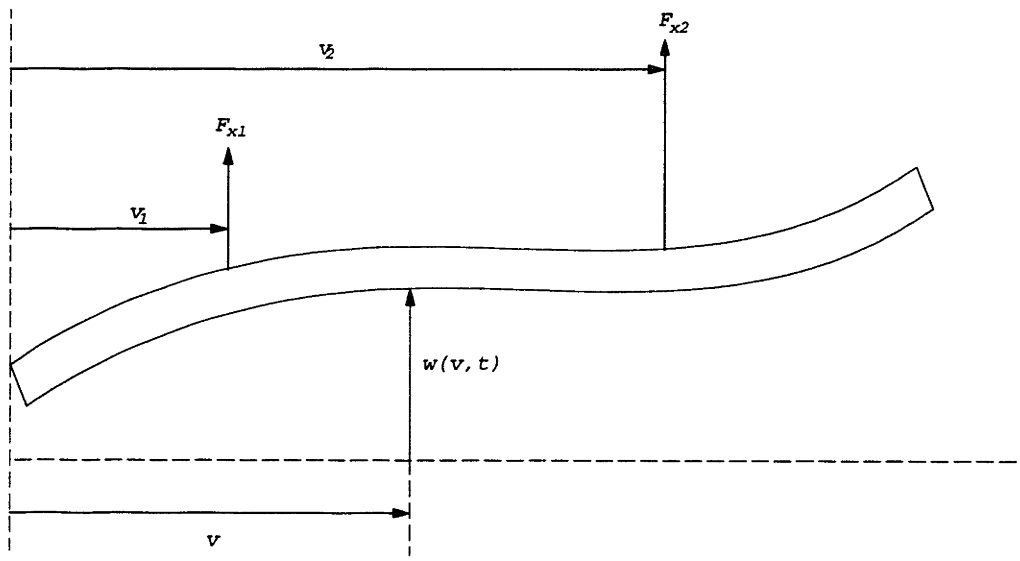

Figure B.1: A Bernoulli-Euler beam with point forcing

The assumed-mode method in [30] can be used to solve for $w(v,t)$. It is assumed in this method that the forced solution has the form

$$w(v,t) = \sum_{n=0}^{n=\infty} Y_n(v)\zeta_{nx}(t), \tag{B.4}$$

where $Y_n(v)$ is the mode shape function of the nth mode and $\zeta_{nx}(t)$ is the associated coordinate. We substitute this solution into Eq.(B.1) and then multiply each term by $Y_m(v)$ and integrate with respect ot v from $v = 0$ to $v = L$. With the help of the orthogonality property of the mode shapes, we obtain

$$m_n\ddot{\zeta}_{nx} + m_n\omega_n\zeta_{nx} = F_{x1}Y_n(v_1) + F_{x2}Y_n(v_1), \tag{B.5}$$

where $m_n = \int_0^L \rho A Y_n^2 dv$ is the modal mass and w_n is the natural frequency. Both are associated with the nth mode.

In this simple analysis, only the rigid body motion and the first bending mode are of interest. Therefore, the infinite series in Eq.(B.4) are truncated to three terms, namely,

$$w(v,t) = Y_0(v)\zeta_0(t) + Y_1(v)\zeta_1(t) + Y_2(v)\zeta_2(t), \tag{B.6}$$

in which $Y_0(v)$ and $Y_1(v)$ represent the modes for the rigid body translation and rotation, both having natural frequencies equal to 0, and $Y_2(v)$ is the mode shape for the first bending mode. Because there exists a linear transformation between $[\zeta_{0x}, \zeta_{1x}]$ and $[x_1, x_2]$, the two equations of motion in ζ_{0x} and ζ_{1x} coordinates can also be represented by the first two equations in Eq.(2.3) with $\Omega = 0$. Moreover, we have

$$x_{1true} = w(v_1,t) = Y_0(v_1)\zeta_{0x}(t) + Y_1(v_1)\zeta_{1x}(t) + Y_2(v_1)\zeta_{2x}(t), \tag{B.7}$$

$$x_{2true} = w(v_2,t) = Y_0(v_2)\zeta_{0x}(t) + Y_1(v_2)\zeta_{1x}(t) + Y_2(v_2)\zeta_{2x}(t), \tag{B.8}$$

where x_{1true} and x_{2true} represent the true displacements of the rotor at x_1 and x_2 bearing locations. Consequently, the overall system dynamics can be describe by the block diagram in Figure B.2.

In this block diagram, the plant $\mathbf{P}$ consists of the first four equations of Eq. (2.3) (the disturbances are ignored in this case), and can be written as $\mathbf{P} = \mathbf{C}_p(s\mathbf{I} - \mathbf{A}_p)^{-1}\mathbf{B}_p$, where $\mathbf{A}_p$, $\mathbf{B}_p$ and $\mathbf{C}_p$ are the matrices in Eq.(3.7) corresponding to the input-state linearization scheme. It is assumed that the dynamics in the Y direction has similar characteristics as that of the X direction and the analysis is still valid when the rotor spins. Furthermore, rather than assuming the system possesses no damping, a modal damping coefficient ξ is introduced.

Based on the previous discussion, the nominal model $\mathbf{P}$ and $\mathbf{\Delta P}$ due to the first bending mode effect comprise the true system dynamics. Since the LTR design uses the nominal model, the critical issue here is to assure the control system is robust

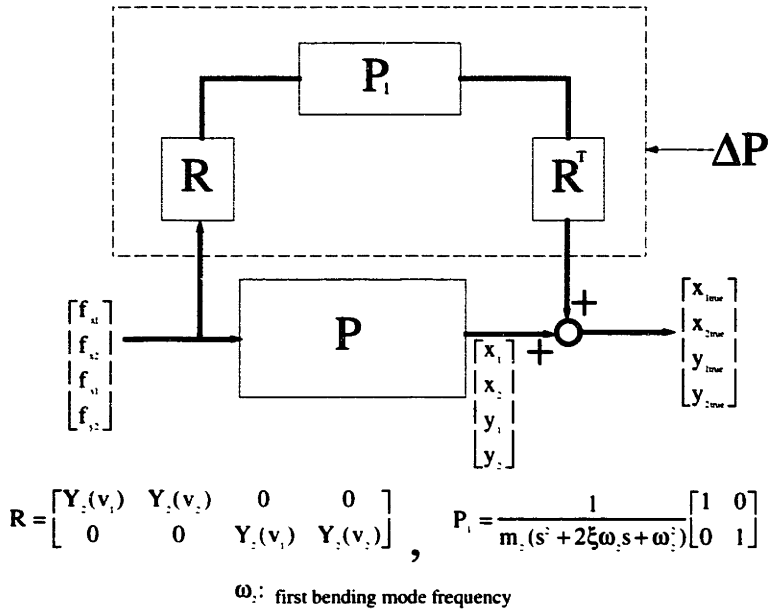

Figure B.2: A block diagram describing the rigid body motion and the first bending mode effect

against the purturbation ΔP. Here we employ some results in the robust control theory to test the robust stability of the control system.

In [12, 14], the small gain theorem is used to prove that a stabilizing controller $\mathbf{C}$ for the plant P can provide robust stability for the plant $\mathbf{P} + \mathbf{\Delta P}$ if

$$\|\mathbf{\Delta P}\,(\mathbf{I} + \mathbf{CP})^{-1}\,\mathbf{C}\|_\infty < 1, \tag{B.9}$$

where $\|.\|_\infty$ denotes the infinity norm of the associated transfer function. In other words, in Figure B.3, if the infinity norm of the product of $\mathbf{\Delta P}$ and the transfer function from ζ_2 to $\mathbf{f}$ is less than 1, the control system is robust stable. The condition in Eq.(B.9) is only a sufficient condiditon and it can be satisfied if

$$\sigma_{max}\left[\mathbf{\Delta P}(j\omega)\right] < \sigma_{max}^{-1}\left[(\mathbf{I} + \mathbf{C}(j\omega)\mathbf{P}(j\omega))^{-1}\,\mathbf{C}(j\omega)\right]. \tag{B.10}$$

This stability test can be immediately applied to the LTR control system using the input-state linearization scheme. In this case,

$$\mathbf{\Delta P} \;=\; \mathbf{R}^T\mathbf{P}_1\mathbf{R}$$

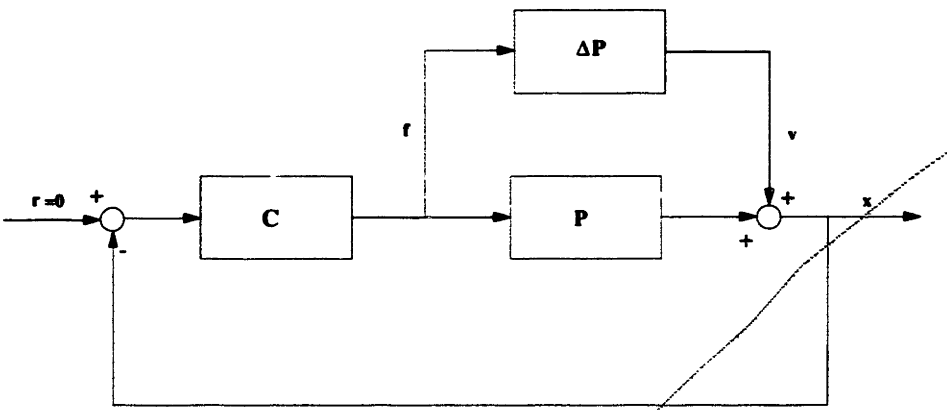

Figure B.3: A block diagram demonstrating the robust stability test for the input-state linearization scheme

$$= \frac{1}{m_2(s^2 + 2\xi\omega_2 s + \omega_2^2)} \mathbf{R}^T\mathbf{R}. \tag{B.11}$$

Using the relation $\sigma_{max}\left[\mathbf{R}^T\mathbf{R}\right] = \sigma_{max}\left[\mathbf{R}\mathbf{R}^T\right]$, we have

$$\sigma_{max}\left[\mathbf{\Delta P}(j\omega)\right] = \frac{1}{m_2'(s^2 + 2\xi\omega_2 s + \omega_2^2)}, \tag{B.12}$$

where $m_2' = \frac{m_2}{\sqrt{Y_2^2(v_1)+Y_2^2(v_2)}}$ is the equivalent modal mass. Now, the robust stability condition becomes

$$\left|\frac{1}{m_2'((j\omega)^2 + 2\xi\omega_2(j\omega) + \omega_2^2)}\right| < \sigma_{max}^{-1}\left[(\mathbf{I} + \mathbf{C}(j\omega)\mathbf{P}(j\omega))^{-1}\mathbf{C}(j\omega)\right] \quad \forall\omega. \tag{B.13}$$

It can be concluded from the above inequality that if the inverse of the maximum signular value of the transfer function $(\mathbf{I}+\mathbf{CP})^{-1}\mathbf{C}$ is larger than the magnitude of $\left|\frac{1}{m_2'((j\omega)^2+2\xi\omega_2(j\omega)+\omega_2^2)}\right|$ for all frequencies, then the controller also guarantee robust stable against the first bending mode.

The robust stability test of the LTR control system, which is designed based on the nominal model in Eq.(3.7), for the input-state linearizaiton scheme is shown in Figure B.4. In this figure, the rotor is assumed spinning at $25000RPM$ and the function $\sigma_{max}^{-1}\left[(\mathbf{I}+\mathbf{C}(j\omega)\mathbf{P}(j\omega))^{-1}\mathbf{C}(j\omega)\right]$ is plotted for different bandwidths. Due to the complexities of the rotors, the acquisition of parameters m_2', ξ, and ω_2 usually rely on performing system identification experimentally. For the purpose of illustration, $m_2' = 4.0kg$, $\xi = 0.08$, $\omega_2 = 875Hz$ are adpoted and the magintude plot of $\frac{1}{m_2'((j\omega)^2+2\xi\omega_2(j\omega)+\omega_2^2)}$ is also shown in this figure. Clearly, as the normalized system bandwith increases over 4, the condition in Eq. B.13 is violated and the control system may loose its stability due to the first mode bending effect. With a larger equivalent model mass m_2', a higher bending frequency ω_2 and a larger modal damping ratio ξ, it is more likely the control system can have robust stability. Besides, among all the three factors, the damping effect is more prevalent over the other two because the violation of Eq. B.13 mainly occurs at the peak of the function on the left of this inequality and the size of the peak is inversely proportional to the modal damping. Notice in Figure B.4, dimensionless parameters are used; thus m_2' is normalized with respect to m, the mass of the rotor, while ω_2 is normalized with respect to ω_n.

Similar analysis procedure can be also applied to the control system associated with the bias current linearization scheme. However, the control variables now are the currents instead of the magnetic forces. Figure B.5 shows such a control system, in which $\mathbf{P}$ and $\mathbf{\Delta P}$ have the same meanings as before. Because the magnetic force in the bias current linearization scheme is a linear combination of the current and the

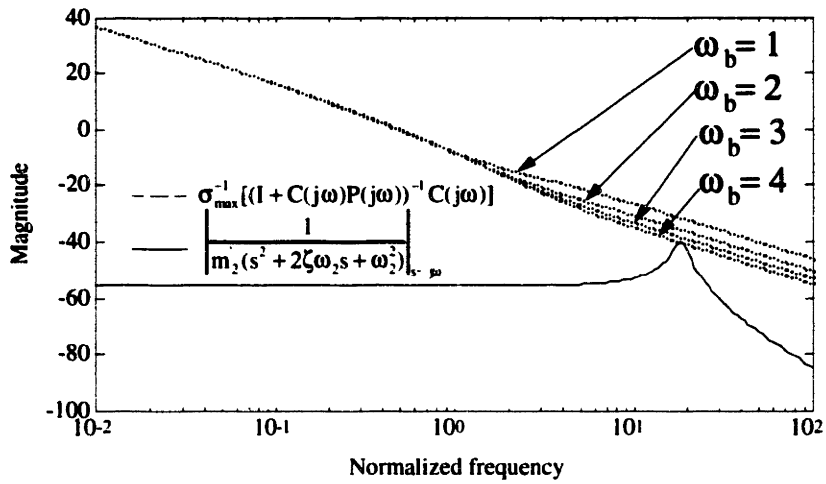

Figure B.4: Robust stability tests of LTR control system using the input-state linearization scheme

displacement, we have

$$\mathbf{f} = \kappa \mathbf{K}_1 \mathbf{x} + \mathbf{K}_1 \mathbf{i}, \tag{B.14}$$

where the expressions for $\mathbf{f}$, $\mathbf{K}_1$, $\mathbf{x}$ and $\mathbf{i}$ can be found in Figure B.5. Therefore, using the notations in Eq.(3.7), the following relation holds:

$$\mathbf{C}_p \left(s\mathbf{I} - \mathbf{A}_p\right)^{-1} \mathbf{B}_p = \left(\mathbf{I} - \kappa \mathbf{P}\mathbf{K}_1\right)^{-1} \mathbf{P}\mathbf{K}_1, \tag{B.15}$$

since both sides of the equality represent the transfer function from $\mathbf{i}$ to $\mathbf{x}$. Again, using the small gain theorem, it can be shown that the controller provides the robust stability if the infinity norm of the product $\mathbf{\Delta P}$ and $\left(\mathbf{I} + \mathbf{K}_1\mathbf{C}\mathbf{P} - \kappa \mathbf{K}_1 \mathbf{P}\right)^{-1} \left(\kappa \mathbf{K}_1 - \mathbf{K}_1 \mathbf{C}\right)$. which is the transfer function from $\mathbf{v}$ to $\mathbf{f}$ in Figure B.5, is less than 1.

The robust stability test is applied to the LTR control system associated with the bias current linearization scheme and the results are shown in Figiure B.6. The parameters and the operating conditions are the same as the previous case. The robust

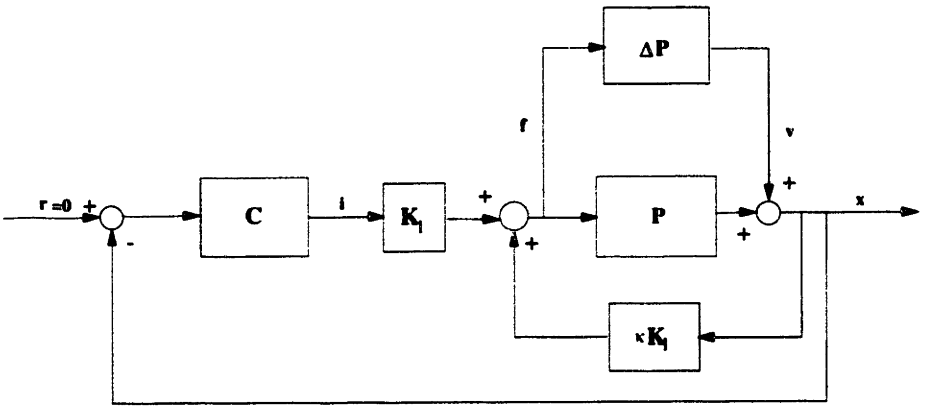

Robust stability test: $\left\|\Delta P \bullet (I + K_I CP - \kappa K_I P)^{-1} \bullet (\kappa K_I - K_I C)\right\|_\infty < 1$

$$i = \begin{bmatrix} i_{x1} \\ i_{x2} \\ i_{y1} \\ i_{y2} \end{bmatrix} \qquad K_I = \kappa \begin{bmatrix} \alpha & \beta & 0 & 0 \\ \beta & \gamma & 0 & 0 \\ 0 & 0 & \alpha & \beta \\ 0 & 0 & \beta & \gamma \end{bmatrix}$$

Figure B.5: A block diagram demonstrating the robust stability test for the bias current linearization scheme

stability condition is violated when $\omega_b \geq 2$. Comparing Figure B.4 and Figure B.6, one can conclude that the control system associated with the bias current linearization scheme is more susceptible to the flexibility effects than the control system assocated with the input-state linearization scheme. This is possibly due to the instability introduced by the former scheme.

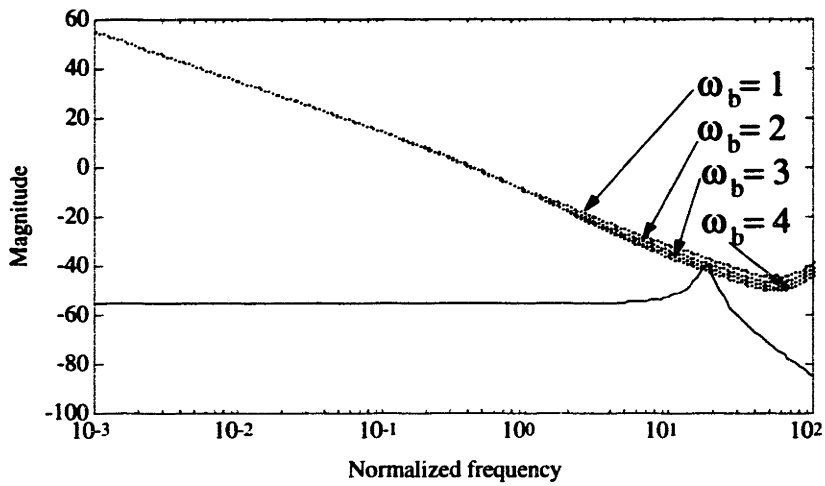

Figure B.6: Robust stability tests of LTR control system using the bias current linearization scheme

Appendix C
Fringing Flux Effects

The model-refining procedure in Section 4.4 strongly relies on the assumption that the magnetic forces contributed from the fringing fluxes are negligible compared to those due to the useful fluxes, so that one can isolate the air gap capacitance C_a and obtain an equivalent description for the effort-source-capacitance network. In this section, a justification on this assumption using the radial bearing as an example is given.

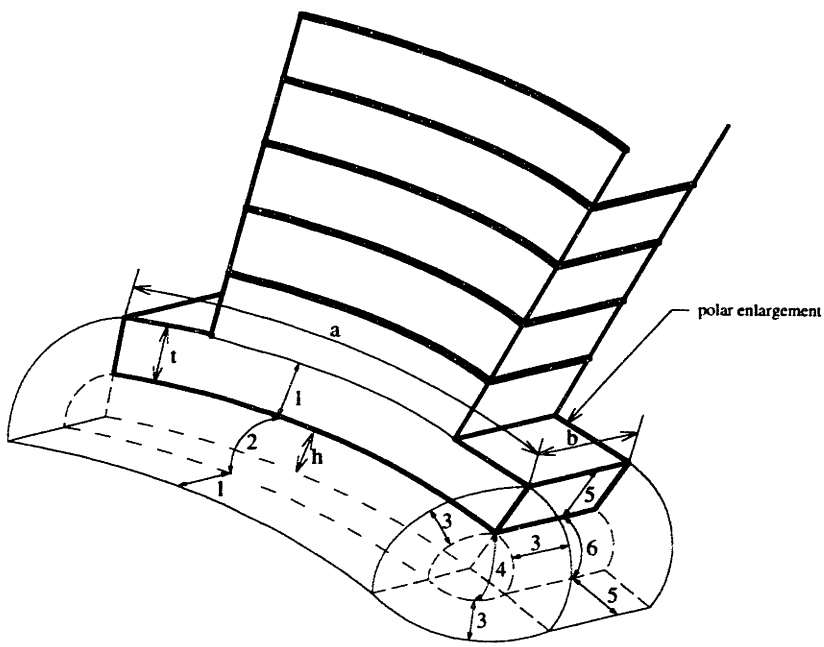

Figure C.1: Typical fringing fluxes existing in the radial bearing

Figure C.1 shows the typical fringing fluxes existing in the radial bearing. The total fringing flux path consists of several simple paths. These paths can be categorized into six types which are designated by numbers 1 to 6 in the same figure. Also using the dimensions a, b, t, h labeled in this figure, one can obtain the capacitance of each type of flux paths[35]:

Type-1 flux path. This type of flux flows either from the front or the rear face of the polar enlargement to the rotor surface. Therefore, there are two type-1 paths. The capacitance of each path is given by:

$$C_1 = \frac{2\mu_0 a}{\pi} \ln(1 + \frac{2t}{h}). \tag{C.1}$$

Type-2 flux path. This type of flux flows from the edge of the front or the rear face of the polar enlargement to the rotor surface. Therefore, there are two type-2 paths. The capacitance of each path is given by:

$$C_2 = 0.52\mu_0 a. \tag{C.2}$$

Type-3 flux path. This type of flux flows from each corner edge of the polar enlargement to the rotor surface. The fringing flux is in the shape of a one-eighth spherical shell, and there are four type-3 paths. The capacitance of each path is given by:

$$C_3 = \frac{\mu_0 t}{2}. \tag{C.3}$$

Type-4 flux path. This type of flux flows from each corner of the polar enlargement to the rotor surface. The fringing flux is in the shape of a one-eighth spherical, and there are four type-4 paths. The capacitance of each path is given by:

$$C_4 = 0.308\mu_0 h. \tag{C.4}$$

Type-5 flux path. This type of flux flows from the either side face of the polar enlargement to the rotor surface. Therefore, there are two type-5 paths. The capacitance of each path is given by:

$$C_5 = \frac{2\mu_0 b}{\pi} \ln(1 + \frac{2t}{h}). \tag{C.5}$$

Type-6 flux path. This type of flux flows from the edge of the either side face of the polar enlargement to the rotor surface. Therefore, there are two type-6 paths. The capacitance of each path is given by:

$$C_6 = 0.52\mu_0 b. \tag{C.6}$$

Finally, the capacitance for the useful flux is given by

$$C_a = \frac{\mu_0 ab}{h} \tag{C.7}$$

A bond graph model characterizing the magnetic fluxes in Figure C.1 is shown in Figure C.2.(a). Because the fringing flux paths and the useful flux path connect the polar enlargement to the rotor surface, they share the same magnetomotive force and a 0 junction can be used to represent such a parallel connection. The generalized capacitive elements associated with the fringing paths can be further combined into a single capacitor with the capacitance

$$C_f = 2C_1 + 2C_2 + 4C_3 + 4C_4 + 2C_5 + 2C_6. \tag{C.8}$$

Now we can use expressions similar to Eq.(2.4) to determine the magnetic forces contributed by the fringing fluxes and the useful flux. For the fringing fluxes, the associated magnetic force F_f is given by:

$$F_f = -\frac{\partial \mathcal{E}_f}{\partial h} = -\frac{M^2}{2}\frac{dC_f}{dh}, \tag{C.9}$$

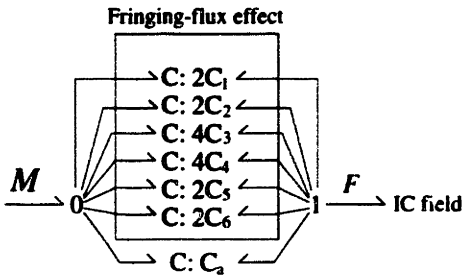

(a)

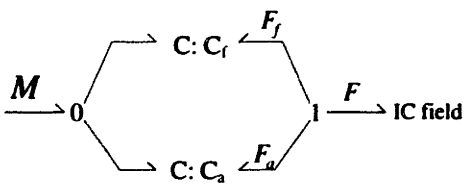

(b)

Figure C.2: Bond graph representations of the fringing fluxes and the useful flux

where $\mathcal{E}_f$ is the magnetic energy stored in the fringing fluxes and M is the magnetomotive force. For the useful fluxes, the associated magnetic force F_a is given by:

$$F_a = -\frac{\partial \mathcal{E}_a}{\partial h} = -\frac{M^2}{2}\frac{dC_a}{dh}, \tag{C.10}$$

where $\mathcal{E}_a$ is the magnetic energy stored in the useful flux.

Eq.(C.9) and Eq.(C.10) together allow one to compute the ratio $\frac{F_f}{F_a}$, which is given by:

$$\frac{F_f}{F_a} = \frac{\frac{dC_f}{dh}}{\frac{dC_a}{dh}} = \frac{8(a+b)ht}{\pi ab(h+2t)} - \frac{1.232g^2}{\pi ab}. \tag{C.11}$$

For the radial bearings of the turbo pump in this study, $a = 0.75cm$, $b = 1.3cm$, $t = 0.375cm$, and $h = 250\mu m$. Substituting these values into Eq. (C.11), we have

$\frac{F_f}{F_a} = 0.0645$, which justifies the assumption that the magnetic force due to the fringing fluxes is negligible compared to the force coming from the useful flux.

Appendix D

Modeling of the Eddy Current Loss

If the magnetic bearing is made up of n_o laminations of ferromagnetic sheet insulated from one another as shown in Fig. D.1, the power loss P_{eddy} of the core can be calculated and written as[44]:

$$\begin{aligned} P_{eddy} &= \frac{a^2}{4k\rho n_o^2}\left(\frac{dB}{dt}\right)^2 (lah) \\ &= \frac{la}{4k\rho h n_o^2}\left(\frac{d\phi}{dt}\right)^2 \end{aligned} \tag{D.1}$$

where ρ is the resistivity of the material. l is the mean circumference of the core and k is a constant which accounts for the fact that the paths near the surface will have larger induced emf's than those in the interior of the lamination.

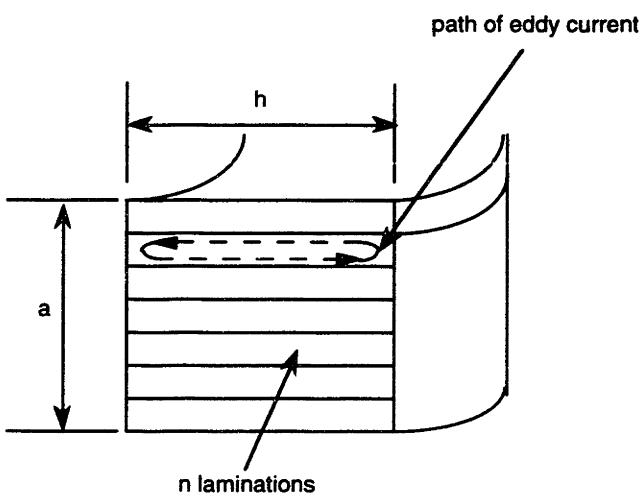

Figure D.1: Laminated Magnetic Core

In the bond graph analogy, the power dissipated for the resistive element R is equal to $R\left(\frac{d\phi}{dt}\right)^2$. Therefore we can identify the resistance induced by the eddy current as $R_e = \frac{la}{4k\rho hn_o^2}$. In addition, Eq D.1 also shows that when a sinusoidal flux is existing in the magnetic circuit, the energy dissipated by the eddy current effect would be proportional to the frequency squared.

Appendix E

Proof of Theorem 5.1

The proof of Theorem 5.3.1 depends on the following lemma.

Lemma E.0.1 *If* $\|\mathbf{B}_m\mathbf{r}(t)\| \leq r$ *for all* $t \geq 0$, *then the reference trajectory* $\mathbf{x}_m(t)$ *is Lipschitz continuous. In other words, a Lipschitz constant* M_m *exists so that*

$$\|\mathbf{x}_m(t_a) - \mathbf{x}_m(t_b)\| \leq M_m|t_a - t_b|, \quad \forall t_a, t_b \geq 0. \tag{E.1}$$

Proof: Let us start by estimating $\|e^{\mathbf{A}_m t}\|$. Consider a linear system described by

$$\dot{\mathbf{z}} = \mathbf{A}_m\mathbf{z}. \tag{E.2}$$

We define a Lyapunov function $\mathcal{V}$ with $\mathcal{V} = \frac{1}{2}\mathbf{z}^T\mathbf{P}\mathbf{z}$. Using Eqs.(5.13) and (E.2), we get $\dot{\mathcal{V}} = -\frac{1}{2}\mathbf{z}^T\mathbf{z}$. Since

$$\mathbf{z}^T\mathbf{z} = \frac{1}{\lambda_{max}[\mathbf{P}]}\lambda_{max}[\mathbf{P}]\mathbf{z}^T\mathbf{z} \geq \frac{2}{\lambda_{max}[\mathbf{P}]}\mathcal{V}, \tag{E.3}$$

it is implied that

$$\dot{\mathcal{V}} \leq -\frac{1}{\lambda_{max}[\mathbf{P}]}\mathcal{V}. \tag{E.4}$$

Accordingly, we have

$$\begin{aligned} \frac{1}{2}\lambda_{min}[\mathbf{P}]\|\mathbf{z}(t)\|^2 \leq \mathcal{V}(t) &\leq \mathcal{V}(0)e^{-\frac{1}{\lambda_{max}[\mathbf{P}]}t} \\ &\leq \frac{1}{2}\lambda_{max}[\mathbf{P}]\|\mathbf{z}(0)\|^2 \end{aligned} \tag{E.5}$$

$\forall t \geq 0$, or $\|\mathbf{z}(t)\| \leq \sqrt{\frac{\lambda_{max}[\mathbf{P}]}{\lambda_{min}[\mathbf{P}]}}\|\mathbf{z}(0)\|$. This, together with the fact that Eq.(E.2) has a unique solution $\mathbf{z}(t) = e^{\mathbf{A}_m t}\mathbf{z}(0)$, means that

$$\|e^{\mathbf{A}_m t}\mathbf{z}(0)\| \leq \sqrt{\frac{\lambda_{max}[\mathbf{P}]}{\lambda_{min}[\mathbf{P}]}}\|\mathbf{z}(0)\| \quad \forall t \geq 0. \tag{E.6}$$

Because Eq.(E.6) holds for all $\mathbf{z}(0) \in \mathcal{R}^n$, we have

$$\|e^{\mathbf{A}_m t}\| \leq \sqrt{\frac{\lambda_{max}[\mathbf{P}]}{\lambda_{min}[\mathbf{P}]}} \quad \forall t \geq 0. \tag{E.7}$$

Next, notice that $\mathbf{x}_m(t)$ has the form

$$\mathbf{x}_m(t) = e^{\mathbf{A}_m t}\mathbf{x}_m(0) + \int_0^t e^{\mathbf{A}_m(t-\tau)}\mathbf{B}_m\mathbf{r}(\tau)d\tau. \tag{E.8}$$

Substituting this solution back into Eq.(5.2) and taking norms give us

$$\begin{aligned}\|\dot{\mathbf{x}}_m(t)\| &\leq \|\mathbf{A}_m e^{\mathbf{A}_m t}\mathbf{x}_m(0)\| \\ &+\|\mathbf{A}_m \int_0^t e^{\mathbf{A}_m(t-\tau)}\mathbf{B}_m\mathbf{r}(\tau)d\tau\| + \|\mathbf{B}_m\mathbf{r}(t)\|.\end{aligned} \tag{E.9}$$

Because of Eq.(E.6) and $\|\mathbf{B}_m\mathbf{r}(t)\| \leq r \ \forall t \geq 0$, we can futher reduce Eq.(E.9) to

$$\begin{aligned}\|\dot{\mathbf{x}}_m(t)\| \leq \|\mathbf{A}_m\|\sqrt{\frac{\lambda_{max}[\mathbf{P}]}{\lambda_{min}[\mathbf{P}]}}\|\mathbf{x}_m(0)\| \\ + \left(\sqrt{\frac{\lambda_{max}[\mathbf{P}]}{\lambda_{min}[\mathbf{P}]}} + 2\right) r\end{aligned} \tag{E.10}$$

$\forall t \geq 0$, by using the fact that $\|\mathbf{A}_m \int_0^t e^{\mathbf{A}_m(t-\tau)}d\tau\| = \|e^{\mathbf{A}_m t} - \mathbf{I}\| \leq \|e^{\mathbf{A}_m t}\| + 1$.

Choosing $M_m = (\|\mathbf{A}_m\|\|\mathbf{x}_m(0)\| + r)\sqrt{\frac{\lambda_{max}[\mathbf{P}]}{\lambda_{min}[\mathbf{P}]}} + 2r$, we have $\|\dot{\mathbf{x}}_m(t)\| \leq M_m$. Consequently, the Lipschitz continuity of $\mathbf{x}_m$ follows by the Mean-Value Theorem. □

We are now in the position to prove Theorem 5.3.1.

Proof of Theorem 5.3.1: We prove this theorem by contradiction. Denoting the function $\|\mathbf{f}(\mathbf{x}) - \mathbf{f}_1(\mathbf{x}, \mathbf{x}_i)\|$ by $d_i(t)$, then it is continuous because of the smoothness of $\mathbf{f}(\mathbf{x})$ and the continuity of the state trajectory $\mathbf{x}(t)$. First assume that there exists $t_i' > t_i$ such that $d(t_i') > \epsilon$. Because $d(t_i) = 0$, we can infer that the set $\mathcal{S}_i = \{t \mid d_i(t) = \epsilon, \ \ t_i < t < t_i'\}$ is nonempty by the intermediate value theorem[1].

[1]The intermediate value theorem states that for a continuous function f on a closed interval $\mathcal{S} \supset \mathcal{R}$, if there are two points $\alpha < \beta$ in $\mathcal{S}$ such that $f(\alpha) \neq f(\beta)$, then f takes every value between $f(\alpha)$ and $f(\beta)$ in the interval (α, β).

Let t_i^* be the minimum element of $\mathcal{S}_i$; i.e., $t_i^* = min\mathcal{S}_i$; then $d_i(t) \leq \epsilon$ for $t_i \leq t \leq t_i^*$. In the mean time, $\|\mathbf{e}(t)\| \geq \rho$ for $t_i \leq t \leq t_i^*$ is automatically assumed here since it is the only case of interest. Consequently, Eq.(5.23) holds with $t = t_i^*$. This, together with Eq.(5.24) gives us

$$t_i^* - t_i \leq \frac{1}{M_m}\left(\sqrt{\frac{\rho}{2\|\mathbf{P}\|M_1}} - \phi - \rho - \delta\right). \tag{E.11}$$

Besides, it can be concluded from Eq.(5.21) that

$$\|\mathbf{e}(t_i^*)\| \leq \left(\frac{\lambda_{max}[\mathbf{P}]}{\lambda_{min}[\mathbf{P}]}\rho^2 + \frac{N_0 + N_1}{\gamma\lambda_{min}[\mathbf{P}]}\right)^{\frac{1}{2}} = \phi. \tag{E.12}$$

By the use of Eqs.(E.1), (E.11) and (E.12), $\|\mathbf{x}(t_i^*) - \mathbf{x}_i\|(= \|\mathbf{x}(t_i^*) - \mathbf{x}(t_i)\|)$ can be bounded as follows

$$\begin{aligned}
\|\mathbf{x}(t_i^*) - \mathbf{x}_i\| &\leq \|\mathbf{e}(t_i^*)\| + \|\mathbf{x}_m(t_i^*) - \mathbf{x}_m(t_i)\| + \|\mathbf{e}(t_i)\| \\
&\leq \phi + M_m(t - t_i) + \rho \leq \sqrt{\frac{\rho}{2\|\mathbf{P}\|M_1}} - \delta \\
&< \sqrt{\frac{\rho}{2\|\mathbf{P}\|M_1}} = \sqrt{\frac{2\epsilon}{M}}.
\end{aligned} \tag{E.13}$$

Applying this result to Eq.(5.3) with $p = 1$, obviously we have $d(t_i^*) < \epsilon$ which is contradictory to the statement that $d(t_i^*) = \epsilon$. Therefore, such a t_i' does not exist for $\|\mathbf{e}\| \geq \rho$. This completes the proof. □

Appendix F

Control Software for Thrust and Radial Bearings

Control programs for the axial bearing and the radial bearings share similar structure. The flow chart of the programs is shown in Figure F.1. Take "axialctr.asm" for example, the program start with including header files and defining control parameters. The header file "defebara.h" contains the definitions for the A/D offsets, the D/A offsets, some A/D constants and some D/A constants. The header file " defmacro.h" defines some macros such as DIV (for division), STARTCONV (for starting conversion) and DATACONV (to convert the data into DSP readable format). After these definitions, the program allocate data memory space for storging control variables. These control variables are then initialized properly. In the main control loop, the rotor position is sampled and the rotor velocity is calculated using the backward diffference method. Since the presence of noise is innevitable, the velocity is further filtered. Afterwards, the reference position and velocity together with the position error and velocity error are computed using the discrete version of Eq.(7.5). In order to determine when to turn on and off the adaptation, we calculate the value of a flag. The flag value, which is set to 0 initially, equals 1 when the $\|\mathbf{e}\|_\infty$ exceeds $\rho+\sigma$, equals 2 when $\|\mathbf{e}\|_\infty$ is less than $\rho-\sigma$. If $\|\mathbf{e}\|_\infty$ is between $\rho+\sigma$ and $\rho-\sigma$, then the current flag value is equal to the flag value of the last sampling period. Notice that for the purpose of saving computation time, the infinity norm instead of Euclidian norm is used here. Finally, the control effort which consists of PD term and adaptation term

is computed and is sent to the D/A.

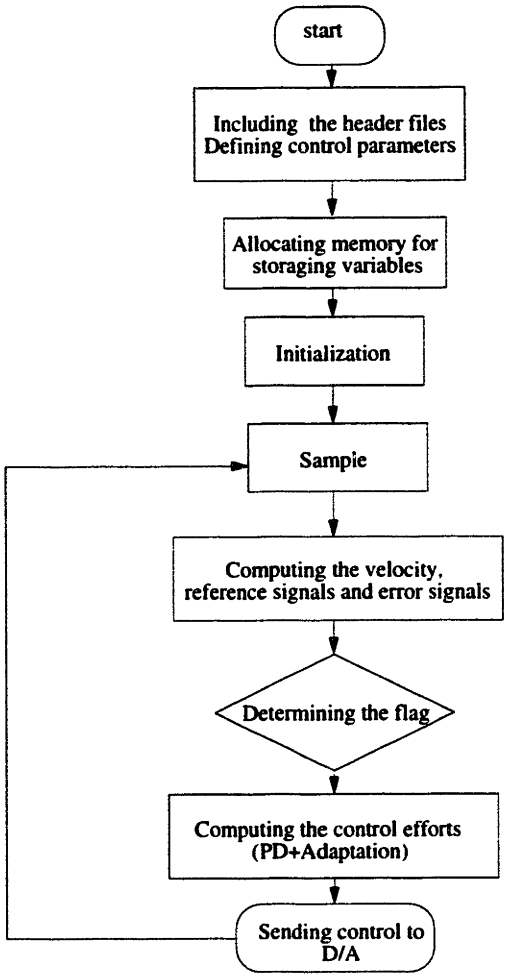

Figure F.1: Flow chart for the control software

F.1 Header Files for the Control Software

A. "defebara.h"

```
{------------------------------------------------------------------------}
{                              - defebara.h -                            }
{This file includes status register bit definitions and hardware parameters }
{for the DSP board used in EBARA project.                                }
{------------------------------------------------------------------------}

{Status register bit definitions}
{------------------------------------------------------------------------}
{------------------------------------------------------------------------}

 {MODE1 register}

#define IRPTEN  0x00001000

 {MODE2 register}
#define TIMEN  0x00000020
#define FG2OUTPUT 0x00020000

 {ASTAT register}




 {STKY register}

 {IRPTL and IMASK and IMASKP register}
#define TMZHI   0x00000010


{Hardware parameters}
{------------------------------------------------------------------------}
{------------------------------------------------------------------------}
 {CPU speed}
#define CPUSPEED  33333333.333



 {A/D offset value}
#define AD0OFFSET  0x00000906
#define AD1OFFSET  0x000008E6
#define AD2OFFSET  0x00000905
```

```
#define AD3OFFSET  0x00000904
#define AD4OFFSET  0x000008DB
#define AD5OFFSET  0x000008E4
#define AD6OFFSET  0x00000926


{D/A offset value}
{#define DA0OFFSET  42.0}
{#define DA1OFFSET  -28.0}

#define DA0OFFSET  0xFFFFFFF2
#define DA1OFFSET  0x0000000C
#define DA2OFFSET  0x0FFFFFF1
#define DA3OFFSET  0xFFFFFFFE
#define DA4OFFSET  0xFFFFFFFF


{ D/A constants                                                    }
#define DAVOLTSMAX   5.0
#define DAVOLTSMIN  -5.0
#define DABITSMAX   8192.0

{ A/D constants                                                    }
#define ADVOLTSMAX   5.0
#define ADVOLTSMIN  -5.0
#define ADBITSMAX   8192.0
```

B. "defmacro.h"

```
{------------------------------------------------------------------------}
{                              - defmacro.h -                             }
{This file includes the macros used in the EBARA project                  }
{------------------------------------------------------------------------}


{ Toggle FLAG2 to signal I/O board to start conversion                    }

#define STARTCONV       BIT SET ASTAT 0x00200000;\
                        NOP; NOP; NOP;\
                        BIT CLR ASTAT 0x00200000;\
                        NOP; NOP; NOP
```

```
#define startconv       BIT SET ASTAT 0x00200000;\
                        NOP; NOP; NOP;\
                        BIT CLR ASTAT 0x00200000;\
                        NOP; NOP; NOP


{ division macro - if there is a quicker way, just change macro }
{                  macro requires the following:                }
{                  F0  = numerator                              }
{                  F12 = denominator                            }

{--------------------------------------------------------------------}
{ Division Algorithm - Given Q = D/N, multiply N and D by the same set }
{                      of factors, Rn.                               }
{      N x R0 x R1 x ... x Rn                                        }
{  Q = ----------------------                                        }
{      D x R0 x R1 x ... x Rn                                        }
{                                                                    }
{ Choose Rn such that as the number of factors increases, the        }
{ denominator approaches 1.  The quotient is then approximately equal }
{ to the numerator.                                                  }
{                                                                    }
{ R0 is the seed provided by the RECIPS instruction.  Succssive Rn are }
{ calculated by the following formula:                               }
{  Ri = 2-D(i-1)                                                     }
{                                                                    }
{ NOTE:  The macro uses the following registers:                     }
{        F0, F7, F11, F12                                            }
{        These registers will be over-written upon exit from macro.  }
{--------------------------------------------------------------------}

#define div     F11 = 2.0; \
                F0 = RECIPS F12, F7 = F0; \
                F12 = F0*F12; \
                F7 = F0*F7, F0 = F11-F12; \
                F12 = F0*F12; \
                F7 = F0*F7, F0 = F11-F12; \
                F12 = F0*F12; \
                F7 = F0*F7, F0 = F11-F12; \
                F0 = F0*F7

#define DIV     F11 = 2.0; \
                F0 = RECIPS F12, F7 = F0; \
                F12 = F0*F12; \
```

```
                F7 = F0*F7, F0 = F11-F12; \
                F12 = F0*F12; \
                F7 = F0*F7, F0 = F11-F12; \
                F12 = F0*F12; \
                F7 = F0*F7, F0 = F11-F12; \
                F0 = F0*F7

{ Convert the bit information from DSP to D/A                                  }
{ F0 = the output (in volts OR AMPS OR METERS) of DSP;                         }
{ F1 = VOLTS2BITS (OR AMPS TO BITS OR METERS TO BITS); F2 = DABITSMAX;         }
{ R0 = final bits in DA, F3 = offset in DA                                     }

#define DACONV    F0 = F1*F0;\
                  F0 = F3+F0;\
                  F1 = F0+F2;\
                  R0 = FIX F1;\
                  R0 = ASHIFT R0 BY 2

#define daconv    F0 = F1*F0;\
                  F0 = F3+F0;\
                  F1 = F0+F2;\
                  R0 = FIX F1;\
                  R0 = ASHIFT R0 BY 2
```

F.2 Control Program for the Thrust Bearing

```
{ Axialctr.asm: The assembly program for controlling the axial bearing }

 #include "defebara.h"
{The header file defebara.h defines the A/D offsets,  D/A offsets, A/D
constants, D/A constants}
 #include "defmacro.h"
{The header file defmacro.h defines some macros such as  div , startconv
 and dataconv}


 #define NUMOFCHANNEL 1   {number of channel}
 #define SMPLSPEED 20000.0   {sampling rate = 20k Hz }
 #define SAVEOFFSET  256       {parameter for saving the data }


{Define some control parameters                                    }

 #define REF_NATFREQ  600.0   {reference model banwidth = 600 rad/s)
 #define REF_DAMP     1.0           {reference model damping = 1.0   }
 #define AXL_B        49.68 {VOLTS TO NEWTONS, equivalent to
 b_{z}=11.5N/A*4.32 A/V}
 #define AXL_SENGAIN  9450.0   {METERS TO VOLTS, the sensor gain}
 #define AXL_INITSIG  -0.3189    {VOLTS,  the initial control current ----
corresponding to   2.2KG, }
 #define AXL_MAXU     1.08    {VOLTS,  the maximum control current---
corresponding to 4 AMPS}
 #define HYSTERESIS   0.0000005 {METERS, the thichness of hysteresis loop}
 #define ADAPTATION   1.0e13        {no unit, adaptation gain}

 #define C1           0.8187307531 {EXP^-ALPHA*T, ALPHA=FILTER
BANDWIDTH , a parameter of the first order filter for the velocity signal,
filter  bandwidth =1kHz}
  #define C2           0.1812692469 {a parameter of the first order filter
for the velocity signal, filter bandwidth =1kHz}

{vf(k+1)=C1*vf(k)+C2*v(k)           vf : filter velocity, v: raw velocity}

  { The following ports are found on the ADSP board              }

  .SEGMENT /DM status;
  .VAR DSPSTAT; {DSP status register}
  .ENDSEG;
```

```
.SEGMENT /DM timer;
.VAR DSPTIMER; {DSP timer}
.ENDSEG;

{ The following ports are found on the 32-channel ADC board     }

.SEGMENT /PM ioadin;
.VAR ADFIFO; {A/D fifo }
.ENDSEG;

.SEGMENT /PM iostat;
.VAR IOSTAT;  {input-output status }
.ENDSEG;

.SEGMENT /DM iodaout;
.VAR DAFIFO;  {D/A fifo }
.ENDSEG;

.SEGMENT /DM iochans;
.VAR CHANNELS; {input-output channel }
.ENDSEG;

.SEGMENT /DM iocntrl;
.VAR CONTROL; { control register }
.ENDSEG;




.SEGMENT /DM dm_data;
{ Conversion factors                                                    }
.VAR VOLT2BITS; {bits/volt }
.VAR BITS2VOLT;  {volts/bit }


{-----------------------------Define variables-------------------------}
.VAR ADINPUT;  {the A/D input}
.VAR DACONTROL; {the D/A control signal}
.VAR SMPL_PERIOD; {sampling period}

 {variables for the reference model}
.VAR REF_POS0;
.VAR REF_VEL0;
.VAR REF_POS;
.VAR REF_VEL;
```

```
 { variables for the plant,}
.VAR AXL_X0;  {old position}
.VAR AXL_X1;   {new position}
.VAR AXL_V1;   {new velocity}
.VAR AXL_V0;   {old velocity}

 { error signal}
.VAR ERR_X;   {position error}
.VAR ERR_V;    {velocity error}

.VAR AXL_BINV; {1/b_{z}}
.VAR AXL_CONV1; { a conversion factor}

 {parameters used in the reference model A matrix}
.VAR REF_AT12;
.VAR REF_AT21;
.VAR REF_AT22;


.VAR P_GAIN; {p gain}
.VAR D_GAIN; {d gain}
.VAR NRML_FCTR; { normalizing factor }
.VAR FLAG; { the flag for the deadzone+ hysteresis loop }

.VAR ADAPT_X;  {position gain used in computing the adapation signal}
.VAR ADAPT_V;   {velocity gain used in computing the adapation signal}

.VAR ADAPT_U;   {the adaptation signal }

{ Variables needed to save data in memory for later dumping }
.VAR INPUT_OFFSET;
.VAR OUTPUT_OFFSET;
.VAR SAVE_END;


.ENDSEG;

.SEGMENT /PM rst_svc;

{-------------------------------------------------------------------}
{ At reset, the BANK registers are as follows:                      }
{       PMBANK1 = 0x800000                                          }
{       DMBANK1 = 0x20000000                                        }
{       DMBANK2 = 0x40000000                                        }
```

```
{       DMBANK3 = 0x80000000                                                }
{ These values, by coincidence, are perfect for our I/O board               }
{---------------------------------------------------------------------------}

{---------------------------------------------------------------------------}
{ The default value of PMWAIT at reset is 0x0003DE.  This corresponds       }
{ to the following:                                                         }
{       bit  13    = 0   (No automatic wait state)                          }
{       bits 12-10 = 000 (memory page size = 256 words)                     }
{       bits  9-7  = 111 (7 PMBANK1 wait states)                            }
{       bits  6-5  = 10  (Int. and Ext. wait state ack mode)                }
{       bits  4-2  = 111 (7 PMBANK0 wait states)                            }
{       bits  1-0  = 10  (Int. and Ext. wait state ack mode)                }
{                                                                           }
{ For our setup, the DSP board accesses memory at 0 wait states and         }
{ accesses all ports and 1 wait state.  Therefore:                          }
{       bit  13    = 0   (No automatic wait state)                          }
{       bits 12-10 = 100 (memory page size = 4096 words)                    }
{       bits  9-7  = 001 (1 PMBANK1 wait state)                             }
{       bits  6-5  = 10  (Int. and Ext. wait state ack mode)                }
{       bits  4-2  = 000 (0 PMBANK0 wait states)                            }
{       bits  1-0  = 10  (Int. and Ext. wait state ack mode)                }
{---------------------------------------------------------------------------}

 PMWAIT = 0x0010C2;

{---------------------------------------------------------------------------}
{ The default value of DMWAIT at reset is 0x000F7BDE.  This corresponds     }
{ to the following:                                                         }
{       bit  23    = 0   (No automatic wait state)                          }
{       bits 22-20 = 000 (memory page size = 256 words)                     }
{       bits 19-17 = 111 (7 DMBANK3 wait states)                            }
{       bits 16-15 = 10  (Int. and Ext. wait state ack mode)                }
{       bits 14-12 = 111 (7 DMBANK2 wait states)                            }
{       bits 11-10 = 10  (Int. and Ext. wait state ack mode)                }
{       bits  9-7  = 111 (7 DMBANK1 wait states)                            }
{       bits  6-5  = 10  (Int. and Ext. wait state ack mode)                }
{       bits  4-2  = 111 (7 DMBANK0 wait states)                            }
{       bits  1-0  = 10  (Int. and Ext. wait state ack mode)                }
{                                                                           }
{ For our setup, the DSP board accesses memory at 0 wait states and         }
{ accesses all ports and 1 wait state.  Therefore:                          }
{       bit  23    = 0   (No automatic wait state)                          }
{       bits 22-20 = 100 (memory page size = 4096 words)                    }
{       bits 19-17 = 001 (1 DMBANK3 wait states)                            }
```

```
{       bits 16-15 = 10  (Int. and Ext. wait state ack mode)           }
{       bits 14-12 = 001 (1 DMBANK2 wait states)                       }
{       bits 11-10 = 10  (Int. and Ext. wait state ack mode)           }
{       bits  9-7  = 000 (0 DMBANK1 wait state)                        }
{       bits  6-5  = 10  (Int. and Ext. wait state ack mode)           }
{       bits  4-2  = 000 (0 DMBANK0 wait states)                       }
{       bits  1-0  = 10  (Int. and Ext. wait state ack mode)           }
{-------------------------------------------------------------------------}

 DMWAIT = 0x00431842;

{-------------------------------------------------------------------------}
{ Set FLAG2 to output mode so we can trigger I/O board conversion when  }
{ we need to.                                                           }
{-------------------------------------------------------------------------}

 MODE2 = FG2OUTPUT;


 JUMP initialize;
.ENDSEG;


.SEGMENT /PM pm_code;

initialize:

{ initialize registers }

 IMASK = 0;
 MODE1 = 0x00012000;

 I0 = 0;
 I1 = 0;
 I2 = 0;
 I3 = 0;
 I4 = 0;
 I5 = 0;
 I6 = 0;
 I7 = 0;
 M0 = 0;
 M1 = 0;
 M2 = 0;
 M3 = 0;
 M4 = 0;
```

```
 M5 = 0;
 M6 = 0;
 M7 = 0;
 L0 = 0;
 L1 = 0;
 L2 = 0;
 L3 = 0;
 L4 = 0;
 L5 = 0;
 L6 = 0;
 L7 = 0;
{-------------------------------------------------------------------------}
{ This program does the following:                                        }
{       1.  Triggers A/D conversion on one channel                        }
{       2.  Polls A/D status register to see when conversion complete     }
{       3.  Pushes A/D value out to D/A                                   }
{       4.  returns to step 1                                             }
{-------------------------------------------------------------------------}

{ Make sure FLAG2 toggle is initially zero.                               }
 BIT CLR ASTAT 0x00200000;

{ Calculate D/A conversion factor                                         }
 F0 = DABITSMAX;
 F12 = DAVOLTSMAX;
 DIV;
 DM(VOLT2BITS) = F0;

{ Calculate A/D conversion factor                                         }
 F12 = ADBITSMAX;
 F0 = ADVOLTSMAX;
 DIV;
 DM(BITS2VOLT) = F0;

{ Initialize the control signal to zero }

 R3 = DA0OFFSET;
 F3 = FLOAT R3;
 F1 = DM(VOLT2BITS);
 F2 = DABITSMAX;
 F0 = 0.0;
 DACONV;
 DM(DACONTROL) = R0;
```

```
{ Set up axial bearing conversion factor for A/D        }
{ axl_conv1=bits2volt/axl_sengain                              }
{ axl_sengain-position sensor conversion factor         }
 F0 = DM(BITS2VOLT);  {1 bit = ? volts   }
 F12 = AXL_SENGAIN;   {1 meters =? volts }

 DIV;

 DM(AXL_CONV1) = F0;       {1 bit = ? meters}



{ Set up the sampling time   T  }
 F0 = 1.0;
 F12 =SMPLSPEED;

 DIV;

 DM(SMPL_PERIOD) = F0;

{ Set up axial bearing 1*PERIOD constant      1/(T)          }
 F0 = SMPLSPEED;
 F12 = 1.0;

 DIV;

 DM(AXL_PERIOD) = F0;

{ Set up normalizing constant      1/omega          }
 F0 = 1.0;
 F12 = REF_NATFREQ;

 DIV;

 DM(NRML_FCTR) = F0;

{ Set up adaptation constants}
 F0 = REF_NATFREQ;
 F1 = F0;
 F0 = F1*F0;
 F1 = 4.4;
 F12 = F1*F0;

 F0 = ADAPTATION;
```

```
   DIV;

   F0 = -F0;
   F1 = DM(SMPL_PERIOD);
   F0 = F1*F0;
   DM(ADAPT_X) = F0;

   F12 = REF_NATFREQ;
   F1 = REF_DAMP;
   F12 = F1*F12;

   DIV;

   DM(ADAPT_V) = F0;

{ In this case, a_{0}(k+1)=a_{0}(k)+ADAPT_X*ERR_X+ADAPT_V*ERR_V,
the discrete version of Eq. (7.9). Because in simulations, the adaption effort
due to a_{1} in Eq. (7.9) is insignificant compared that due to a_{0}, to save
the computation time, the zeroth order approximation is implementedt}


  { Set up AXL_BINV (1/b) constant                                    }
   F0 = 1.0;
   F12 = AXL_B;

   DIV;

   DM(AXL_BINV) = F0;


  {Set up the reference model A*T matrix constants                 }
  { For the reference model, xm(k+1)=(I+A*T)*xm(k)          }

   F0 = DM(SMPL_PERIOD);

   DM(REF_AT12) = F0;

   F0 = REF_NATFREQ;
   F1 = F0;
   F2 = DM(SMPL_PERIOD);

   F3 = F0*F1;

   F0 = -1.0;
```

```
F3 = F0*F3;
DM(P_GAIN) = F3;
F3 = F3*F2;

DM(REF_AT21) = F3;

F0 = -2.0;
F1 = REF_DAMP;
F2 = REF_NATFREQ;
F3 = DM(SMPL_PERIOD);

F4 = F0*F1;
F4 = F4*F2;
DM(D_GAIN) = F4;
F4 = F4*F3;

DM(REF_AT22) = F4;


{ Setup the initial velocity for the reference model                }
{ The initial position will be acquired by  the sampling process    }
{ Also initialize the flag and adaptation control signal            }
F0 = 0.0;

DM(REF_VEL0) = F0;
DM(AXL_V0) = F0;
DM(FLAG) = F0;
DM(ADAPT_U) = F0;
{ Setup variables required to saving data in memory for later recall    }
R0 = SAVEOFFSET;
DM(INPUT_OFFSET) = R0;
R1 = ASHIFT R0 BY 1;
R2 = 0x8000;
R2 = R2-R1;
R2 = ASHIFT R2 BY -1;
R1 = R2+R0;
DM(OUTPUT_OFFSET) = R1;
R1 = R1+R2;
DM(SAVE_END) = R1;

{ Reset I/O board                                                   }
R0 = 0x0;
DM(CONTROL) = R0;
NOP; NOP; NOP;
```

```
{-------------------------------------------------------------------------}
{ Set 1 A/D channel and 0 D/A channels.  When a conversion is triggered,}
{ both the A/D and D/A conversions are triggered.  Therefore, I set the }
{ the number of D/A to 0 so that nothing goes out.                       }
{                                                                        }
{ Number of Channels Register:  [default - DM(0x40000001)]               }
{       bits 2-0 -> number of A/D channels                               }
{       bits 5-3 -> number of D/A channels                               }
{-------------------------------------------------------------------------}

 R0 = NUMOFCHANNEL;
 R1 = LSHIFT R0 BY 3;
 R0 = R0+R1;
 DM(CHANNELS) = R0;
 NOP; NOP; NOP;

{-------------------------------------------------------------------------}
{ Release analog reset (don't know why) and set go mode to flag2 toggle }
{                                                                        }
{ Control Register:  [default - DM(0x40000002)]                          }
{       bits 2-0 -> go mode (0 = go on toggle of FLAG2)                  }
{                           (1 = go on interrupt)                        }
{       bits 5-3 -> IRQ mode                                             }
{       bit    6 -> Status select                                        }
{       bit    7 -> Analog reset                                         }
{-------------------------------------------------------------------------}

 R0 = 0x80;
 DM(CONTROL) = R0;
 NOP; NOP; NOP;



{ Set timer sampling period and counter                                  }

 F12 = SMPLSPEED;
 F0 = CPUSPEED;
 DIV;
 R1 = FIX F0;
 R0 = R1-1;

 TPERIOD = R0;
 TCOUNT = R0;

{Set the initial current}
```

```
 F0 = AXL_INITSIG;
 F2 = AXL_MAXU;

{Make the control current does not exceed the limit  }

 COMP(F0,F2);
 IF GT F0=F2;
 F2=-F2;
 COMP(F0,F2);
 IF LT F0=F2;

 F1 = DM(VOLT2BITS);
 F2 = DABITSMAX;
 R3 = DAOOFFSET;
 F3 = FLOAT R3;
 DACONV;

 DM(DACONTROL)=R0;

{Send the initial current and get the initial position information        }


 DM(DAFIFO) = R0;

 STARTCONV;


 R1 = 0x03;
wait_init:      R0 = PM(IOSTAT);
 R7 = R0 AND R1;
 IF NE JUMP wait_init;




{-------------------------------------------------------------------------}
{ Get A/D value(s) from FIFO.  [default - PM(0x800000)]                    }
{                                                                          }
{ The values obtained are 14-bit 2^s-complement values sign extended to }
{ the left.  2^s complement is obtained by negating the real value and  }
{ adding 1.  The range of values for our particular A/D is:              }
{                                                                          }
{       +5V = 0001 1111 1111 1111                                          }
{        0V = 0000 0000 0000 0000                                          }
```

```
{       -5V = 1110 0000 0000 0001                                          }
{                                                                          }
{ Sample code for converting 2^s complement notation to floating point    }
{ is as follows:                                                           }
{               R1 = FEXT R0 BY 0:16 (SE);                                 }
{               F0 = FLOAT R0;                                             }
{                                                                          }
{ Sample code for converting floatin point numbers to 2^s complement       }
{ notation is as follows:                                                  }
{               F0 = FIX R0;                                               }
{                                                                          }
{------------------------------------------------------------------------}

{Read and discard the A/D value}

 R0 = PM(ADFIFO);

{Resend the control signal }
 R0 = DM(DACONTROL);
 DM(DAFIFO) = R0;

 STARTCONV;


 R1 = 0x03;
wait_init1:     R0 = PM(IOSTAT);
 R7 = R0 AND R1;
 IF NE JUMP wait_init1;


{ Convert the A/D value to meters  }
 R0 = PM(ADFIFO);
 R0 = FEXT R0 BY 0:14 (SE);
 DM(ADINPUT) = R0;
 R1 = ADOOFFSET;
 R0 = R0+R1;
 F0 = FLOAT R0;
 F1 =  DM(AXL_CONV1);
 F0 = F0*F1;


{ Store the initial position                                               }
 DM(REF_POS0) = F0;
 DM(AXL_X0) = F0;
 DM(AXL_X1) = F0;
```

```
{ Set up input/output save pointers in last address registers          }
 I6 = DM(INPUT_OFFSET);
 I7 = DM(OUTPUT_OFFSET);

{Save the first A/D input(sensor output), D/A output(control input data)}
#ifdef PLOT

 R0 = DM(ADINPUT);
 DM(I6,1) = R0;
 R0 = DM(DACONTROL);
 F3 = DABITSMAX;
 R3 = FIX F3;
 R0 = FEXT R0 BY 2:14;
 R0 = R0-R3;
 DM(I7,1) = R0;

#endif
#ifdef plot

 R0 = DM(ADINPUT);
 DM(I6,1) = R0;
 R0 = DM(DACONTROL);
 F3 = DABITSMAX;
 R3 = FIX F3;
 R0 = FEXT R0 BY 2:14;
 R0 = R0-R3;
 DM(I7,1) = R0;

#endif

{ Reset interrupt latch register                                       }
 BIT SET IRPTL 0x0;

{ Allow timer interrupts                                               }
 BIT SET IMASK TMZHI;

{ Turn on timer                                                        }
 BIT SET MODE2 TIMEN;

{ Allow interrupt generation                                           }
 BIT SET MODE1 IRPTEN;

idlecycle:      IDLE;
```

```
 JUMP idlecycle;

{The control code starts here}
sample:

 R0 = DM(DACONTROL);
 DM(DAFIFO) = R0;

 STARTCONV; { Start  A/D conversion after sampling}


 R1 = 0x03;

                    {Wait until the conversion is done}
wait1:          R0 = PM(IOSTAT);
 R7 = R0 AND R1;
 IF NE JUMP wait1;




{-------------------------------------------------------------------------}
{ Get A/D value(s) from FIFO.  [default - PM(0x800000)]                   }
{                                                                         }
{ The values obtained are 14-bit 2's-complement values sign extended to }
{ the left.  2's complement is obtained by negating the real value and  }
{ adding 1.  The range of values for our particular A/D is:               }
{                                                                         }
{       +5V = 0001 1111 1111 1111                                         }
{        0V = 0000 0000 0000 0000                                         }
{       -5V = 1110 0000 0000 0001                                         }
{                                                                         }
{ Sample code for converting 2's complement notation to floating point  }
{ is as follows:                                                          }
{               R1 = FEXT R0 BY 0:16 (SE);                                }
{               F0 = FLOAT R0;                                            }
{                                                                         }
{ Sample code for converting floatin point numbers to 2's complement    }
{ notation is as follows:                                                 }
{               F0 = FIX R0;                                              }
{                                                                         }
{-------------------------------------------------------------------------}

 R0 = PM(ADFIFO);
```

```
{ Transform the sampling data into right format----- adding offset,
 multiplying the conversion factor}
   R0 = FEXT R0 BY 0:14 (SE);
   DM(ADINPUT) = R0;
   R1 = ADOOFFSET;
   R0 = R0+R1;
   F0 = FLOAT R0;
   F1 = DM(AXL_CONV1);
   F0 = F0*F1;

  {Store the position signal as AXL_X0}

   DM(AXL_X0) = F0;
 {Determine RAW velocity using backward difference }

   F1 = DM(AXL_X1);
   F0 = F0-F1;

   F1 = DM(AXL_PERIOD);

   F0 = F0*F1;

 {Pass the velocity signal through a filter   }
 {vf(k+1)=C1*vf(k)+C2*v(k)            vf : filter velocity, v: raw velocity}
   F1 = C2;
   F0 = F0 *F1;

   F1 = C1;
   F2 = DM(AXL_V1);
   F2 = F1*F2;

   F0 = F0 +F2;

   DM(AXL_V0) = F0;

{The filtered velocity is now saved in AXL_V0                    }

{-------------------------------------------------------------------------}
{-------------------------------------------------------------------------}


{Compute the reference signals ( position and velocity) and the error signals
 position and velocity)}
   F0 = DM(REF_AT12);
   F1 = DM(REF_VEL0);
```

```
  F2 = F0*F1;
  F0 = DM(REF_POS0);
  F2 = F2+F0;
  DM(REF_POS) = F2;
  F1 = DM(AXL_X0);
  F1 = F1-F2;
  DM(ERR_X)=F1;

  F0 = DM(REF_AT21);
  F1 = DM(REF_POS0);
  F2 = F0*F1;
  F0 = DM(REF_AT22);
  F1 = DM(REF_VEL0);
  F3 = F0*F1;
  F2 = F2+F3;
  F0 = DM(REF_VEL0);
  F2 = F0+F2;
  DM(REF_VEL) = F2;
  F1 = DM(AXL_V0);
  F1 = F1-F2;
  DM(ERR_V)=F1;

{Determine the flag value, the flag is initially 0,   }

  F3 = DM(FLAG);

  F0 = DM(ERR_X);
  F0 = ABS F0;

  F1 = DM(ERR_V);
  F1 = ABS F1;
  F2 = DM(NRML_FCTR);
  F1 =F1*F2;

  F2 = MAX(F0,F1); {Determine the max norm}
  F4 = HYSTERESIS;

  COMP(F2,F4);
  IF LE JUMP setflag0;

  F1 = 1.41421;
  F4 = F1*F4;

  COMP(F2,F4);
  IF GT JUMP setflag1;
```

```
 JUMP setflag;

setflag0:       F3 = 0.0;
 JUMP setflag;

setflag1:       F3 = 1.0;
 JUMP setflag;

setflag:        DM(FLAG) = F3;

{Determine the adaptive control action }
 F0 = DM(ERR_X);
 F1 = DM(ADAPT_X);
 F0 = F0*F1;

 F1 = DM(ERR_V);
 F2 = DM(ADAPT_V);
 F1 = F1*F2;

 F3 = F0+F1;
 F4 = DM(FLAG);
 F3 = F3*F4;
 F5 = DM(ADAPT_U);
 F5 = F3+F5; {Adaptive control action}
 DM(ADAPT_U) = F5;

{Determine the PD control action }
 F0 = DM(P_GAIN);
 F1 = DM(AXL_X0);
 F2 = F0*F1;
 F0 = DM(D_GAIN);
 F1 = DM(AXL_V0);
 F3 = F0*F1;
 F2 = F2+F3;  {PD control force}
 F2 = F2+F5;  {PD +Adaptive control}
 F0 = DM(AXL_BINV);
 F2 = F2*F0;
 F1 = AXL_INITSIG;
 F0 = F1+F2; {Total volts}

{Check if any saturation occurs in the control current}

 F2 = AXL_MAXU;

 COMP(F0,F2);
```

```
 IF GT F0=F2;
 F2=-F2;
 COMP(F0,F2);
 IF LT F0=F2;

 F1 = DM(VOLT2BITS);
 F2 = DABITSMAX;
 R3 = DAOOFFSET;
 F3 = FLOAT R3;
 DACONV;

 DM(DACONTROL)=R0;

 DM(DAFIFO) = R0;



 STARTCONV;

 R1 = 0x03;
wait2:          R0 = PM(IOSTAT);
 R7 = R0 AND R1;
 IF NE JUMP wait2;



{Save the reference position, velocity       }

 F0 = DM(REF_POS);
 DM(REF_POS0) = F0;
 F0 = DM(REF_VEL);
 DM(REF_VEL0) = F0;

{Update system position information }


 F0 = DM(AXL_X0);
 DM(AXL_X1) = F0;

 F0 = DM(AXL_V0);
 DM(AXL_V1) = F0;


{ Save original input value before we over-write it                    }
```

```
#ifdef PLOT
 R0 = I6;
 R1 = DM(OUTPUT_OFFSET);
 R0 = R1-R0;
 IF EQ JUMP sskip;

 R0 = DM(ADINPUT);
 DM(I6,1) = R0;
 R0 = I7;
 R1 = DM(SAVE_END);
 R0 = R1-R0;
 IF EQ JUMP sskip;

 R0 = DM(DACONTROL);
 F3 = DABITSMAX;
 R3 = FIX F3;
 R0 = FEXT R0 BY 2:14;
 R0 = R0-R3;
 DM(I7,1) = R0;

#endif

#ifdef plot
 R0 = I6;
 R1 = DM(OUTPUT_OFFSET);
 R0 = R1-R0;
 IF EQ JUMP sskip;

 R0 = DM(ADINPUT);
 DM(I6,1) = R0;
 R0 = I7;
 R1 = DM(SAVE_END);
 R0 = R1-R0;
 IF EQ JUMP sskip;

 R0 = DM(DACONTROL);
 F3 = DABITSMAX;
 R3 = FIX F3;
 R0 = FEXT R0 BY 2:14;
 R0 = R0-R3;
 DM(I7,1) = R0;

#endif
```

```
sskip:          R0 = PM(ADFIFO);



ret:
 RTI;

.ENDSEG;


.SEGMENT /PM tmzh_svc;

 JUMP sample;

.ENDSEG;
```

F.3 Control Program for the Radial Bearings

```
{ Radctr.asm: the assembly program for controlling the radial bearing  system}


{-------------------------------------------------------------------------}
 #include "defebar1.h"
{The header file defebara.h defines the A/D offsets,  D/A offsets, A/D
constants, D/A constants}

 #include "defmacro.h"
{The header file defmacro.h defines some macros such as  div , startconv
and dataconv}

 #define NUMOFCHANNEL 4  {number of channel}
 #define SMPLSPEED 15000.0  {sampling rate = 20k Hz }
 #define SAVEOFFSET  256  parameter for saving the data }

 {Define some control parameters                                    }
 #define REF1_NATFREQ  550.0  {reference model bandwidth for 1 axis=550
   rad/s}
 #define REF2_NATFREQ  770.0  {reference model bandwidth for 1 axis=770
   rad/s}

 #define REF_DAMP     1.0 {reference model damping ratio}
 #define RAD_B1       22.6 {X1 VOLTS TO NEWTONS, b_{x1}=22.6 N/V}
 #define RAD_B2       35.1 {X2 VOLTS TO NEWTONS, b_{x2}=35.1 N/V}
 #define RAD_B3       28.1 {Y1 VOLTS TO NEWTONS, b_{y1}=28.1 N/V}
 #define RAD_B4       39.1 {Y2 VOLTS TO NEWTONS, b_{y2}=39.1 N/V}
 #define RAD_SEN      25000.0   {METERS TO VOLTS, the sensor gain}
 #define RAD_MAXU     1.47   {VOLTS,  the maximum control current---
   corresponding to 3.5AMPS}
 #define HYSTERESIS   0.25e-6  {METERS, the width of hysteresis loop}
 #define ADAPTATION1   7.0e13        {no unit, adaptation gain for 1 axis}
 #define ADAPTATION2   14.0e13      {no unit, adaptation gain for 2 axis}

{Define filter parameters for the velocity signal}
{vf(k+1)=C1*vf(k)+C2*v(k)            vf : filter velocity, v: raw velocity}

 #define C1           0.8187307531    {EXP^-ALPHA*T, ALPHA=FILTER
   BANDWIDTH , a parameter of the first order filter for the velocity signal,
   filter bandwidth =1kHz}
 #define C2           0.1812692469    {1-c1} {a parameter of the first order
  filter for the velocity signal, filter bandwidth =1kHz}
```

```
#define ALPHA         0.5229147967  {1/M+L1^2/Ir}
#define BETA          0.2560445493  {1/M-L1*L2/Ir}
#define GAMMA         1.0308653097  {1/M+L2^2/Ir}

#define ALPHAINV      2.1771366598
#define BETAINV       -0.54075345203
#define GAMMAINV      1.104370244287
{  | ALPHAINV ,  BETAINV       | --| ALPHA ,  BETA    | -1
     | BETAINV    ,  GAMMAINV | --| BETA   ,  GAMMA|          }


{ Notice that the equations of motion for the radial bearings are
   ddot x1= f1(x1,x2,doty1,doty2)+ALPHA*Fx1+BETA*Fx2;
   ddot x2= f2(x1,x2,doty1,doty2)+BETA*Fx1+GAMMA*Fx2;
   ddot y1= f3(dotx1,dotx2,y1,y2)+ALPHA*Fy1+BETA*Fy2;
   ddot y2= f4(dotx1,dotx2,y1,y2)+BETA*Fy1+GAMMA*Fy2;

   where the f1,f2,f3,f4 are the nonlinear, uncertain funtions due to the
   magnetic field and the gyroscopic effect, Fx1=b_{x1}*ux1, Fx2=b_{x2}*ux2,
   Fy1=b_{y1}*uy1 and Fy2=b_{y2}*uy2 are the magnetic forces.
   (ux1,ux2,uy1,uy2 are the control voltages)}


 { The following ports are found on the ADSP board              }

 .SEGMENT /DM status;
 .VAR DSPSTAT; {DSP status register}
 .ENDSEG;

 .SEGMENT /DM timer;
 .VAR DSPTIMER; {DSP timer}
 .ENDSEG;

 { The following ports are found on the 32-channel ADC board    }

 .SEGMENT /PM ioadin;
 .VAR ADFIFO; {A/D fifo }
 .ENDSEG;

 .SEGMENT /PM iostat;
 .VAR IOSTAT; {input-output status }
 .ENDSEG;

 .SEGMENT /DM iodaout;
```

```
 .VAR DAFIFO; {D/A fifo }
 .ENDSEG;

 .SEGMENT /DM iochans;
 .VAR CHANNELS;  {input-output channel }
 .ENDSEG;

 .SEGMENT /DM iocntrl;
 .VAR CONTROL;  { control register }
 .ENDSEG;



 .SEGMENT /DM dm_data;
 { Conversion factors                                                    }
 .VAR VOLT2BITS; {bits/volt }
 .VAR BITS2VOLT; {volts/bit }

 .VAR ADINPUT[NUMOFCHANNEL]; {the A/D input}
 .VAR DACONTROL[NUMOFCHANNEL]; {the D/A control signal}
 .VAR ADOFFSET[5]=AD0OFFSET, AD1OFFSET, AD2OFFSET,
  AD3OFFSET, AD4OFFSET; {A/D offsets }
 .VAR DAOFFSET[5]=DA0OFFSET, DA1OFFSET, DA2OFFSET,
   DA3OFFSET,  DA4OFFSET; {D/A offsets }

 {-----------------------Define variables---------------------------------}

 .VAR RAD_SENGAIN=RAD_SEN;

 { Radial bearing variable storage locations  }
 .VAR SMPL_PERIOD; {sampling period}
 .VAR RAD_PERIOD;

{variables for the 1 axis reference model}
 .VAR REF1_POS0[2];
 .VAR REF1_VEL0[2];
 .VAR REF1_POS[2];
 .VAR REF1_VEL[2];

{variables for the 2 axis reference model}
 .VAR REF2_POS0[2];
 .VAR REF2_VEL0[2];
 .VAR REF2_POS[2];
 .VAR REF2_VEL[2];
```

```
{ variables for the plant }
 .VAR RAD_X0[NUMOFCHANNEL];    {x1,y1,x2,y2 new position}
 .VAR RAD_X1[NUMOFCHANNEL];    {x1,y1,x2,y2 old position}
 .VAR RAD_V1[NUMOFCHANNEL];   {x1,y1,x2,y2 old velocity}
 .VAR RAD_V0[NUMOFCHANNEL];   {x1,y1,x2,y2 new velocity}
 .VAR ERR_X[NUMOFCHANNEL];      {x1,y1,x2,y2 position error}
 .VAR ERR_V[NUMOFCHANNEL];      {x1,y1,x2,y2 velocity error}
 .VAR RAD_BINV[NUMOFCHANNEL]; {1/b_{x1}, 1/b_{y1}, 1/b_{x2},
  1/b_{y2}}

 .VAR RAD_CONV; { a conversion factor}

{parameters used in the 1 axis reference model A matrix}
 .VAR REF1_AT12;
 .VAR REF1_AT21;
 .VAR REF1_AT22;

{parameters used in the 2 axis reference model A matrix}
 .VAR REF2_AT12;
 .VAR REF2_AT21;
 .VAR REF2_AT22;

 .VAR PD_U1[4]; {PD matrix for X1,Y1 bearing}
 .VAR PD_U2[4]; {PD matrix for X2,Y2 bearing}
 .VAR NRML_FCTR1; { normalizing factor (1/omega) for 1 axis }
 .VAR NRML_FCTR2; { normalizing factor (1/omega) for 2 axis  }
 .VAR FLAG; {flag for switching the adaptation}
 .VAR ADAPT_U1[4]; { adaptation gain matrix for X1,Y1 bearing, the four
   columns correspond to x1, y1, dx1, dy1}
 .VAR ADAPT_U2[4]; { adaptation gain matrix for X1,Y1 bearing, the four
  columns correspond to x2, y2, dx2, dy2}
 .VAR ADAPT_U[NUMOFCHANNEL]; { adaptation control vector}
 .VAR OVERALL_U[NUMOFCHANNEL]; { overall control vector}

 { Variables needed to save data in memory for later dumping }
 .VAR INPUT_OFFSET;
 .VAR OUTPUT_OFFSET;
 .VAR SAVE_END;


 .ENDSEG;

 .SEGMENT /PM rst_svc;
```

```
{-------------------------------------------------------------------------}
{ At reset, the BANK registers are as follows:                            }
{       PMBANK1 = 0x800000                                                }
{       DMBANK1 = 0x20000000                                              }
{       DMBANK2 = 0x40000000                                              }
{       DMBANK3 = 0x80000000                                              }
{ These values, by coincidence, are perfect for our I/O board             }
{-------------------------------------------------------------------------}

{-------------------------------------------------------------------------}
{ The default value of PMWAIT at reset is 0x0003DE.  This corresponds     }
{ to the following:                                                       }
{       bit  13    = 0   (No automatic wait state)                        }
{       bits 12-10 = 000 (memory page size = 256 words)                   }
{       bits  9-7  = 111 (7 PMBANK1 wait states)                          }
{       bits  6-5  = 10  (Int. and Ext. wait state ack mode)              }
{       bits  4-2  = 111 (7 PMBANK0 wait states)                          }
{       bits  1-0  = 10  (Int. and Ext. wait state ack mode)              }
{                                                                         }
{ For our setup, the DSP board accesses memory at 0 wait states and       }
{ accesses all ports and 1 wait state.  Therefore:                        }
{       bit  13    = 0   (No automatic wait state)                        }
{       bits 12-10 = 100 (memory page size = 4096 words)                  }
{       bits  9-7  = 001 (1 PMBANK1 wait state)                           }
{       bits  6-5  = 10  (Int. and Ext. wait state ack mode)              }
{       bits  4-2  = 000 (0 PMBANK0 wait states)                          }
{       bits  1-0  = 10  (Int. and Ext. wait state ack mode)              }
{-------------------------------------------------------------------------}

 PMWAIT = 0x0010C2;

{-------------------------------------------------------------------------}
{ The default value of DMWAIT at reset is 0x000F7BDE.  This corresponds   }
{ to the following:                                                       }
{       bit  23    = 0   (No automatic wait state)                        }
{       bits 22-20 = 000 (memory page size = 256 words)                   }
{       bits 19-17 = 111 (7 DMBANK3 wait states)                          }
{       bits 16-15 = 10  (Int. and Ext. wait state ack mode)              }
{       bits 14-12 = 111 (7 DMBANK2 wait states)                          }
{       bits 11-10 = 10  (Int. and Ext. wait state ack mode)              }
{       bits  9-7  = 111 (7 DMBANK1 wait states)                          }
{       bits  6-5  = 10  (Int. and Ext. wait state ack mode)              }
{       bits  4-2  = 111 (7 DMBANK0 wait states)                          }
{       bits  1-0  = 10  (Int. and Ext. wait state ack mode)              }
{                                                                         }
```

```
{ For our setup, the DSP board accesses memory at 0 wait states and     }
{ accesses all ports and 1 wait state.  Therefore:                      }
{       bit  23    = 0   (No automatic wait state)                      }
{       bits 22-20 = 100 (memory page size = 4096 words)                }
{       bits 19-17 = 001 (1 DMBANK3 wait states)                        }
{       bits 16-15 = 10  (Int. and Ext. wait state ack mode)            }
{       bits 14-12 = 001 (1 DMBANK2 wait states)                        }
{       bits 11-10 = 10  (Int. and Ext. wait state ack mode)            }
{       bits  9-7  = 000 (0 DMBANK1 wait state)                         }
{       bits  6-5  = 10  (Int. and Ext. wait state ack mode)            }
{       bits  4-2  = 000 (0 DMBANK0 wait states)                        }
{       bits  1-0  = 10  (Int. and Ext. wait state ack mode)            }
{-----------------------------------------------------------------------}

 DMWAIT = 0x00431842;

{-----------------------------------------------------------------------}
{ Set FLAG2 to output mode so we can trigger I/O board conversion when  }
{ we need to.                                                           }
{-----------------------------------------------------------------------}

 MODE2 = FG2OUTPUT;


 JUMP initialize;
.ENDSEG;


.SEGMENT /PM pm_code;

initialize:

{ initialize registers }

 IMASK = 0;
 MODE1 = 0x00012000;

 I0 = 0;
 I1 = 0;
 I2 = 0;
 I3 = 0;
 I4 = 0;
 I5 = 0;
 I6 = 0;
 I7 = 0;
```

```
M0 = 0;
M1 = 0;
M2 = 0;
M3 = 0;
M4 = 0;
M5 = 0;
M6 = 0;
M7 = 0;
L0 = 0;
L1 = 0;
L2 = 0;
L3 = 0;
L4 = 0;
L5 = 0;
L6 = 0;
L7 = 0;
{-------------------------------------------------------------------------}
{ This program does the following:                                        }
{       1.  Triggers A/D conversion on one channel                        }
{       2.  Polls A/D status register to see when conversion complete     }
{       3.  Pushes A/D value out to D/A                                   }
{       4.  returns to step 1                                             }
{-------------------------------------------------------------------------}

{ Make sure FLAG2 toggle is initially zero.                               }
 BIT CLR ASTAT 0x00200000;

{ Calculate D/A conversion factor                                         }
 F0 = DABITSMAX;
 F12 = DAVOLTSMAX;
 DIV;
 DM(VOLT2BITS) = F0;

{ Calculate A/D conversion factor                                         }
 F12 = ADBITSMAX;
 F0 = ADVOLTSMAX;
 DIV;
 DM(BITS2VOLT) = F0;

{ Initialize the control signal to zero }

 B0 = DACONTROL;
 B1 = DAOFFSET;
 F1 = DM(VOLT2BITS);
 F2 = DABITSMAX;
```

```
 LCNTR = NUMOFCHANNEL;
 DO initctr UNTIL LCE;
   F0 = -0.1518;
   R3 = DM(I1,1);
   F3 = FLOAT R3;
   DACONV;
initctr:          DM(I0,1) = R0;


{ Set up radial bearing conversion factor for A/D         }
{ rad_conv=bits2volt/rad_sengain                         }
{ rad_sengain-position sensor conversion factor           }

  F0 = DM(BITS2VOLT);  {1 bit = ? volts    }
  F12 = DM(RAD_SENGAIN);       {1 meters =? volts }

  DIV;

  DM(RAD_CONV) = F0;        {1 bit = ? meters}

{ Set up the sampling time   T  }
 F0 = 1.0;
 F12 =SMPLSPEED;

 DIV;

 DM(SMPL_PERIOD) = F0;

{ Set up radial bearing 1*PERIOD constant      1/(T)          }
 F0 = SMPLSPEED;
 F12 = 1.0;

 DIV;

 DM(RAD_PERIOD) = F0;

{ Set up normalizing constant      1/omega          }
 F0 = 1.0;
 F12 = REF1_NATFREQ;

 DIV;

 DM(NRML_FCTR1) = F0;

 F0 = 1.0;
```

```
F12 = REF2_NATFREQ;

DIV;

DM(NRML_FCTR2) = F0;




{ Set up RAD_BINV constant                                    }

B0 = RAD_BINV;
F0 = 1.0;
F12 = RAD_B1;

DIV;


DM(I0,1) = F0;

F0 = 1.0;
F12 = RAD_B2;

DIV;

DM(I0,1) = F0;

F0 = 1.0;
F12 = RAD_B3;

DIV;

DM(I0,1) = F0;

F0 = 1.0;
F12 = RAD_B4;

DIV;

DM(I0,1) = F0;


{ Set up the 1 axis reference model  A*T matrix constants          }
{ For the reference model, xm(k+1)=(I+A*T)*xm(k)       }
```

```
 F0 = DM(SMPL_PERIOD);

 DM(REF1_AT12) = F0;

 F0 = REF1_NATFREQ;
 F1 = F0;
 F3 = F0*F1;

 F0 = -1.0;
 F7 = F0*F3;
{-Wn1^2 is now stored in F7 }

 F2 = DM(SMPL_PERIOD);
 F3 = F7*F2;

 DM(REF1_AT21) = F3;

 F0 = -2.0;
 F1 = REF_DAMP;
 F2 = REF1_NATFREQ;
 F3 = DM(SMPL_PERIOD);

 F4 = F0*F1;
 F8 = F4*F2;
{-2*damping*Wn1  is now stored in F8}

 F4 = F8*F3;
 F1 = 1.0;
 F4 = F1+F4;
 DM(REF1_AT22) = F4;

{Set up the 2 axis reference model A*T matrix constants          }
{ For the reference model, xm(k+1)=(I+A*T)*xm(k)       }


 F0 = DM(SMPL_PERIOD);

 DM(REF2_AT12) = F0;

 F0 = REF2_NATFREQ;
 F1 = F0;
 F3 = F0*F1;

 F0 = -1.0;
```

```
 F13 = F0*F3;
{-Wn2^2 is now stored in F13 }

 F2 = DM(SMPL_PERIOD);
 F3 = F13*F2;

 DM(REF2_AT21) = F3;

 F0 = -2.0;
 F1 = REF_DAMP;
 F2 = REF2_NATFREQ;
 F3 = DM(SMPL_PERIOD);

 F4 = F0*F1;
 F14 = F4*F2;
{-2*damping*Wn2  is now stored in F14}

 F4 = F14*F3;
 F1 = 1.0;
 F4 = F1+F4;
 DM(REF2_AT22) = F4;


{ Setup the parameters for the PD matrix }
 B0 = PD_U1;
 B1 = PD_U2;
 F1 = ALPHAINV;
 F2 = F1*F7;
 DM(I0,1) = F2;
 F2 = F1*F8;
 DM(I0,1) = F2;

 F1 = BETAINV;
 F2 = F1*F13;
 DM(I0,1) = F2;
 F2 = F1*F7;
 DM(I1,1) = F2;
 F2 = F1*F14;
 DM(I0,1) = F2;
 F2 = F1*F8;
 DM(I1,1) = F2;

 F1 = GAMMAINV;
 F2 = F1*F13;
 DM(I1,1) = F2;
```

```
 F2 = F1*F14;
 DM(I1,1) = F2;

{ Set up parameters for the adaptation gain matrices}
 B0 = ADAPT_U1;
 B1 = ADAPT_U2;

 F0 = 1.0;
 F10 = 2.0;
 F12 = F10*F7;

 DIV;

{ F0 = -1/2Wn1^2}
 F1 = ADAPTATION1;
 F7 = F1*F0;
 F3 = DM(SMPL_PERIOD);
 F7 = F3*F7;
 F9 = F7;
{ F7 =-ADAPTGAIN1* T/2Wn1^2 }

 F0 = F7;
 F1 = REF1_NATFREQ;
 F12 = REF_DAMP;
 F12 = F1*F12;

 DIV;

 F8 = F0;
{ F8 =-ADAPTGAIN1* T/2DAMP*Wn1^3 }



 F0 = 1.0;
 F10 = 2.0;
 F12 = F10*F13;

 DIV;

{ F0 = -1/2Wn2^2}
 F1 = ADAPTATION2;
 F13 = F1*F0;
 F3 = DM(SMPL_PERIOD);
 F13 = F3*F13;
```

```
{ F13 =-ADAPTGAIN2* T/2Wn2^2 }

 F0 = F13;
 F1 = REF2_NATFREQ;
 F12 = REF_DAMP;
 F12 = F1*F12;

 DIV;

 F14 = F0;
{ F14 =-ADAPTGAIN2* T/2DAMP*Wn2^3 }

 F7 = F9;

 F1 = ALPHA;
 F0 = F1*F7;
 DM(I0,1) = F0;
 F0 = F1*F8;
 DM(I0,1) = F0;

 F1 = BETA;
 F0 = F1*F13;
 DM(I0,1) = F0;
 F0 = F1*F7;
 DM(I1,1) = F0;
 F0 = F1*F14;
 DM(I0,1) = F0;
 F0 = F1*F8;
 DM(I1,1) = F0;


 F1 = GAMMA;
 F0 = F1*F13;
 DM(I1,1) = F0;
 F0 = F1*F14;
 DM(I1,1) = F0;


{ Setup the initial velocity for the reference model                }
{ The initial position will be acquired by sampling processes       }
{ Also initialize the flag and adaptation control signal            }
 F0 = 0.0;
 DM(FLAG) = F0;
 B0 = REF1_VEL0;
 B1 = REF2_VEL0;
```

```
 LCNTR = 2;
 DO resetpar1 UNTIL LCE;
  DM(I0,1) = F0;
resetpar1:       DM(I1,1) = F0;
 B1 = RAD_V0;
 B2 = ADAPT_U;
 B3 = OVERALL_U;
 LCNTR = NUMOFCHANNEL;
 DO resetpar UNTIL LCE;
  DM(I1,1) = F0;
  DM(I2,1) = F0;
resetpar:        DM(I3,1) = F0;


{ Setup variables required to save data in memory for later recall    }
 R0 = SAVEOFFSET;
 DM(INPUT_OFFSET) = R0;
 R1 = ASHIFT R0 BY 1;
 R2 = 0x8000;
 R2 = R2-R1;
 R2 = ASHIFT R2 BY -1;
 R1 = R2+R0;
 DM(OUTPUT_OFFSET) = R1;
 R1 = R1+R2;
 DM(SAVE_END) = R1;

{ Reset I/O board                                                     }
 R0 = 0x0;
 DM(CONTROL) = R0;
 NOP; NOP; NOP;

{---------------------------------------------------------------------}
{ Set 1 A/D channel and 0 D/A channels.  When a conversion is triggered,}
{ both the A/D and D/A conversions are triggered.  Therefore, I set the }
{ the number of D/A to 0 so that nothing goes out.                    }
{                                                                     }
{ Number of Channels Register:  [default - DM(0x40000001)]            }
{       bits 2-0 -> number of A/D channels                            }
{       bits 5-3 -> number of D/A channels                            }
{---------------------------------------------------------------------}

 R0 = NUMOFCHANNEL;
 R1 = LSHIFT R0 BY 3;
 R0 = R0+R1;
 DM(CHANNELS) = R0;
```

```
 NOP; NOP; NOP;

{-------------------------------------------------------------------------}
{ Release analog reset (don't know why) and set go mode to flag2 toggle }
{                                                                         }
{ Control Register:  [default - DM(0x40000002)]                           }
{       bits 2-0 -> go mode (0 = go on toggle of FLAG2)                   }
{                           (1 = go on interrupt)                         }
{       bits 5-3 -> IRQ mode                                              }
{       bit    6 -> Status select                                         }
{       bit    7 -> Analog reset                                          }
{-------------------------------------------------------------------------}

 R0 = 0x80;
 DM(CONTROL) = R0;
 NOP; NOP; NOP;



{ Set timer sampling period and counter                                   }

 F12 = SMPLSPEED;
 F0 = CPUSPEED;
 DIV;
 R1 = FIX F0;
 R0 = R1-1;

 TPERIOD = R0;
 TCOUNT = R0;

{Set the initial current}

 B0 = DACONTROL;
 B1 = DAOFFSET;
 LCNTR = NUMOFCHANNEL;
 DO resetctr UNTIL LCE;
  F0 = -0.1518;
  F1 = DM(VOLT2BITS);
  F2 = DABITSMAX;
  R3 = DM(I1,1);
  F3 = FLOAT R3;
  DACONV;

resetctr:        DM(I0,1)=R0;
```

```
{Send the initial current and get the initial position information        }

 B0 = DACONTROL;
 LCNTR = NUMOFCHANNEL;
 DO sentinit UNTIL LCE;
  R0 = DM(I0,1);
sentinit:        DM(DAFIFO) = R0;

 STARTCONV;


 R1 = 0x03;
wait_init:       R0 = PM(IOSTAT);
 R7 = R0 AND R1;
 IF NE JUMP wait_init;




{-------------------------------------------------------------------------}
{ Get A/D value(s) from FIFO.  [default - PM(0x800000)]                    }
{                                                                          }
{ The values obtained are 14-bit 2's-complement values sign extended to }
{ the left.  2's complement is obtained by negating the real value and  }
{ adding 1.  The range of values for our particular A/D is:              }
{                                                                          }
{       +5V = 0001 1111 1111 1111                                          }
{        0V = 0000 0000 0000 0000                                          }
{       -5V = 1110 0000 0000 0001                                          }
{                                                                          }
{ Sample code for converting 2's complement notation to floating point  }
{ is as follows:                                                           }
{               R1 = FEXT R0 BY 0:16 (SE);                                 }
{               F0 = FLOAT R0;                                             }
{                                                                          }
{ Sample code for converting floatin point numbers to 2's complement    }
{ notation is as follows:                                                  }
{               F0 = FIX R0;                                               }
{                                                                          }
{-------------------------------------------------------------------------}

{Read and discard the A/D value}

 LCNTR = NUMOFCHANNEL;
 DO discard UNTIL LCE;
```

```
discard:        R0 = PM(ADFIFO);

{Resend the control signal }

 B0 = DACONTROL;
 LCNTR = NUMOFCHANNEL;
 DO resendctr UNTIL LCE;
  R0 = DM(I0,1);
resendctr:       DM(DAFIFO) = R0;

 STARTCONV;


 R1 = 0x03;
wait_init1:     R0 = PM(IOSTAT);
 R7 = R0 AND R1;
 IF NE JUMP wait_init1;


{ Convert the A/D value to meters  }

 B0 = ADINPUT;
 B1 = ADOFFSET;
 B3 = RAD_X0;
 B4 = RAD_X1;
 LCNTR = NUMOFCHANNEL;
 DO storeinit1 UNTIL LCE;
  R0 = PM(ADFIFO);
  R0 = FEXT R0 BY 0:14 (SE);
  DM(I0,1) = R0;
  R1 = DM(I1,1);
  R0 = R0+R1;
  F0 = FLOAT R0;
  F1 =  DM(RAD_CONV);
  F0 = F0*F1;
{ Store the initial position                                          }
  DM(I3,1) = F0;
storeinit1:      DM(I4,1) = F0;

  B1 = REF1_POS0;
  B2 = REF2_POS0;
  B3 = RAD_X0;
  LCNTR = 2;
  DO storeinit2 UNTIL LCE;
   F0 = DM(I3,1);
```

```
   DM(I1,1) = F0;
   F0 = DM(I3,1);
storeinit2:       DM(I2,1) = F0;



{ Set up input/output save pointers in last address registers          }
 I6 = DM(INPUT_OFFSET);
 I7 = DM(OUTPUT_OFFSET);

{Save the first A/D input(sensor output), D/A output(control input data)}
#ifdef PLOTX1
 B0 = ADINPUT;
 R0 = DM(I0,1);
 DM(I6,1) = R0;
 B0 = DACONTROL;
 R0 = DM(I0,1);
 F3 = DABITSMAX;
 R3 = FIX F3;
 R0 = FEXT R0 BY 2:14;
 R0 = R0-R3;
 DM(I7,1) = R0;

#endif
#ifdef plotx1

 B0 = ADINPUT;
 R0 = DM(I0,1);
 DM(I6,1) = R0;
 B0 = DACONTROL;
 R0 = DM(I0,1);
 F3 = DABITSMAX;
 R3 = FIX F3;
 R0 = FEXT R0 BY 2:14;
 R0 = R0-R3;
 DM(I7,1) = R0;

#endif

#ifdef PLOTX2
 B0 = ADINPUT;
 R0 = DM(1,I0);
 DM(I6,1) = R0;
 B0 = DACONTROL;
```

```
 R0 = DM(1,I0);
 F3 = DABITSMAX;
 R3 = FIX F3;
 R0 = FEXT R0 BY 2:14;
 R0 = R0-R3;
 DM(I7,1) = R0;

#endif
#ifdef plotx2

 B0 = ADINPUT;
 R0 = DM(1,I0);
 DM(I6,1) = R0;
 B0 = DACONTROL;
 R0 = DM(1,I0);
 F3 = DABITSMAX;
 R3 = FIX F3;
 R0 = FEXT R0 BY 2:14;
 R0 = R0-R3;
 DM(I7,1) = R0;

#endif

#ifdef PLOTY1
 B0 = ADINPUT;
 R0 = DM(2,I0);
 DM(I6,1) = R0;
 B0 = DACONTROL;
 R0 = DM(2,I0);
 F3 = DABITSMAX;
 R3 = FIX F3;
 R0 = FEXT R0 BY 2:14;
 R0 = R0-R3;
 DM(I7,1) = R0;

#endif
#ifdef ploty1

 B0 = ADINPUT;
 R0 = DM(2,I0);
 DM(I6,1) = R0;
 B0 = DACONTROL;
 R0 = DM(2,I0);
 F3 = DABITSMAX;
 R3 = FIX F3;
```

```
 R0 = FEXT R0 BY 2:14;
 R0 = R0-R3;
 DM(I7,1) = R0;

#endif

#ifdef PLOTY2
 B0 = ADINPUT;
 R0 = DM(3,I0);
 DM(I6,1) = R0;
 B0 = DACONTROL;
 R0 = DM(3,I0);
 F3 = DABITSMAX;
 R3 = FIX F3;
 R0 = FEXT R0 BY 2:14;
 R0 = R0-R3;
 DM(I7,1) = R0;

#endif
#ifdef ploty2

 B0 = ADINPUT;
 R0 = DM(3,I0);
 DM(I6,1) = R0;
 B0 = DACONTROL;
 R0 = DM(3,I0);
 F3 = DABITSMAX;
 R3 = FIX F3;
 R0 = FEXT R0 BY 2:14;
 R0 = R0-R3;
 DM(I7,1) = R0;

#endif

{ Reset interrupt latch register                                    }
 BIT SET IRPTL 0x0;

{ Allow timer interrupts                                            }
 BIT SET IMASK TMZHI;

{ Turn on timer                                                     }
 BIT SET MODE2 TIMEN;

{ Allow interrupt generation                                        }
 BIT SET MODE1 IRPTEN;
```

```
idlecycle:      IDLE;
 JUMP idlecycle;


sample:
 B0 = DACONTROL;
 LCNTR = NUMOFCHANNEL;
 DO sentctr UNTIL LCE;
  R0 = DM(I0,1);
sentctr:         DM(DAFIFO) = R0;

 STARTCONV; { start  A/D conversion after sampling}



 R1 = 0x03;
wait1:          R0 = PM(IOSTAT);
 R7 = R0 AND R1;
 IF NE JUMP wait1;




{-------------------------------------------------------------------------}
{ Get A/D value(s) from FIFO.  [default - PM(0x800000)]                    }
{                                                                          }
{ The values obtained are 14-bit 2^s-complement values sign extended to    }
{ the left.  2^s complement is obtained by negating the real value and     }
{ adding 1.  The range of values for our particular A/D is:                }
{                                                                          }
{       +5V = 0001 1111 1111 1111                                          }
{        0V = 0000 0000 0000 0000                                          }
{       -5V = 1110 0000 0000 0001                                          }
{                                                                          }
{ Sample code for converting 2^s complement notation to floating point    }
{ is as follows:                                                           }
{               R1 = FEXT R0 BY 0:16 (SE);                                 }
{               F0 = FLOAT R0;                                             }
{                                                                          }
{ Sample code for converting floatin point numbers to 2^s complement       }
{ notation is as follows:                                                  }
{               F0 = FIX R0;                                               }
{                                                                          }
{-------------------------------------------------------------------------}
```

```
 B0 = ADINPUT;
 B1 = ADOFFSET;
 B2 = RAD_X0;
 B3 = RAD_X1;
 B4 = RAD_V1;
 B5 = RAD_V0;
 LCNTR = NUMOFCHANNEL;
 DO smposvel UNTIL LCE;
  R0 = PM(ADFIFO);
  R0 = FEXT R0 BY 0:14 (SE);
  DM(I0,1) = R0;
  R1 = DM(I1,1);
  R0 = R0+R1;
  F0 = FLOAT R0;
  F1 = DM(RAD_CONV);
  F0 = F0*F1;

{Store X0 }

  DM(I2,1) = F0;
{Determine RAW velocity using backward difference }

  F1 = DM(I3,1);
  F0 = F0-F1;

  F1 = DM(RAD_PERIOD);

  F0 = F0*F1;

{Pass the velocity signal through a filter   }
  F1 = C2;
  F0 = F0*F1;

  F1 = C1;
  F2 = DM(I4,1);
  F2 = F1*F2;

  F0 = F0+F2;

smposvel:        DM(I5,1) = F0;



{-------------------------------------------------------------------------}
{The control code start here                                              }
```

```
{-------------------------------------------------------------------------}
{Calculate the reference model signals and the error signals }

 B0 = REF1_POS0;
 B1 = REF1_VEL0;
 B2 = REF1_POS;
 B3 = RAD_X0;
 B4 = ERR_X;
 F5 = DM(REF1_AT12);
 F6 = DM(REF1_AT21);
 F7 = DM(REF1_AT22);
 LCNTR = 2;
 DO refcal1 UNTIL LCE;
  F1 = DM(I1,1);
  F2 = F1*F5;
  F0 = DM(I0,1);
  F2 = F2+F0;
  DM(I2,1) = F2;
  F1 = DM(I3,2);
  F1 = F1-F2;
refcal1:          DM(I4,2)=F1;

 B0 = REF1_POS0;
 B1 = REF1_VEL0;
 B2 = RAD_V0;
 B3 = REF1_VEL;
 B4 = ERR_V;
 LCNTR = 2;
 DO refcal2 UNTIL LCE;
  F1 = DM(I0,1);
  F2 = F6*F1;
  F1 = DM(I1,1);
  F3 = F7*F1;
  F2 = F2+F3;
  DM(I3,1) = F2;
  F1 = DM(I2,2);
  F1 = F1-F2;
refcal2:          DM(I4,2)=F1;


 B0 = REF2_POS0;
 B1 = REF2_VEL0;
 B2 = REF2_POS;
 B3 = RAD_X0;
 B4 = ERR_X;
```

```
 F1 = DM(I3,1);
 F1 = DM(I4,1);
 F5 = DM(REF2_AT12);
 F6 = DM(REF2_AT21);
 F7 = DM(REF2_AT22);
 LCNTR = 2;
 DO refcal3 UNTIL LCE;
  F1 = DM(I1,1);
  F2 = F1*F5;
  F0 = DM(I0,1);
  F2 = F2+F0;
  DM(I2,1) = F2;
  F1 = DM(I3,2);
  F1 = F1-F2;
refcal3:          DM(I4,2)=F1;

 B0 = REF2_POS0;
 B1 = REF2_VEL0;
 B2 = RAD_V0;
 F1 = DM(I2,1);
 B3 = REF2_VEL;
 B4 = ERR_V;
 F1 = DM(I4,1);
 LCNTR = 2;
 DO refcal4 UNTIL LCE;
  F1 = DM(I0,1);
  F2 = F6*F1;
  F1 = DM(I1,1);
  F3 = F7*F1;
  F2 = F2+F3;
  DM(I3,1) = F2;
  F1 = DM(I2,2);
  F1 = F1-F2;
refcal4:          DM(I4,2)=F1;


{In order to simplify the computation, the infinity norm instead of two norm
 is  used to determine the switching of the adaptation. The infinity norm of
 a vector is defined as the largest absolute value among the vectorial
 components}

{Determine the flag value------the flag equals 1 when the infinity norm of
 the error vector is larger than rho(size of the deadzone)+sigma(width of
 the hysteresis loop). The flag equals 0 when the infinity norm of the error
 vector is less than rho-sigma. When the infinity norm of the error vector is
```

```
  between rho+sigma and rho-sigma, the current flag value equals  the flag
  value of the previous sampling period.   }

  F3 = DM(FLAG);

  B0 = ERR_X;
  F0 = DM(I0,1);
  F0 = ABS F0;
  F1 = DM(I0,1);
  F1 = ABS F1;
  F0 = MAX(F0,F1); {Determine the maximum between e_x1 and e_y1}
  F1 = DM(I0,1);
  F1 = ABS F1;
  F0 = MAX(F0,F1); {Determine the maximum between e_x1,e_y1 and e_x2}
  F1 = DM(I0,1);
  F1 = ABS F1;
  F0 = MAX(F0,F1); {Determine the maximum between e_x1,e_y1 e_x2, and e_y2}


  B1 = ERR_V;
  F1 = DM(I1,1);
  F1 = ABS F1;
  F2 = DM(NRML_FCTR1);
  F1 = F1*F2;
  F2 = DM(I1,1);
  F2 = ABS F2;
  F4 = DM(NRML_FCTR2);
  F2 = F2*F4;

  F1 = MAX(F1,F2); {Determine the maximum between e_dx1 and
 e_dy1}
  F2 = DM(I1,1);
  F2 = ABS F2;
  F4 = DM(NRML_FCTR1);
  F2 = F4*F2;
  F1 = MAX(F1,F2); {Determine the maximum between e_dx1,e_dy1,
 e_dx2}
  F2 = DM(I1,1);
  F2 = ABS F2;
  F4 = DM(NRML_FCTR2);
  F2 = F4*F2;
  F1 = MAX(F1,F2); {Determine the maximum between e_dx1,e_dy1,
e_dx2, and e_dy2}
```

```
 F2 = MAX(F0,F1); {Determine the infinity norm of the error vector}
 F4 = HYSTERESIS;

 COMP(F2,F4);
 IF LE JUMP setflag0;

 F1 = 2.0;
 F4 = F1*F4;

 COMP(F2,F4);
 IF GT JUMP setflag1;
 JUMP setflag;

setflag0:       F3 = 0.0;
 JUMP setflag;

setflag1:       F3 = 1.0;
 JUMP setflag;

setflag:       DM(FLAG) = F3;


{Determine the PD and adaptive control action }
 B0 = ADAPT_U1;
 B1 = ADAPT_U2;
 B2 = ERR_X;
 B3 = ERR_V;
 F7 = 0.0;
 F8 = 0.0;
 LCNTR = 2;
 DO adaptcalx UNTIL LCE;
  F0 = DM(I2,1);
  F1 = DM(I0,1);
  F1 = F0*F1;
  F7 = F7+F1;
  F2 = DM(I1,1);
  F2 = F0*F2;
  F8 = F8+F2;
  F0 = DM(I3,1);
  F1 = DM(I0,1);
  F1 = F0*F1;
  F7 = F7+F1;
  F2 = DM(I1,1);
  F2 = F0*F2;
```

```
adaptcalx:      F8 = F8+F2; {F7,F8 store the x adaptive action}


 B0 = ADAPT_U1;
 B1 = ADAPT_U2;
 F11 = 0.0;
 F12 = 0.0;
 LCNTR = 2;
 DO adaptcaly UNTIL LCE;
  F0 = DM(I2,1);
  F1 = DM(I0,1);
  F1 = F0*F1;
  F11 = F11+F1;
  F2 = DM(I1,1);
  F2 = F0*F2;
  F12 = F12+F2;
  F0 = DM(I3,1);
  F1 = DM(I0,1);
  F1 = F0*F1;
  F11 = F11+F1;
  F2 = DM(I1,1);
  F2 = F0*F2;
adaptcaly:      F12 = F12+F2; {F11,F12 store the y adaptive action}

 B0 = PD_U1;
 B1 = PD_U2;
 B2 = RAD_X0;
 B3 = RAD_V0;
 F9 = 0.0;
 F10 = 0.0;
 LCNTR = 2;
 DO pdcalx UNTIL LCE;
  F0 = DM(I2,1);
  F1 = DM(I0,1);
  F1 = F0*F1;
  F9 = F9+F1;
  F2 = DM(I1,1);
  F2 = F0*F2;
  F10 = F10+F2;
  F0 = DM(I3,1);
  F1 = DM(I0,1);
  F1 = F0*F1;
  F9 = F9+F1;
  F2 = DM(I1,1);
  F2 = F0*F2;
```

```
pdcalx:          F10 = F10+F2; {F9,F10 store the x PD action}

 B0 = PD_U1;
 B1 = PD_U2;
 F13 = 0.0;
 F14 = 0.0;
 LCNTR = 2;
 DO pdcaly UNTIL LCE;
  F0 = DM(I2,1);
  F1 = DM(I0,1);
  F1 = F0*F1;
  F13 = F13+F1;
  F2 = DM(I1,1);
  F2 = F0*F2;
  F14 = F14+F2;
  F0 = DM(I3,1);
  F1 = DM(I0,1);
  F1 = F0*F1;
  F13 = F13+F1;
  F2 = DM(I1,1);
  F2 = F0*F2;
pdcaly:          F14 = F14+F2; {F13,F14 store the PD action}


 F4 = DM(FLAG);
 F7 = F7*F4;
 F8 = F8*F4;
 B1 = ADAPT_U;
 B0 = OVERALL_U;
 F1 = DM(I1,0);
 F7 = F7+F1; {adaptive control action }
 DM(I1,1) = F7;
 F5 = F7+F9;
 DM(I0,1) = F5; {Radx1 adaptive + PD control action}
 F1 = DM(I1,0);
 F8 = F8+F1;
 DM(I1,1) = F8; {adaptive control action }
 F5 = F8+F10;
 DM(I0,1) = F5; {Radx2 adaptive + PD control action}

 F4 = DM(FLAG);
 F11 = F11*F4;
 F12 = F12*F4;

 F1 = DM(I1,0);
```

```
 F11 = F11+F1; {adaptive control action }
 DM(I1,1) = F11;
 F5 = F11+F13;
 DM(I0,1) = F5; {Radx1 adaptive + PD control action}
 F1 = DM(I1,0);
 F12 = F12+F1;
 DM(I1,1) = F12; {adaptive control action }
 F5 = F12+F14;
 DM(I0,1) = F5; {Radx2 adaptive + PD control action}


 B0 = OVERALL_U;
 B1 = RAD_BINV;
 B2 = DACONTROL;
 B3 = DAOFFSET;
 LCNTR = NUMOFCHANNEL;
 DO checksat UNTIL LCE;
  F0 = DM(I0,1);
  F2 = DM(I1,1);
  F0 = F2*F0;

{Check if any saturation occurs in the control current}

  F2 = RAD_MAXU;

  COMP(F0,F2);
  IF GT F0=F2;
  F2=-F2;
  COMP(F0,F2);
  IF LT F0=F2;

  F1 = -0.1518;
  F0 = F0+F1;
  F1 = DM(VOLT2BITS);
  F2 = DABITSMAX;
  R3 = DM(I3,1);
  F3 = FLOAT R3;
  DACONV;

  DM(I2,1)=R0;

checksat:        DM(DAFIFO) = R0;


 STARTCONV;
```

```
 R1 = 0x03;
wait2:          R0 = PM(IOSTAT);
 R7 = R0 AND R1;
 IF NE JUMP wait2;



{Save the reference position, velocity       }

 B0 = REF1_POS;
 B1 = REF1_POS0;
 B2 = REF1_VEL;
 B3 = REF1_VEL0;
 LCNTR = 2;
 DO savedata1 UNTIL LCE;
  F0 = DM(I0,1);
  DM(I1,1) = F0;
  F0 = DM(I2,1);
savedata1:       DM(I3,1) = F0;

 B0 = REF2_POS;
 B1 = REF2_POS0;
 B2 = REF2_VEL;
 B3 = REF2_VEL0;
 LCNTR = 2;
 DO savedata3 UNTIL LCE;
  F0 = DM(I0,1);
  DM(I1,1) = F0;
  F0 = DM(I2,1);
savedata3:       DM(I3,1) = F0;


{Update system position information }

 B0 = RAD_X0;
 B1 = RAD_X1;
 B2 = RAD_V0;
 B3 = RAD_V1;
 LCNTR = NUMOFCHANNEL;
 DO savedata2 UNTIL LCE;

  F0 = DM(I0,1);
  DM(I1,1) = F0;
```

```
  F0 = DM(I2,1);
savedata2:        DM(I3,1) = F0;


{ Save original input value before we over-write it                    }
#ifdef PLOTX1
 R0 = I6;
 R1 = DM(OUTPUT_OFFSET);
 R0 = R1-R0;
 IF EQ JUMP sskip;

 B0 = ADINPUT;
 R0 = DM(I0,1);
 DM(I6,1) = R0;
 R0 = I7;
 R1 = DM(SAVE_END);
 R0 = R1-R0;
 IF EQ JUMP sskip;

 B0 = DACONTROL;
 R0 = DM(I0,1);
 F3 = DABITSMAX;
 R3 = FIX F3;
 R0 = FEXT R0 BY 2:14;
 R0 = R0-R3;
 DM(I7,1) = R0;

#endif

#ifdef plotx1
 R0 = I6;
 R1 = DM(OUTPUT_OFFSET);
 R0 = R1-R0;
 IF EQ JUMP sskip;

 B0 = ADINPUT;
 R0 = DM(I0,1);
 DM(I6,1) = R0;
 R0 = I7;
 R1 = DM(SAVE_END);
 R0 = R1-R0;
 IF EQ JUMP sskip;

 B0 = DACONTROL;
 R0 = DM(I0,1);
```

```
 F3 = DABITSMAX;
 R3 = FIX F3;
 R0 = FEXT R0 BY 2:14;
 R0 = R0-R3;
 DM(I7,1) = R0;

#endif

#ifdef PLOTX2
 R0 = I6;
 R1 = DM(OUTPUT_OFFSET);
 R0 = R1-R0;
 IF EQ JUMP sskip;

 B0 = ADINPUT;
 R0 = DM(1,I0);
 DM(I6,1) = R0;
 R0 = I7;
 R1 = DM(SAVE_END);
 R0 = R1-R0;
 IF EQ JUMP sskip;

 B0 = DACONTROL;
 R0 = DM(1,I0);
 F3 = DABITSMAX;
 R3 = FIX F3;
 R0 = FEXT R0 BY 2:14;
 R0 = R0-R3;
 DM(I7,1) = R0;

#endif

#ifdef plotx2
 R0 = I6;
 R1 = DM(OUTPUT_OFFSET);
 R0 = R1-R0;
 IF EQ JUMP sskip;

 B0 = ADINPUT;
 R0 = DM(1,I0);
 DM(I6,1) = R0;
 R0 = I7;
 R1 = DM(SAVE_END);
 R0 = R1-R0;
 IF EQ JUMP sskip;
```

```
 B0 = DACONTROL;
 R0 = DM(1,I0);
 F3 = DABITSMAX;
 R3 = FIX F3;
 R0 = FEXT R0 BY 2:14;
 R0 = R0-R3;
 DM(I7,1) = R0;

#endif

#ifdef PLOTY1
 R0 = I6;
 R1 = DM(OUTPUT_OFFSET);
 R0 = R1-R0;
 IF EQ JUMP sskip;

 B0 = ADINPUT;
 R0 = DM(2,I0);
 DM(I6,1) = R0;
 R0 = I7;
 R1 = DM(SAVE_END);
 R0 = R1-R0;
 IF EQ JUMP sskip;

 B0 = DACONTROL;
 R0 = DM(2,I0);
 F3 = DABITSMAX;
 R3 = FIX F3;
 R0 = FEXT R0 BY 2:14;
 R0 = R0-R3;
 DM(I7,1) = R0;

#endif

#ifdef ploty1
 R0 = I6;
 R1 = DM(OUTPUT_OFFSET);
 R0 = R1-R0;
 IF EQ JUMP sskip;

 B0 = ADINPUT;
 R0 = DM(2,I0);
 DM(I6,1) = R0;
 R0 = I7;
```

```
 R1 = DM(SAVE_END);
 R0 = R1-R0;
 IF EQ JUMP sskip;

 B0 = DACONTROL;
 R0 = DM(2,I0);
 F3 = DABITSMAX;
 R3 = FIX F3;
 R0 = FEXT R0 BY 2:14;
 R0 = R0-R3;
 DM(I7,1) = R0;

#endif

#ifdef PLOTY2
 R0 = I6;
 R1 = DM(OUTPUT_OFFSET);
 R0 = R1-R0;
 IF EQ JUMP sskip;

 B0 = ADINPUT;
 R0 = DM(3,I0);
 DM(I6,1) = R0;
 R0 = I7;
 R1 = DM(SAVE_END);
 R0 = R1-R0;
 IF EQ JUMP sskip;

 B0 = DACONTROL;
 R0 = DM(3,I0);
 F3 = DABITSMAX;
 R3 = FIX F3;
 R0 = FEXT R0 BY 2:14;
 R0 = R0-R3;
 DM(I7,1) = R0;

#endif

#ifdef ploty2
 R0 = I6;
 R1 = DM(OUTPUT_OFFSET);
 R0 = R1-R0;
 IF EQ JUMP sskip;

 B0 = ADINPUT;
```

```
 R0 = DM(3,I0);
 DM(I6,1) = R0;
 R0 = I7;
 R1 = DM(SAVE_END);
 R0 = R1-R0;
 IF EQ JUMP sskip;

 B0 = DACONTROL;
 R0 = DM(3,I0);
 F3 = DABITSMAX;
 R3 = FIX F3;
 R0 = FEXT R0 BY 2:14;
 R0 = R0-R3;
 DM(I7,1) = R0;

#endif

sskip:          LCNTR = NUMOFCHANNEL;
 DO sendagain UNTIL LCE;
sendagain:      R0 = PM(ADFIFO);



ret:
 RTI;

.ENDSEG;


.SEGMENT /PM tmzh_svc;

 JUMP sample;

.ENDSEG;
```

Bibliography

[1] Allaire, P. (Editor), *Proceeding of the Third International Symposium on Magnetic Bearings*, Washington, July 1992.

[2] Analog Devices, *ADSP-21000: User's Manual*, 1991.

[3] Analog Devices, *ADSP-21000 Family: Assembler Tools & Simulator Manual*, 1991.

[4] B. D. O. Anderson and J. B. Moore, *Optimal Control: Linear Quadratic Methods*. NJ: Prentice-Hall, 1990.

[5] T. M. Apostol, *Mathematical Analysis*. NY: Addison-Wesley, 1975.

[6] M. Athans, *Lecture Notes in Multivariable Control Systems*, Department of Electrical Engineering, Massachusetts Institute of Technology,1993.

[7] R. V. Braembussche (Editor), *Vibration and Rotor Dynamics*, von Karman Institute for Fluid Dynamics, Lecture Series 1992-06.

[8] K. R. Bornstein, "Dynamic Load Capabilities of Active Electromagnetic Bearings," *ASME Journal of Tribology*, Vol. 113, pp. 598-602, 1991.

[9] D. Childs, *Turbomachinery Rotor dynamics: Phenomena, Modeling, and Analysis*, John Wiley & Sons, Inc., 1993.

[10] Compumotor Digiplan, *Positioning Control Systems and Drives : 1991-1992 Catalog.*

[11] S. H. Crandall, D. C. Karnopp, E. F. Kurtz, and D. C. Pridmore-Brown, *Dynamics of Mechanical and Electro-mechanical Systems*, NY : McGraw-Hill, 1968.

[12] M. A. Dahleh and I. D. Diaz-Bobillo, *Control of Uncertain Systems*, New Jersey, Prentice-Hall, Inc., 1995.

[13] D. Dhar and L. E. Barrett, "Design of Magnetic Bearings for Rotor Systems with Harmonic Excitations," *ASME Journal of Tribology*, Vol. 115, pp. 359-366, 1993.

[14] J. C. Doyle, B. A. Francis, and A. R. Tannenbaum, *Feedback Control Theory*, NY: Macmillan Publishing Company, 1992.

[15] M. Dussaux, "The Industrial Applications of Active Magnetic Bearing Technology," Proceedings of the Second International Symposium on Magnetic Bearings, July 12-14, 1990, pp.33-38.

[16] S. Earnshaw, "On the nature of Molecular Forces," *Transactions at the Cambridge Philosophical Society*, Vol. 7, 1842, pp. 97-112.

[17] B. C. Fabien, "Controller Gain Selection for an Electromagnetic Suspension Under Random Excitation," *ASME Journal of Dynamic Systems, Measurement and Control*, Vol. 115, pp. 156-165, Mar.. 1993.

[18] T. A. Higabseb and B. A. Foss, "Constructing NARMAX models using ARMAX models," *Int. J. Contr.*, Vol. 58, pp.1125-1154, Nov. 1993. Englewood Cliffs, NJ: Prentice-Hall, 1989.

[19] T. Higuchi (Editor), *Proceeding of the Second International Symposium on Magnetic Bearings*, Toyko, July 1990.

[20] Hispano-Sula. "Totally Active Magnetic Suspension System," Société D'Exploitation Des Matérials, French Patent 1186527, November 1957.

[21] C.-W. Lee, *Vibration Analysis of Rotors*. Dordrecht: Boston, Kluwer Academic Publishers, 1993.

[22] W. Messner, R. Horowitz, W.-W. Kao and M. Boals "A New Adaptive Learning Rule," *IEEE Trans. on Automat. Contr.* Vol. 36, pp 188-197, Feb., 1991.

[23] M. Hubbard and P. Mcdonald, "Feedback Control Systems for Flywheel Radial Instabilities," *1980 Flywheel Technology Symposium Proceedings*, Scottsdale, Arizona, Oct. 1980.

[24] D. C. Karnopp, D. L. Margolis, and R. C. Rosenberg, *System Dynamics - A Unified Approach*, John Wiley & Sons, Inc., 1990.

[25] C.-W. Lee and J.-S. Kim, "Modal Testing and Suboptimal Vibration Control of Flexible Rotor Bearing System by Using a Magnetic Bearing," *ASME Journal of Dynamic Systems, Measurement and Control*, Vol. 114, pp. 244-252, Jun., 1992.

[26] J. M. Maciejowski, *Multivariable Feedback Design*, Addison-Wesley Publishing Company, 1989.

[27] E. Maslen, and et al., " Practical Limits to the Performance of Magnetic Bearings: Peak Force, Slew Rate, and Displacement Sensitivity. " *ASME Journal of Tribology*, Vol 111, pp. 331-336, 1989.

[28] F. Matsumara and T. Yoshimoto, "System Modeling and Control Design of a Horizontal-Shaft Magnetic-Bearing System," *IEEE Trans. on Magnetics*, Vol.MAG-22, No. 3, May, 1986.

[29] MAXIM, *1993 New Releases Data Book Volume II.*

[30] L. Meirovitch. *Analytical Methods in Vibrations.* London: Macmillan Publishing Company, 1967.

[31] K. M. Misovec, F. Flynn, B. G. Johnson, and J. K. Hedrick, "Sliding Mode Control of Magnetic Suspensions for Precision Pointing and Tracking Applications." ASME Winter Annual Meeting. 1990.

[32] K. S. Narendra and A.M. Annaswamy. *Stable Adaptive Systems.* Englewood Cliffs. NJ: Prentice-Hall. 1989.

[33] K. S. Narendra and K. Parthassarathy. "Identification and Control of Dynamical Systems Using Neural Networks." *IEEE Trans. on Neur. Net.*, Vol. 1, pp 4-26. Mar.. 1990.

[34] D. K. Rao . et al.. "Stiffness of Magnetic bearings Subjected to Combined Static and Dynamic Loads." *ASME Journal of Tribology.* Vol. 114. pp. 785-789, 1992.

[35] H. C. Roters, *Electromagnetic Devices.* John Wiley & Sons, Inc., London. 1961.

[36] S. Reddy, "Theory of Time Delay Control and Application to Magnetic Bearings," Ph.D. thesis. Department of Mechanical Engineering, Massachusetts Institute of Technology. Sep.. 1992.

[37] S. Sinha, K. L. Meese and K. W. Wang. "Sliding Mode Control of a Rigid Rotor via Magnetic Bearings," ASME Biennial Conference on Mechanical Vibratin adn Noise. Florida, Sep. 1991.

[38] R. M. Sanner and J.-J. E. Slotine "Gaussian Network for Direct Adaptive Control," *Proc. Amer. Contr. Conf.*. pp 2153-2159, 1991.

[39] J.-J. E. Slotine and W. Li, *Applied Nonlinear Control.* Englewood Cliffs, NJ: Prentice-Hall, 1991.

[40] J.-J. E. Slotine and S. S. Sastry, "Tracking Control of Nonlinear Systems Using Sliding Surfaces With Applications to Robot Manipulators," *Int. J. Control*, Vol. 39, No. 2, 1983.

[41] C. K. Sortore et al., "Permanent Magnet Biased Magnetic Bearings - Design, Construction and Testing," *Proc. 2nd Intl. Sym. on Magnetic Bearings*, pp. 175-182, 1990.

[42] G. Stein and M. Athans, " The LQG/LTR Procedure for Multivariable Feedback Control Design, " *IEEE Tran. Automatic Control*, AC-32, pp. 105-114, 1984.

[43] G. Scheitzer (Editor), *Proceeding of the First International Symposium on Magnetic Bearings*, Zürish, July 1988.

[44] Slemon, G. R. and Straughen, A., 1980, *Electric Machines*, Addison-Wesley Publishing Company.

[45] D. L. Trumper, "Nonlinear Compensation Techniques for Magnetic Suspension Systems," *Proceeding of NASA Workshop on Aerospace Applications of Magnetic Suspension Technology*, NASA Langley Research Center, Hampton, VA, Sep. 1990.

[46] D. L. Trumper, "Experimental Results in Nonlinear Compensation of a One-Degree-of-Freedom Magnetic Suspension," *Proceeding of NASA Workshop on Aerospace Applications of Magnetic Suspension Technology*, NASA Langley Research Center, Hampton, VA, Aug. 1991.

[47] V. I. Utkin, "Variable Structure With Sliding Mode: A Survey," *IEEE Trans. on Automat. Contr*, Vol. 2, 1977.

[48] J. Wetzel, "Implementation of Time Delay Control to Magnetic Bearings," *Laboratory for Manufacturing and Productivity Report*, Massachusetts Institute of Technology, in preparation.

[49] H. H. Woodson and J. R. Melcher, *Electromechanical Dynamics.* NY: John Wiley and Sons, 1968.

[50] T.-J. Yeh and K. Youcef-Toumi "Design and Control Integration of Magnetic Bearing Systems, Part I: Modeling and Performance Limitations," *ASME winter annual meeting*, Nov., 1994.

[51] T.-J. Yeh and K. Youcef-Toumi "Design and Control Integration of Magnetic Bearing Systems, Part II: Loop Transfer Recovery based design methodology," *ASME winter annual meeting*, Nov.. 1994.

[52] K. Youcef-Toumi, T. Chuang and T. Hawkey, "Analysis and Control of Active Magnetic Bearings," *Laboratory for Manufacturing and Productivity Report*, Massachusetts Institute of Technology, March, 1989.

[53] K. Youcef-Toumi and T. Fuhlbrigge, "Application of a Decentralized Time Delay Controller to Robot Manipulators." *Proceedings of the 1989 IEEE Conference on Robotics and Automation.*

[54] K. Youcef-Toumi and O. Ito, "Controller Design for Systems with Unknown Dynamics," *ASME Journal of Dynamic Systems, Measurement and Control*, Vol. 112, No.1, pp. 133-142, Mar., 1990.

[55] K. Youcef-Toumi, S. Reddy, "Stability Analysis of Time Delay Control with Application to High Speed Magnetic Bearings," ASME winter annual meeting, 1990.

[56] K. Youcef-Toumi, S. Reddy, "Dynamic Analysis and Control of High Speed and High Precision Active Magnetic Bearings," *ASME Journal of Dynamic Systems, Measurement and Control.* Vol. 114, pp. 623-633, Dec., 1992.

[57] H. Zlotykamien, "The Active Magnetic Bearing Enables Optimum Control of Machine Vibrations," *Proceeding of the Fourth International Conference on Vibrations in Rotating Machinery*, Edinburgh, Scotland, Sept., 1988.

THESIS PROCESSING SLIP

FIXED FIELD: ill. _____ name _____

index _____ biblio _____

▶ COPIES: (Archives) Aero Dewey (Eng) Hum
Lindgren Music Rotch Science

TITLE VARIES: ▶☐ _____

NAME VARIES: ▶☐ _____

IMPRINT: (COPYRIGHT) _____

▶ COLLATION: 208 l

▶ ADD. DEGREE: _____ ▶ DEPT.: _____

SUPERVISORS: _____

NOTES:

cat'r: date:

page: F50

▶ DEPT: M.E.

▶ YEAR: 1996 ▶ DEGREE: Sc.D.

▶ NAME: YEH, Ting-Jen